Error Analysis of an Airborne FMCW ATI SAR for Ocean Surface Currents Retrieval

Huazeng Deng

A dissertation
submitted in partial fulfillment of the
requirements for the degree of

Doctor of Philosophy

University of Washington

2018

Reading Committee:

John D. Sahr, Chair

Gordon Farquharson

Bruce R. Darling

Dale P. Winebrenner

Program Authorized to Offer Degree:
Electrical Engineering

University of Washington

Abstract

Error Analysis of an Airborne FMCW ATI SAR
for Ocean Surface Currents Retrieval

Huazeng Deng

Chair of the Supervisory Committee:
Professor John D. Sahr
Department of Electrical Engineering

Along-track interferometric synthetic aperture radar (ATI-SAR) has shown its promise in high-resolution ocean surface currents velocity mapping. An accurate velocity measurement by ATI-SAR requires precise phase difference or interferometric phase estimation between receivers. This work explores possible instrumental and platform error sources that may introduce the observed ATI phase error from field experiments. With technical analysis and literature review, a number of possible error sources were presented and a comprehensive error analysis was performed to study the effects of the phase mismatch between receiver channels, phase imbalance between receive antennas, uncompensated motion errors due to the inaccurate measurements of platform attitude/velocity, and ATI phase errors due to the uncertainty of the reference digital elevation model (DEM) map.

The range-dependent phase fluctuations observed in ATI-SAR interferogram are demonstrated to be caused by the mismatch in the phase responses between the two receiver channels of the radar. A novel phase ripple calibration scheme was presented to mitigate the phase fluctuations during the SAR processing and could be applied to real-time calibration. The residual phase offset in the range direction is proved to be most likely due to the imbalance between the receive antennas' phase patterns. The estimation of the antenna phase imbalance with the collected farmland data was applied to remove most of the residual phase

offset. The phase undulations observed in the along-track direction of the interferogram are demonstrated to be related to the uncompensated motion errors introduced by the inaccurate attitude and velocity measurements by the inertial navigation system (INS). The DEM uncertainty analysis shows that the ATI phase error due to the DEM height error cannot be neglected when the DEM uncertainty exceeds a threshold.

With all proposed calibration approaches, the ATI phase error can be reduced by as much as 1 radians after calibration, which converts to about 55 cm/s ocean surface velocity error. Assuming no ocean waves exists in the imaged scene, which means the Doppler measurements made by ATI-SAR consist of contributions only from the ocean surface currents, the estimated surface velocity error can be reduced from 70 cm/s to about 14 cm/s, which is a significant improvement for ocean surface currents mapping with ATI-SAR.

TABLE OF CONTENTS

LIST OF FIGURES

LIST OF TABLES

ACKNOWLEDGMENTS

I wish to express my sincere appreciation to a number of wonderful people who provides me with invaluable advice and generous help during the long journey of my PhD at the University of Washington (UW). It is their endless and inspiring encouragement which made me believe in my hard work and finally, reach the ending point of this journey.

First, I would like to thank both my PhD advisors, Dr. Gordon Farquharson, and Prof. John Sahr, for their consistent support and encouragement over the past few years. Gordon has been an amazing advisor who is good at inspiring people and teaching me to believe in the value of my work and efforts. He not only taught me how to tackle the challenges in my research but also played an awesome role model whose upright and generous characteristics had a deep influence on me. Also, thanks to the financial support he offered me over the first few years, which helped me be able to focus on my research and make faster progress. After Gordon left UW and joined Capella Space, Prof. John Sahr kindly took the role of advising me on the completion of the rest of my PhD research with his expertise in radar signal processing and remote sensing. I'm very grateful for John's willingness to advise me on my previous research topic, which has a significant impact on making possible the continuation of my research without changing topic. John is always available to share his opinions despite his busy schedule. I've received countless insightful advice on research from John and grown a lot through our many long discussions over the past two years. Without Gordon and John's support, I would never be able to reach the current stage.

I would also like to thank members of my PhD committee. Prof. Andy Jessup kindly offered me lots of helpful advice on my research with his expertise on remote sensing and inspiring encouragement whenever I lost confidence in completing my research during the

hard times. I greatly appreciate his favor by seeking financial support for me after my research assistantships ended. Prof. Dale Winebrenner is such a kind professor and friend who offers me great patience and advice on how to improve my research ability. I benefited a lot from those long conversations with him. Prof. Bruce Darling also provides me with valuable suggestions on my research proposal and dissertation, especially the understanding of the radar hardware in my study. All their efforts made the results of my research more complete and convincing.

Moreover, some special thanks to the amazing folks from EE and the Applied Physics Lab at UW. I would like to thank my brilliant labmate Shadi A, who fight together with me to tackle difficult challenges in our research over the past five years. I'm also very grateful for Dr. Chris Chickadel and Dr. Jim Thompson's patient help and guidance on ocean remote sensing with their expertise in oceanography.

Last but not least, I should express my sincere thanks to my beloved family and friends for their continuous support and love over the long journey. You are always my strongest backup and those who believe in what I can achieve. I would never be able to complete this without you.

DEDICATION

To my beloved parents, Huanqi Deng and Yuanling Wang, and my dear grandparents, for their love, strongest support and long-lasting encouragement.

Chapter 1

INTRODUCTION

Along-track interferometric Synthetic Aperture Radar (ATI-SAR) has shown its promise in the study of ocean surface waves and currents. It has been employed on airborne and spaceborne platforms for ocean surface velocity measurements. By carrying the radar on a moving platform, it creates a long synthetic aperture which greatly improves the spatial resolution and also covers a much wider area than traditional point sensors and near-shore high-frequency radars. Since the estimated radial velocity is directly proportional to the phase difference (also known as the interferometric phase) between the received signals of the two receiver channels, care must be taken on the accuracy of the phase measurement by the radar instrument. This chapter provides a brief overview of advances in ATI-SAR technology and introduces the challenges of employing along-track SAR interferometry, which must be overcome for accurate ocean surface motion estimation.

1.1 Importance of Ocean Surface Currents and Conventional Measurements

The study of the ocean surface waves and currents is crucial for the understanding the exchanges of heat, momentum, nutrients, water, and gases between the atmosphere and the ocean. The ocean surface currents are an important process in modifying the surface wave field. Because of currents' spatial and temporal variations over a vast area, it is very difficult to characterize these current fields using measurements from in situ point sensors such as surface drifters, buoys (Figure 1.1). High frequency (HF) radars have also been employed on the coast (Figure 1.2) and they are capable of mapping the ocean surface currents in the near-shore regions as far as a few hundred kilometers from the shore. However, HF radars can only achieve spatial resolution on the order of 1 km because they are real aperture

radars whose spatial resolution is greatly limited by the length of the antenna's physical aperture length. Synthetic Aperture Radars (SAR) have been effective and are of great interest for the remote sensing of ocean surface during the past few decades because of their high spatial resolution and nearly instantaneous coverage of large ocean areas. As is shown in Figure 1.3, the high azimuth resolution of SAR is achieved by synthesis over finite integration of the known phase history of the backscattered signal that is Doppler-shifted due to relative motion between the radar and the target being imaged [10] . High range resolution is achieved by modulating the transmitted signal. The imaging mechanism of ocean waves by a conventional SAR is determined by several basic modulation processes. These include the tilt modulation, hydrodynamic modulation, velocity bunching. However, it is difficult to retrieve significant ocean wave heights and surface current from conventional SAR data, because the ocean wave-radar modulation transfer function (MTF) of the imaging process can only be estimated under certain limiting conditions.

1.2 Ocean Surface Currents Retrieval by ATI-SAR

More recently, along-track interferometric (ATI) SAR has been implemented and become an increasingly popular technique for the measurement of ocean surface currents. An ATI-SAR employs two antennas separated by a fixed distance along the platform flight direction. Each antenna measures the backscattered signal from the same scatterer on the ocean surface at slightly different times. The phase difference between the two measurements is proportional to the radial velocity of the scatterer relative to the radar look direction. Goldstein and Zebker [11, 12] first demonstrated the capability of ATI-SAR for ocean surface current estimate in San Francisco Bay, Mission Bay and San Diego Bay. Shemer et al. [13] retrieved the two-dimension surface ocean current fields in Monterey Bay by subtracting the effective phase velocity of the Bragg waves from the ATI-SAR measured radial velocity. Graber et al. [14] derived for the first time a high-resolution, area-extensive vector surface current map from interferometric synthetic aperture radar (InSAR) over the continental shelf region off the coast of Cape Hatteras. His study has shown the good agreement of the InSAR current

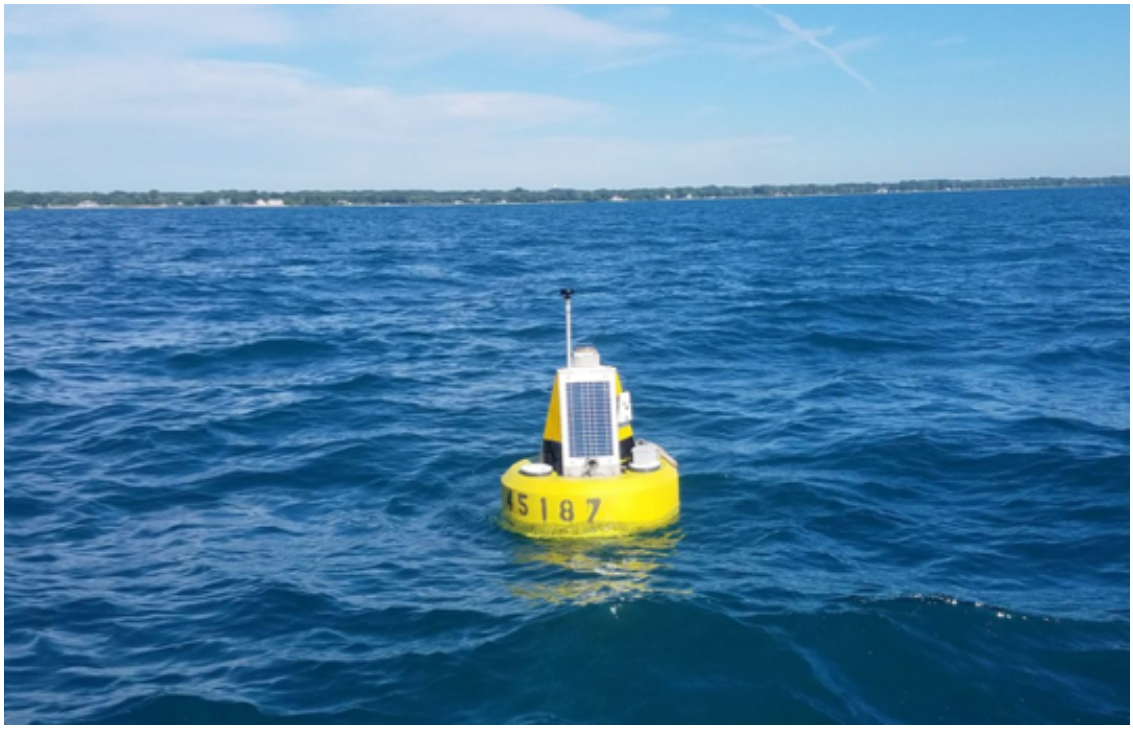

Figure 1.1: Demonstration of the buoy as the in situ point sensor. The nearshore buoys developed by LimnoTech, Inc. were deployed off Waukegan and Winthrop Harbor, Illinois, USA. Reprinted from [1].

estimates with the in-situ measurements, in cases where no strong current gradients were present. Kim et al. [4] developed a new and practical method to extract the surface current component utilizing simultaneously measured dual-frequency ATI-SAR data that were collected off the Ulsan coast in the southeastern part of the Korean peninsula. With dual-frequency measurements, the Bragg wave phase velocity were effectively eliminated from the ATI-SAR velocity and the extracted surface current vectors showed very close agreement with the in situ current measurements. Although their current estimates can be used to generate a more accurate high-resolution current map from currently available ATI-SAR system without any in situ meteorological observations, they are not the actual current velocity since they still contained additional residual velocity components induced by the long ocean wave

Figure 1.2: Near-shore high frequency radar developed by Qualitas Environmental Solutions for the measurement of surface currents and waves with a measuring range of up to 200 km. Reprinted from [2].

motions.

The ATI-SAR implementation discussed above employs the traditional configuration [12], in which the radar measures only one line-of-sight component of surface velocity vector. The retrieval of the fully two-dimensional velocity vectors requires two or more intersecting passes of the aircraft [14], during which time the current field is assumed to be constant. Furthermore, the vector estimates can only be made over the limited area where the SAR images overlap, making the long-distance strip mapping less possible. To overcome these limitations, Rodriguez et al. [15] proposed the idea of utilizing dual-beam interferometry

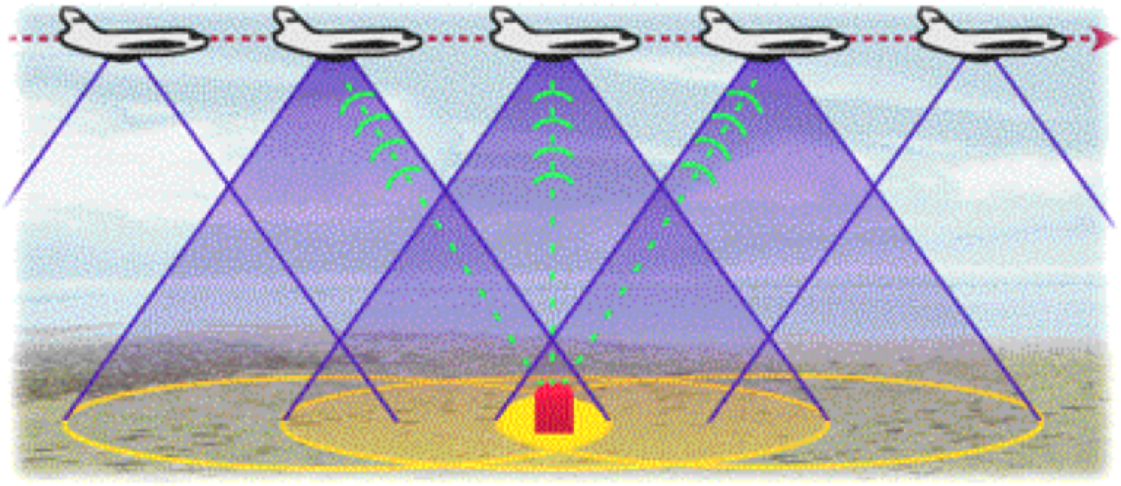

Figure 1.3: Illustration of Synthetic Aperture Radar. Reprinted from [3].

(DBI) to measure the vector velocity in a single pass of the aircraft. DBI combines two ATI-SARs, one squinted forward from broadside and the other squinted aft. Thus, each scatterer is imaged by two beams and two radial velocity components in different directions are obtained, allowing the reconstruction of the surface vector velocity during a single flight.

Frasier and Camps [16] investigated and further developed the concept of DBI. They described the principle of operation of an airborne instrument designed to measure sea surface currents in a single pass. After that, the first dual-beam ATI-SAR was designed and built by the University of Massachusetts [17]. Toporkov et al. [18] presented the first examples of single-pass vector velocity retrievals achieved with this new dual-beam system and provided their qualitative assessment. Estimates of surface current vectors by the dual-beam system in the coastal region around barrier islands during high tidal flow were compared with predictions by the U.S. National Ocean Service. Discrepancies of up to 0.5 m/s in velocity magnitudes were observed. Velocity retrievals for the same area based on the data from two different tracks showed good consistency, indicating the robustness of the DBI principle.

Since the first demonstration of vector retrieve with a single-pass dual-beam InSAR system, the DBI principle has been implemented in various projects for ocean surface current

velocity mapping. An airborne Wavemill proof-of-concept campaign [19] took place in the tidally-driven Irish Sea in 2011 with the configuration of a Ku-band dual-beam ATI-SAR. The data was collected during a maximum ebb tidal flow and the current velocity retrieval with the data suggests a large discrepancy compared with the in-situ measurements. It was shown that the difference between the radar and in-situ measurements is mainly due to two major error sources. The first part is the systematic error from the instrument or platform itself. The second part is the contribution of wind-wave surface velocity artifact to the measured Doppler velocity, which must be removed to retrieve the surface current vectors with sufficient accuracy.

More recently, the Applied Physics Laboratory at the University of Washington (UW-APL), in collaboration with Artemis Inc., has developed a miniaturized dual-beam ATI SAR, which can be installed on a small aircraft or UAV [20]. The system's low size, weight and power significantly reduce the operation cost and enable one to fly it more frequently for airborne experiments. A number of field experiments with this microASAR have been conducted over different tidally-driven inlets [21–25]. The ATI-SAR derived surface current vectors were compared with the in-situ measurements made by surface drifters at the New River Inlet (NRI) in North Carolina and Mouth of Columbia River (MCR) [26]. Discrepancies in both vector magnitude and direction were observed. Note that represent discrepancies between the airborne InSAR and in situ measurements with the term "errors" throughout the study. The InSAR measurement errors on surface currents velocity result from two main categories: error from radar system or platform itself and contribution from the wind-wave surface velocity artifact to the InSAR measured Doppler velocity. The scope of this study focuses on the first category error analysis, i.e., an analysis of systematic phase errors that come from the radar and aircraft which directly translate to the measured radial velocity errors for ATI-SAR.

The accuracy of ocean currents retrieval depends of the interferometric phase processing of ATI-SAR. Ideally, the interferometric phase measured by ATI-SAR results from the contribution of ocean surface motion due to the currents and waves. However, the measured ATI

phase always incorporates phase errors from the InSAR system itself and also the aircraft platform in real situations. For example, for a scene where all the scatterers are stationary, the corresponding interferometric phase measured by InSAR should be zero. The actual measured ATI phase rarely satisfies this condition, which indicates certain phase errors from the instrument or platform itself. This systematic phase error can be introduced by various different sources, making the analysis and the entire phase error calibration very complex. Moreover, no comprehensive phase error analysis for dual-beam ATI-SAR has been reported in current literatures.

Starting from the phase error observed in the interferogram for a stationary farmland, our study divided the observed phase error into three sub-categories for analysis. The first sub-category is the range-dependent phase fluctuations which has been reported to be caused by atmospheric phase screen, multi-path reflection of the aircraft body or the imbalance between SAR receive channels. Various studies [27, 28] showed that the measured repeat pass ATI-SAR phase fluctuations versus range due to the change of the atmosphere condition during the two measurements. However, the atmospheric effect is not significant for our system with a very short temporal baseline (8.7 ms). [29] analyzes the multipath effect in the airborne interferometric SAR which introduces phase undulations in the range direction of the SAR image. This effect is a result of the superposition of the time-delayed replica of the direct signal with the signal itself. They propose a multipath model that is used to estimate unknown parameters in the model to correct the multipath phase disturbances. A similar effect has been studied in [30], where the multipath component of the signal from the airborne InSAR system causes oscillating phase errors and hence height errors. Although the multi-path effect is common for airborne radars, our study demonstrated that the range-dependent phase fluctuations in our frequency modulated continuous wave (FMCW) SAR system is mainly due to the imbalance between the receive channels of the FMCW SAR, rather than the multi-path reflections from the body of the aircraft.

The second sub-category is shown as the phase offset which varies slowly in the range direction of the interferogram. This phase offset maybe induced by the imbalance between

the phase array antenna's phase pattern or the difference between the channel's electric path length. [31] demonstrated for the first time the usage of phase patterns in an operational interferometric SAR mission. It derives the mathematical background of the phase patterns and provides the calibration approach for the different phase pattern calibration aspects. Our study retrieved the phase difference between antennas as a function of antenna elevation offset angle. Instead of measuring the antenna pattern of each antenna, we estimated the antenna phase imbalance using the interferometric phase and antenna elevation offset angle data from an area with only stationary land scatterers.

The third sub-category is seen as the phase undulations in the azimuth or along-track direction of interferogram. This kind of phase error could be caused by the uncompensated motion errors due to uncertainties in the inertial navigation system (INS) measurement. [16] first mathematically derived the sensitivity of surface velocity estimate by dual-beam squinted ATI-SAR to small random errors in platform velocity and attitude. The effects of residual uncompensated motion errors on the phase errors for airborne ATI-SAR has not been investigated until recently [32]. They found out that the phase errors caused by uncompensated motion errors based on center-beam approximation (CBA) and reference DEM approximation during SAR motion compensation (MC) cannot be neglected when the DEM errors exceed 25 meters. My work studied the effects of uncompensated motion errors as well as the DEM uncertainties on interferometric phase of squinted ATI-SAR for the first time. Simulation shows that uncompensated motion error does account for the majority of the observed azimuthal phase undulations.

All of the above mentioned possible error sources will be analyzed in this study and corresponding phase calibration schemes will be presented. The goal of this study is to improve the understanding of the system phase errors from the airborne dual-beam squinted ATI-SAR system and come up with effective phase calibration approach for each important phase error source to improve the system accuracy for ocean surface currents mapping.

1.3 Organization

This dissertation is organized as follows. In Chapter 2, we review the basic principle of along-track interferometry and the UW-APL dual-beam microASAR system used in this study. The phase errors observed in the interferogram is presented and characterized as difference error source categories. Chapter 3 studies the cause for the observed range-dependent phase fluctuations and corresponding calibration approaches. Chapter 4 studies the antenna phase imbalances which translate to the residual ATI phase error in range after phase ripple calibration. The effect of global navigation satellite system/inertial measurement unit (GNSS/IMU) uncertainty in aircraft attitude measurement and the Digital Elevation Model (DEM) error on the ATI phase measurement are studied in Chapter 5 and Chapter 6. In Chapter 7, an initial study on the contribution of ocean waves to the ATI-SAR Doppler measurement is presented. Finally, the summary of this study as well as its contributions are discussed in Chapter 8.

Chapter 2

THEORETICAL BACKGROUND

This chapter covers the theoretical basics for along-track interferometric SAR processing for ocean surface currents estimation and the descriptions of the airborne radar system.

2.1 ATI-SAR Measurements

The ATI-SAR is a synthetic aperture radar with two antennas separated by a fixed distance along the platform flight direction. Figure 2.1 provides a schematic illustration of the ATI-SAR configuration [4]. The two antennas image the same area at slightly different times (time lag τ) and record the phase information of the backscattered signals. The phase difference between these two measurements is proportional to the Doppler shift of the backscattered signal and, thus, to the radial velocity between the radar and the scatterers, which is given in Equation (2.1) [11]

$$\Phi = \omega_D \tau = \frac{4\pi B}{\lambda V} u_r = \frac{2kB}{v_p} u_r \tag{2.1}$$

where ω_D is the Doppler shift, v_p is the platform velocity and λ is the incident electromagnetic wavelength. Here we assume both antennas are transmitting and receiving simultaneously, indicating that $\tau = \frac{B}{v_p}$. Thus, one can estimate the velocity of the target from the phase difference by combining two complex images from the two receivers.

The phase difference, also known as the interferometric phase, for each pixel in the two complex ATI-SAR images is considered to be the phase of the autocorrelation function of the backscattered signal from that particular pixel at the time lag τ [33]. The auto correlation

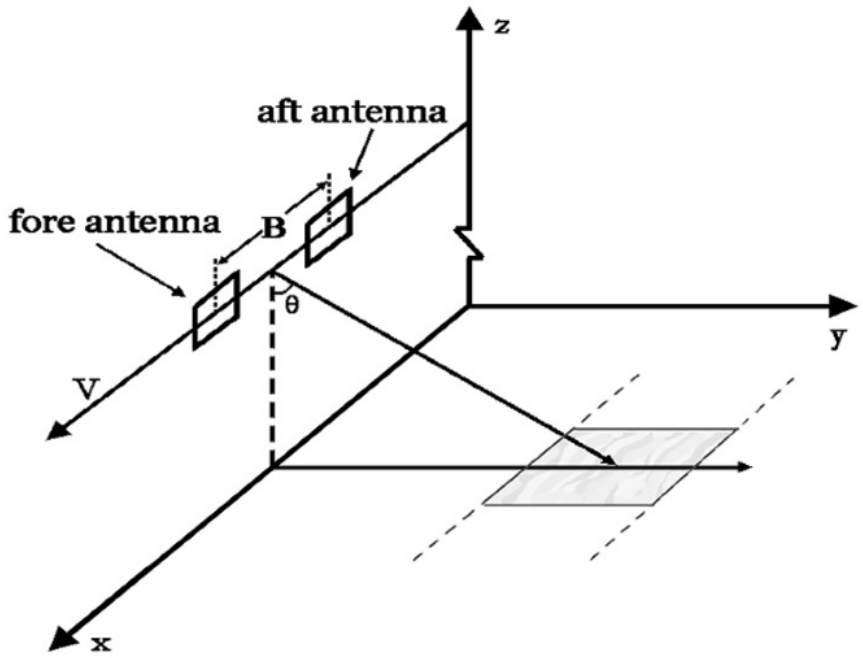

Figure 2.1: Schematic illustration of the ATI-SAR. Reprinted from [4].

function is given by

$$R(\tau) = E\{B(t)B^*(t-\tau)\} \tag{2.2}$$

where $B(t)$ is the backscattered field from a particular pixel at time t. The autocorrelation of the backscattered field is related to the Doppler spectrum $S(\omega)$ by

$$R(\tau) = \frac{1}{(2\pi)^{1/2}} \int_{-\infty}^{\infty} e^{i\omega\tau} S(\omega) d\omega \tag{2.3}$$

where $S(\omega)$ is a real function. If $\omega\tau$ is much smaller than 1 over the frequency band of $S(\omega)$, then the phase of the autocorrelation function is given by

$$\Delta\phi = \arg\{R(\tau)\} \approx \frac{\int_{-\infty}^{\infty} \omega S(\omega) d\omega}{\int_{-\infty}^{\infty} S(\omega) d\omega} \tau = \bar{\omega}\tau = 2\pi \bar{f_D} \tau \tag{2.4}$$

where $\bar{f_D}$ is the mean Doppler frequency. This equation relates the phase difference measured

by ATI-SAR to the mean Doppler frequency weighted with the Doppler spectrum.

The RCS-weighted mean Doppler frequencies can be decomposed into four contributions as [4]

$$\langle f_{D\pm} \rangle_\sigma = f_D^c + f_{D\pm}^b + f_{D\pm}^m + f_D^o \tag{2.5}$$

where f_D^c denotes the contribution of the mean surface current, $f_{D\pm}^b$ represents the contribution of the phase velocities of the two Bragg wave components, $f_{D\pm}^m$ represents the contribution of the correlated RCS variations introduced by the correlation between orbital motions and tilt and hydrodynamic modulation of the backscattered power, and f_D^o is the only periodic component part caused by the real orbital velocities of the long gravity waves. $f_{D\pm}^m$ and f_D^o are the contributions of the long ocean waves.

$$\langle U \rangle_s = \frac{\lambda}{4\pi\tau} \langle \Delta\phi \rangle_s = \frac{\lambda}{2} \{ f_D^c + f_D^m + (2A-1) f_{D^+}^b \} = u_r^c + u_r^m + u_r^B \tag{2.6}$$

where u_r^c is the contribution of the average surface current velocity, u_r^m is the velocity introduced by the orbital motions of longer waves, and u_r^B is the net Bragg-wave phase velocity.

2.2 System Description

As stated earlier, the conventional ATI-SAR only measures one line-of-sight component of the velocity between the radar and the scatterer during a single pass of the aircraft. To retrieve the two-dimensional surface velocity vector, it requires two intersecting passes and each pass provides an estimate of the velocity component at one direction. The dual-beam system enables the reconstruction of the surface velocity vector during a single pass. The UW-APL microASAR is a dual-beam system implemented with two miniaturized squinted ATI-SARs and an INS. Each radar consists of an FMCW transceiver and data acquisition unit, and three flat-panel antennas. The antennas are mounted under the belly of a Cessna 172 aircraft. A concept drawing showing the antennas for the two squinted ATI-SARs is shown in Figure 2.2. The port-side antennas are squinted aft of the side-looking direction, and the starboard-side antennas are squinted forward. The flat-panel antennas are mechanically rotated in the horizontal plane, and tilted in the squinted plane. The squint angle (ϕ_s)

is 30 degrees measured in the horizontal plane, and the elevation angle (θ_i) is 60 degrees, measured between the radar looking direction and nadir direction. The transceivers and data acquisition units are the microASARs built by Artemis, Inc. [6]. The bandwidth of the transmitted signal is 80 MHz and the resulting slant range resolution is 1.875 m. The frequency bands of the radars are separated by 40 MHz, allowing the radars to operate simultaneously.

Figure 2.2: Concept drawing of antenna installation under the belly of a Cessna 172 aircraft.

2.3 Dual-beam ATI-SAR Measurement

The geometry of dual-beam interferometry is shown in Figure 2.3. During the flight, the dual-beam system first observe the scene with its fore-looking ATI-SAR and then, after a short period of time, with its aft-looking counterpart. The interfeorgrams for fore and aft squinted radars can be calculated from the corresponding coregistered complex image pairs. With Equation (2.1), we obtain two Doppler velocity measurements from the same point on

the surface: the first, u_r^+ at time t_1, by the forward-squinted antenna, and the second u_r^-, at time t_2, with the aft-squinted antenna. The radial velocity measurement is an estimate of the mean Doppler shift of the surface scatterer detected by the radar. Based on the composite ocean surface scattering theory [4], the mean Doppler shift will be the sum of the contributions from Bragg-resonant wave phase velocity, the orbital motions of long gravity waves, and surface current Equation (2.6).

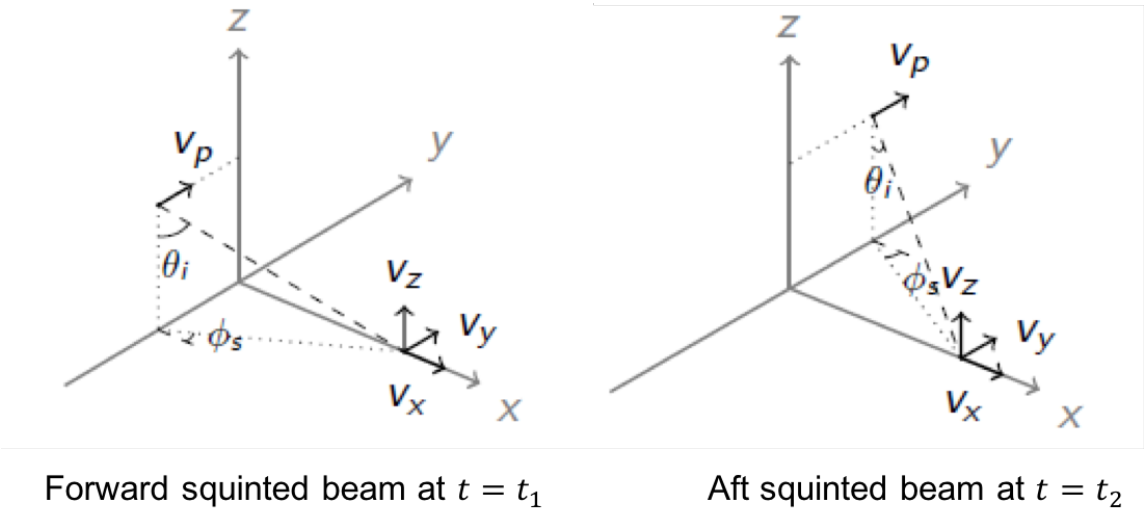

Figure 2.3: Dual-beam ATI-SAR measurement geometry.

The resulting radial velocity is a linear combination of the three components of the surface velocity vector (v_x, v_y, v_z) and is given by

$$\begin{aligned} u_r^+ &= v_x \sin\theta_i^+ \cos\phi_s^+ + v_y \sin\theta_i^+ \sin\phi_s^+ - v_z \cos\theta_i^+ \\ u_r^- &= v_x \sin\theta_i^- \cos\phi_s^- + v_y \sin\theta_i^- \sin\phi_s^- - v_z \cos\theta_i^- \end{aligned} \tag{2.7}$$

where the forward- and aft-squinted incidence angles (θ_i^+ and θ_i^-) are measured in the vertical plane, and the forward- and aft-squinted angles are measured in the horizontal plane. Assuming that the contribution from the vertical velocity component is small, the horizontal

surface components are estimated from the dual-Doppler measurements using

$$\begin{bmatrix} v_x \\ v_y \end{bmatrix} = \frac{1}{D} \begin{bmatrix} \sin\theta_i^- \sin\phi_s^- & -\sin\theta_i^+ \sin\phi_s^+ \\ -\sin\theta_i^- \cos\phi_s^- & \sin\theta_i^+ \cos\phi_s^+ \end{bmatrix} \begin{bmatrix} u_r^+ \\ u_r^- \end{bmatrix} \tag{2.8}$$

where

$$D = \sin\theta_i^+ \sin\theta_i^- \sin(\phi_s^- - \phi_s^+) \tag{2.9}$$

Note that these equations allow for different incidence and squint angles for the different radars. At present, we do not attempt to remove the contribution to the surface velocity from long gravity waves.

2.4 Field Experiments and Observations

A number of field experiments have been conducted with the APL-UW dual-beam ATI-SAR system. An airborne campaign for the study of near shore ocean wave and current interaction was conducted at the New River Inlet (NRI) in North Carolina in May, 2012. The experiment site is a tidally driven inlet and the typical mean value of the current velocity ($\sim 0.7m/s$) in that region is greater than that in the region far away from the coast. The campaign lasted for about a month and ATI-SAR data was collected on different days during the maximum ebb and flood periods of the tides. The in-situ measurement of the surface current was provided by the surface drifters [34] developed by APL-UW. The current vector velocity retrieved by the radar with Equation (2.8) was compared with the measurements made by the surface drifters. Errors in both magnitude and direction have been observed. Figure 2.4 shows the interferogram generated from the data collected at the NRI on May 10, 2012 during its maximum ebb period, from which we can clearly observe the structure of the flow in the inlet. Note that the red color indicates the water is flowing from the inlet into the ocean. Furthermore, we observed range-dependent phase fluctuations over the land adjacent to the inlet, displayed as the blue and red alternating stripes. Since the land is stationary, the interferometric phase should be zero over the area. This range-dependent phase fluctuations suggests certain phase error introduced by the radar system or

platform itself and various field experiments demonstrated this phase offset is independent of surface properties. To better observe the range dependent phase offset, we ran another field experiment at a farmland area in Washington State. Figure 2.5 shows the google earth image for the site. The corresponding interferogram for this site is shown in Figure 2.6. We can clearly observe the range-dependent phase fluctuations (red and blue stripes) in the inteferogram over stationary land scatterer. The phase fluctuations, caused by certain systematic phase error sources, need to be removed from the measured interferometric phase for accurate velocity estimate.

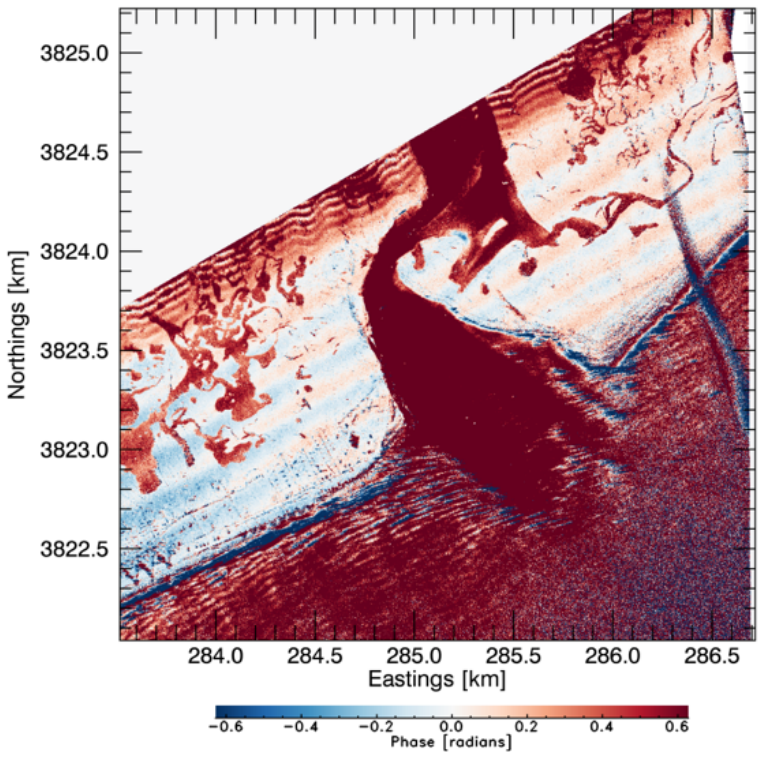

Figure 2.4: The interferogram for New River inlet in NC.

The phase offset exists in the observed farmland interferogram is consisted of not only the range dependent phase fluctuations but also the phase offset that varies slowly in the

Figure 2.5: Google earth image for the farm land test site.

range direction and the phase undulations that varies in the along-track direction. Thus, the observed phase error is actually a combination of errors from these three error sub-categories. Note that under the system configuration, one radians of phase error translate into 50 cm/s error in the radial velocity measurement. Figure 2.7 illustrates these 3 sub-categories of the observed phase error. Figure 2.7(a) shows the original interferogram. After we remove the phase fluctuations (RMS value of 0.2 rad) in range with our proposed calibration scheme, the remaining interferogram (Figure 2.7(b)) still shows a phase offset (RMS value of 0.7 rad) which varies slowly in range. Finally, after we estimated this slowly varying phase offset and applied it into the post-processing, the remaining interferogram (Figure 2.7(c)) still

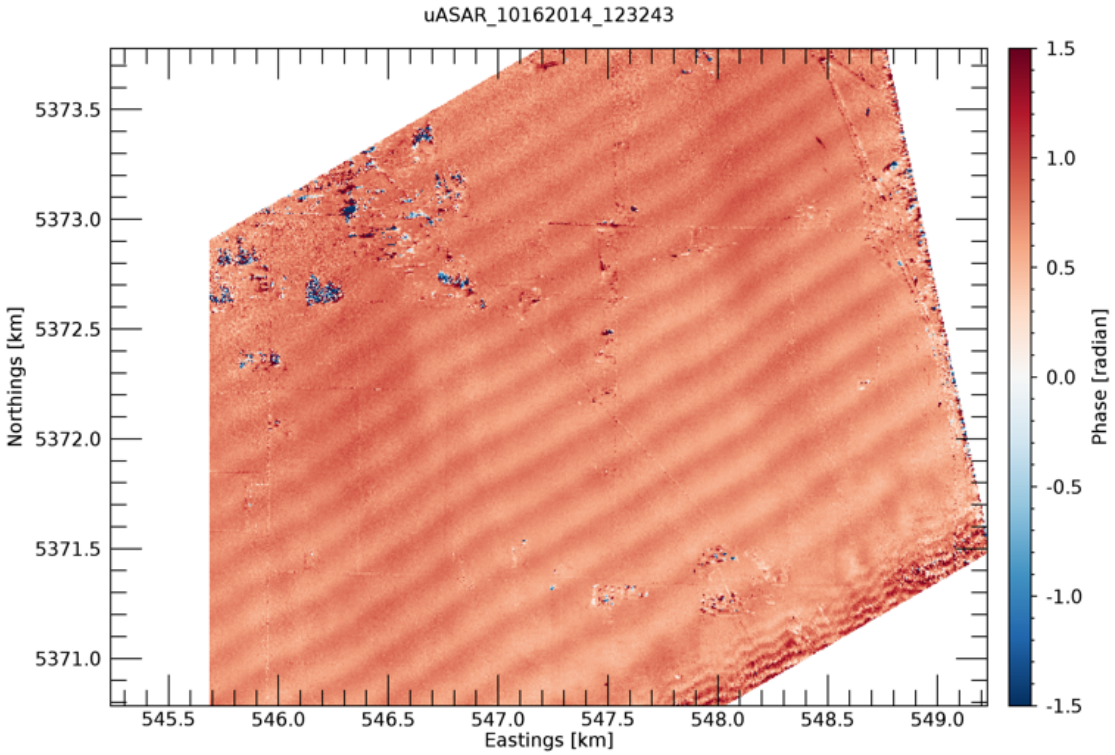

Figure 2.6: Interferogram for the stationary farmland area in WA, USA

shows the phase undulations in the along-track direction. The study will try to understand what are the possible error sources for explaining these 3 error categories and propose the corresponding calibration schemes to mitigate the phase errors.

2.5 Summary, Problem Statement, and Contributions

Based on the observation of phase error in the farmland interferogram presented in Chapter 2, this study tries to find possible error sources that can explain the observed interferometric phase error. From the discussion in Chapter 1 on the reported phase error sources in previous literatures, we find that no one has performed a detailed and comprehensive study of all possible systematic phase error sources for dual-beam squinted ATI-SAR. Every current

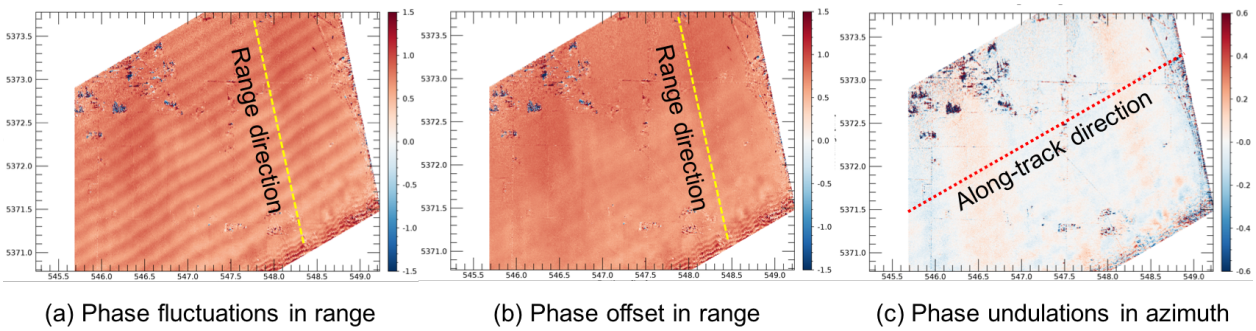

Figure 2.7: Observed phase errors for the stationary farmland area in WA, USA

literature we referred to reports only one or two specific phase error source that applies somehow to their own ATI-SAR system. Although a comprehensive error source analysis and the entire phase calibration can be very complex for such system, it is appealing if one can list all possible systematic or platform error sources and study the importance of each error source to understand which one dominates the phase error in ATI-SAR. Such study will provide theoretical bases for the error source analysis and signal calibration of airborne FMCW ATI-SAR for ocean surface currents retrieval.

Based on the literature review on the phase error sources in Chapter 1, we try to find out all possible error sources that can introduce the interferometric phase errors for ATI-SAR. We finally divided all the error sources we find into 4 different classes based on their own properties. The first class of error sources is due to system imperfections, which can include imbalance between receive channels, multi-path propagation due to on-aircraft reflection and imbalance between antenna phase patterns. The second class of error is due to insufficient system parameter knowledge, which can include insufficient knowledge on temperature, baseline between antenna and electric path length difference between channels. The third class of error sources is due to insufficient navigation system accuracy and the fourth class of error sources is due to insufficient digital elevation model (DEM) accuracy. The last two classes of error sources will result in residual phase error during the MC process for airborne ATI-SAR. Table 2.1 illustrates these 4 classes of error sources. 4 classes of error sources that

Table 2.1: Summary of 4 classes of error sources that can contribute to ATI-SAR systematic phase error

Class	**Error Sources**
Radar System Imperfections	Imbalance between receive channels
	Multi-path propagation due to on-aircraft reflection
	Imbalance between receive antennas
Insufficient System Parameter Knowledge	Temperature
	Electric path length difference between channels
Insufficient INS Accuracy	Uncertainties in aircraft attitude and velocity measurements by INS
Insufficient DEM Accuracy	Reference DEM deviates from true elevation
	Residual phase error during motion compensation

can contribute to ATI-SAR systematic phase error.

Based on the discussion so far, the research questions for this study can be as follows: (1) For each possible error source listed in Table 2.1, how much does it contribute to the observed phase error? (2) Which error source is more significant for our FMCW ATI-SAR system? (3) Can we come up with possible calibration approach to mitigate the effects?

My approaches to answer these questions includes mathematical analysis of the uncertainty of ATI-phase in terms of uncertainties of each related error source listed in Table 2.1. Then computer simulations will be performed to validate the theoretical analysis. We will run lab-controlled experiment and real data analysis for the phase calibration process. The following chapters will present my research approaches for the study of the 4 classes of error sources in Table 2.1.

Chapter 3

CALIBRATION OF THE PHASE FLUCTUATIONS IN DUAL-CHANNEL FMCW SAR

This chapter introduces a phase calibration scheme for an interferometric FMCW synthetic aperture radar (SAR) to correct range-dependent phase errors in FMCW SAR interferograms. We demonstrate that the receiver filters operating on the FMCW beat frequency signal account for most of the phase mismatch between the different receiver channels. The scheme presented estimates the phase error in each channel. Results of the scheme for three estimation approaches (curve fitting, joint least squares, and maximum likelihood) for two different phase models are presented. The results are quantified by computing the reduction in spectral energy associated with the phase mismatch. We find that phase error can be reduced by 14 dB using the approach. Note that most of the contents in this chapter are cited from one of the author's publications in 2018 [35].

3.1 Problem Description and Related Work

Airborne along-track interferometric synthetic aperture radar (ATI-SAR) is one technique used to estimate high-resolution ocean surface currents [11, 12, 14, 33, 36] and other dynamic surface features [37]. These ATI-SAR systems have in the past been large instruments that require medium-sized to large aircraft from which to operate. In the past decade, small synthetic aperture radars have been developed by various groups [6, 38, 39]. These systems are often frequency-modulated continuous-wave (FMCW) radars that can be flown from significantly smaller and lower-cost platforms than previous SAR systems. More recently, FMCW SAR has been operated in interferometric modes to estimate surface current vector velocity [22, 26]. However, since the radial velocity component measured by ATI-SAR is

proportional to the interferometric phase, phase matching between radar receivers is critical for accurate current retrieval. For example, the data collected with this FMCW SAR system showed range-dependent phase fluctuations in the interferograms [5].

Phase errors in interferometric SAR systems can arise from different sources and need to be corrected in the data processing to provide accurate velocity estimates. [29] analyzes the multipath effect in the airborne interferometric SAR, which introduces phase undulations in the range direction of the SAR image. This effect is a result of the superposition of the time-delayed replica of the direct signal with the signal itself. They propose a multipath model that is used to estimate unknown parameters in the model to correct the multipath phase disturbances. A similar effect has been studied in [30], where the multipath component of the signal from the airborne InSAR system causes oscillating phase errors and hence height errors. They present a model describing the impact of the multipath error in the system and apply the model to deal with the phase errors to achieve a high geodetic fidelity. Although the phase disturbance due to the multipath effect is common in airborne SAR systems, we demonstrate that the observed phase deviations with our FMCW system is not dominated by the multipath effect but the phase mismatch between receivers. Note that in this work, we do not address the absolute phase calibration problem addressed by other studies [40–42].

In this chapter, we review the FMCW implementation of the dual-channel along-track FMCW SAR used in this study, and show an example of range-dependent phase offset observed in the interferogram from a test site. To calibrate this phase offset in the FMCW system, a lab-based experiment was performed and different approaches for estimating the phase of each channel were studied. All approaches used account for the phase ripple throughout the receiver, including the front-end electronics and the digital subsystem. This work has relevance to implementing compact low-cost FMCW interferometric SAR systems for geophysical research measurements.

3.2 Calibration Approach

3.2.1 FMCW SAR Implementation

The dual-channel FMCW radar utilized for ocean surface current mapping is the microASAR transceiver developed by Artemis Inc. Figure 3.1 shows a simplified block diagram of the system. The received signals are first mixed with a frequency-offset copy of the transmitted signal, and the result is the beat frequency between the reference chirp and the scattered signals. The beat frequency depends on the round-trip time from the radar to the scatterer. This signal is filtered with a surface acoustic wave band-pass filter (SAW BPF) to attenuate the direct transmission from transmit to receive antennas. The resulting signal is down-converted to baseband, filtered and digitized.

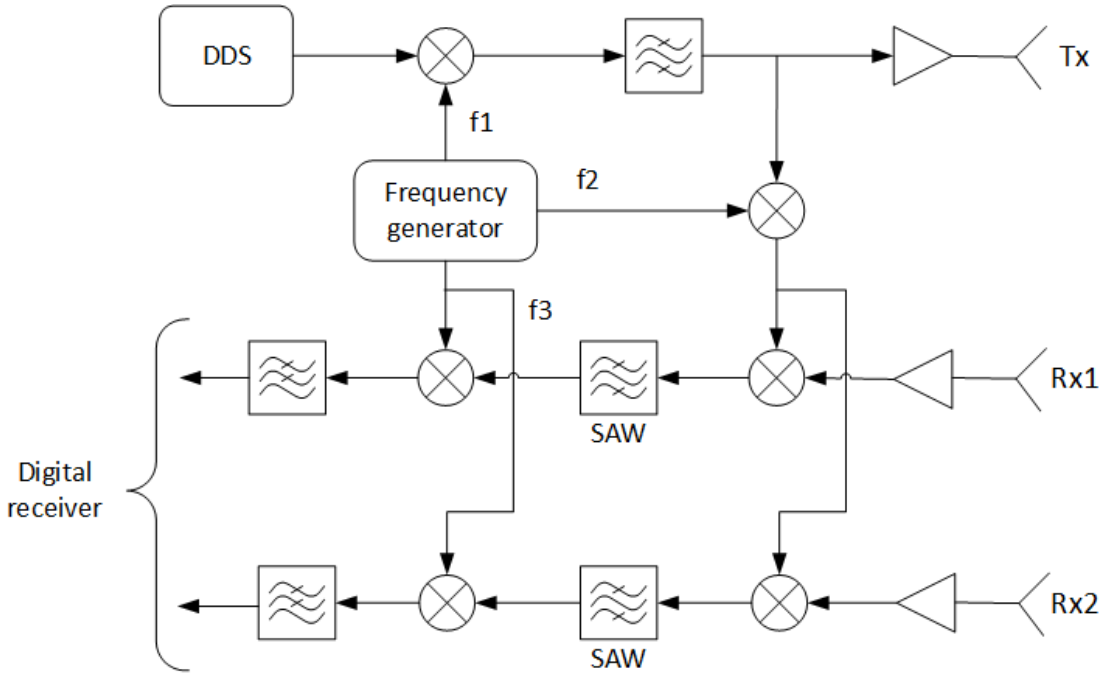

Figure 3.1: Simplified block diagram of the microASAR transceiver. Reprinted from [5].

The range-compressed data are then processed with a backprojection algorithm using a digital elevation model (DEM). SAR images are generated from the data for both channels,

and the interferogram is formed. The interferogram shown in Figure 3.2 was generated from data collected over farmland in Washington (WA), where most of the area is stationary and should have zero along-track interferometric phase. Any cross-track component of phase in the interferogram should be small as a DEM is used in the the SAR image formation. The aircraft was flying from east to west during data collection and imaged the northbound area. The phase ripples in the interferogram appear to be a function of slant range, where variations in the distance of the ripples from the radar vary with attitude (pitch, roll, yaw) changes of the aircraft.

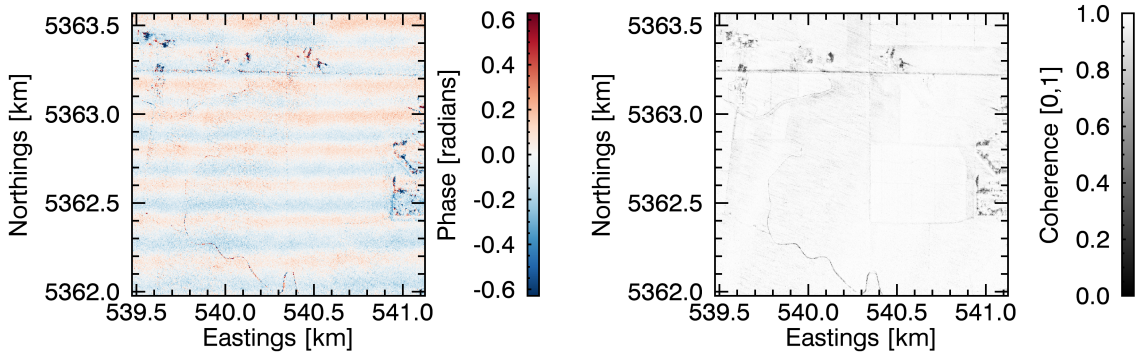

(a) Uncalibrated

(b) Coherence

Figure 3.2: Interferogram in UTM coordinates for UTM Zone 10 showing the phase ripple over land at a stationary farmland area in WA (a) and the corresponding coherence image (b). The displayed phase range is from -0.6 radians to 0.6 radians.

Although there is significant isolation between the transmit and receive antennas (estimated to be 60 dB by the manufacturer of the antennas), strong feedthrough between the transmit and receive antennas dominates the low-frequency part of the dechirped signal spectrum. To minimize the dynamic range requirements of the receiver, it is desirable to remove the strong feedthrough signal as early as possible in the receiver electronics. The microASAR removes the feedthrough by utilizing a SAW BPF, which was selected due to its

sharp transition to the stopband region. The feedthrough removal is achieved by carefully choosing the frequency of the crystal oscillator so that the feedthrough component in the dechirped signal is mixed down to the first null of the SAW BPF. This feedthrough removal is illustrated in Figure 3.3.

Since the SAW filters have a sharp cutoff response (and therefore ripple in the passband), we hypothesize that mismatches in the phase response of the SAW filters account for the majority of phase ripple between the receivers. This hypothesis seems reasonable because the SAW filters operate on the FMCW beat frequency signal, in which frequency is proportional to distance of the reflections from the radar, so any frequency-dependent phase ripple in the filters will produce a range-dependent phase ripple in interferograms. In this hypothesis, we make the assumption that any frequency-dependent phase ripple in the front-end components affect all FMCW beat frequencies roughly in the same way (see Appendix A).

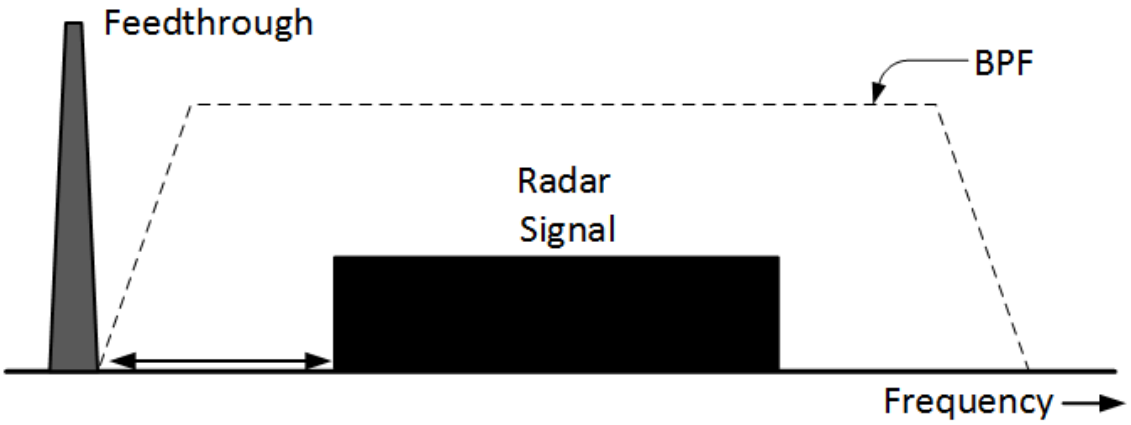

Figure 3.3: microASAR dechirped signal spectrum and suppression of the feedthrough signal by the SAW bandpass filter. Adapted from [6].

3.2.2 Calibration Setup

The idea of phase calibration is to estimate the phase ripple in each channel and apply the estimated ripple to each SAR image after range compression and before time-domain backprojection during SAR image formation. In this way, each formed SAR image is phase calibrated before the interferogram is generated. Hence, we decided to estimate the phase ripple for each channel rather than to compute the phase difference between the two channels. Note that this idea can be applied to the phase calibration of multichannel interferometric FMCW systems. The calibration approach developed in this study is to inject a single tone signal simultaneously into both receiver channels and estimate the phase of the output signal (Figure 3.4). The frequency of the injected signal is chosen so that the result is a chirp signal whose spectrum covers the full bandwidth of the SAW filter after mixing with the transmitted signal. The resulting chirp provides a swept-frequency signal that is used to characterize phase response of the components downstream of the mixer in the receiver (in the same way as is done with a network analyzer). We believe the unique advantage of the calibration method makes it applicable to other FMCW SAR systems as well. After being filtered by the SAW BPF, the chirp is down-converted to baseband, filtered and digitized using the radar electronics. The radar parameters for the calibration setup are listed in Table 3.1. This approach can be easily implemented in a flight configuration by using a high-precision oscillator and a phase locked loop (PLL) as a frequency synthesizer to generate the calibration tone signal.

3.3 Phase Estimation Approaches

The output signal of each receiver channel is a chirp signal whose phase is a quadratic function in terms of time, and the phase ripple in that channel. Mathematically, this signal is expressed as

$$S(t) = \cos(\phi(t)) = \cos\left(\omega_0 t + \frac{1}{2}at^2 + \phi_0 + \Phi_r(t)\right) \ , \tag{3.1}$$

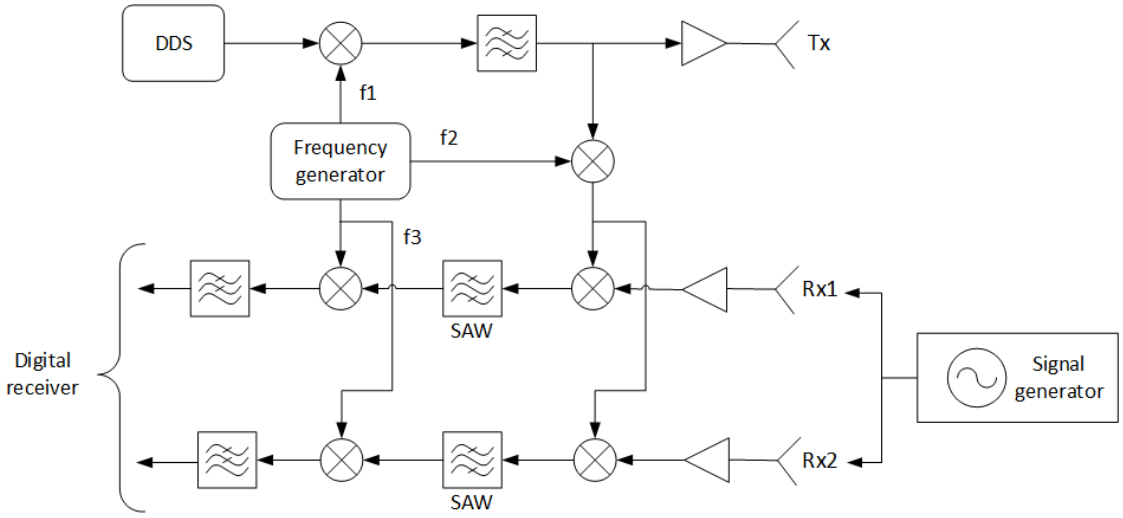

Figure 3.4: Simplified diagram for calibration setup. A single tone generated by signal generator is injected into both receiver channels. Adapted from [7].

where a denotes the chirp rate, ω_0 denotes the initial frequency and ϕ_0 is the initial phase. $\Phi_r(t)$ represents the phase ripple of the channel which is also a function of time because the beat frequency of an FMCW radar increases linearly with time delay to scatterer. $\Phi_r(t)$ represents the phase ripple caused by nonlinearities in the phase response of SAW filters of the receiver channel, which should be a function of the beat frequency. Note that the beat frequency of an FMCW radar increases linearly with the time delay of the pulse, we can write the phase ripple as a function of time. To retrieve the ripple in the channel, we estimate the parameters in the phase model.

We consider two approaches to estimating the ripple. The first uses a phase model (Phase Model 1) that does not include the ripple term, and the second (Phase Model 2) that does include this term:

$$\text{Phase Model 1: } \Phi(t) = \frac{1}{2}at^2 + \omega_0 t + \phi_0 \ ,$$
$$\text{Phase Model 2: } \Phi(t) = \frac{1}{2}at^2 + \omega_0 t + \phi_0 + \Phi_r(t) \ .$$

The estimation approaches associated with the first phase model are indirect estimates of

Table 3.1: List of microASAR parameters.

Parameter	Value	Unit
Theoretical chirp rate	-7.5671e+11	rad/s^2
Transmitted chirp frequency	5368.76–5388.76	MHz
Chirp bandwidth	20	MHz
Theoretical initial frequency	3615898	rad/s
Calibration signal frequency	5378.76	MHz
SAW BPF bandwidth	16.5	MHz
Sampling rate	24.485	MHz
Pulse repetition frequency	749.969	Hz

the phase ripple. Namely, we estimated the parameters a and ω_0 in the phase model which does not include the ripple, and then subtract the estimated phase from the measured phase. The residual should be the phase ripple we are trying to estimate. Note that the estimation of the initial phase is not strictly required since it only contributes to a constant phase offset, which can be compensated later and does not affect the trend of phase variations. In the case of Phase Model 2, we model the phase ripple $\Phi_r(t)$ as a specific function of time, and the estimation problem becomes one of estimating the parameters in Phase Model 2, i.e., a, ω_0 and the parameters in the ripple function.

In this section of the paper, we focus on estimation schemes and results using Phase Model 1, and only present results with Phase Model 2 in Section 3.4 of this chapter. The reason for this organization of the material is that we use the ripple estimation results from Phase Model 1 to derive an analytic function for the ripple term needed for Phase Model 2.

3.3.1 Estimation Using Least-Squares Curve Fitting

The first approach taken to estimating the phase model parameters is to use least-squares curve fitting [43–45]. We estimate the parameters of the quadratic phase in Equation (3.1), by finding the set of parameters which minimizes the squared error between the estimated and measured signals. Applying this approach directly results in a nonlinear least-square problem which requires one to solve iteratively [46]. An alternative is to "linearize" the problem by unwrapping the phase. [47] has proved that this approximation is valid for high signal to noise ratios (SNR). Simple linear least-squares curve fitting techniques may then be used. In this study, a least-squares curve fitting procedure named MPFIT which uses the Levenberg-Marquardt technique [45] to solve the least-squares problem was performed to obtain the estimates of the parameters in Phase Model 1. The procedure fits the phase model to the measured phase data points and returns the best-fit parameters. The measured phase is extracted from the analytic signal created from the output signal in Equation (3.1). [48] details the way of computing the analytic signal via Hilbert transform [49] and FFT:

$$Z(t) = A(t)e^{j\Phi_m(t)} = S(t) + j\mathcal{H}\{S(t)\} \ , \tag{3.2}$$

where $Z(t)$ is the complex analytic signal with the same phase as $S(t)$ and $\mathcal{H}\{\cdot\}$ denotes the Hilbert transform. The measured phase $\Phi_m(t)$ is obtained by taking the argument of the analytic signal and then unwrapping it

$$\Phi_m(t) = \text{unwrap}\{\arg(S(t))\} \ . \tag{3.3}$$

The difference between the measured and the fitted phase is the phase ripple in the receiver channel we are trying to characterize. Since the beat frequency and target range are both linear functions of time, the phase ripple can be easily expressed as a function of frequency or range.

Computer simulations with the curve fitting approach for phase estimation were performed, in which we simulated the phase ripple $\Phi_r(t)$ for each channel as a combination of sinusoids. Then we added white Gaussian noise to the signal model in Equation (3.1). We

estimated the phase ripple with curve fitting approach and compared with our simulated phase ripple to compute the estimation errors. The simulations were performed under different noise levels and the root mean squared (RMS) difference between the simulated phase ripple and estimation results was computed during each simulation. We ran 1000 simulations at each noise level and the mean value of the RMS differences are listed in Table 3.2. For the ATI SAR used in this study, a phase error of 1 radian will introduce a radial velocity error of $50\,\mathrm{cm\,s^{-1}}$, which is significant compared with the typical values of ocean surface currents. Simulation results show that with an SNR of 25 dB, the phase estimation error is around 0.06 radians, which corresponds to a velocity error of around $3\,\mathrm{cm\,s^{-1}}$ for our system parameters. When the SNR drops below 15 dB, the phase error increases to more than 1 radian. Hence, the calibration procedure requires a calibration signal SNR above 25 dB for acceptable ocean current velocity measurements.

Table 3.2: RMS errors (in radians) of phase ripple estimation for simulations with different SNRs.

	Curve Fitting		Joint Estimation		MLE	
SNR (dB)	Channel 0	Channel 1	Channel 0	Channel 1	Channel 0	Channel 1
25	0.0616	0.0618	0.0613	0.0618	0.0613	0.0619
20	0.1034	0.1036	0.1033	0.1037	0.1035	0.1037
15	0.1917	0.1917	0.1948	0.1948	0.1825	0.1828
10	1.7601	1.7747	2.2822	2.2844	0.4754	0.4749

3.3.2 Joint Estimation Using Least Squares

The curve fitting approach estimates the parameters of the phase model for each channel separately. However, the injected signal for each receiver channel is the same and hence the estimated parameters ω_0 and a in the phase model must be the same for both channels. In the curve fitting approach, we did not exploit this fact. To take advantage of all available information and to constrain the estimation problem better, we derived an approach to jointly estimate the phases for both receiver channels. The phase model for each channel used for joint estimation has the form:

$$\Phi_0(t) = \frac{1}{2}at^2 + \omega_0 t + \phi_0$$
$$\Phi_1(t) = \frac{1}{2}at^2 + \omega_0 t + \phi_1 \ ,$$

where ϕ_0 denotes initial phase of the output signal in channel 0, and ϕ_1 denotes the initial phase of the output signal in channel 1. The initial phase values for the two channels may be different due to differences in the receiver electronics. Assume we have M measured phase values from each channel. A matrix formulation of the phase model for joint estimation is

$$\Phi = Ap \ , \tag{3.4}$$

where Φ is a vector of $2M$ elements which contains the measured phases from both channels, A is a $2M \times 4$ predictor matrix whose first column corresponds to t^2, second column corresponds to t, third column corresponds to ϕ_0, last column corresponds to ϕ_1. p is a vector which contains the parameters to be estimated, i.e., a, ω_0, ϕ_0 and ϕ_1. From linear regression theory, the ordinary least squares estimate of the parameter vector p is given by [50]

$$\hat{p} = (A^T A)^{-1} A^T \Phi \ . \tag{3.5}$$

Using (3.5), we are able to jointly estimate the phase ripple for both receiver channels by calculating $\Phi - A\hat{p}$. The phase ripple estimates for each chirp record are then averaged to yield the desired result.

Simulations with this approach were performed with additive noise of different levels. The RMS values of estimation errors are provided in Table 3.2. The joint estimate scheme is expected to perform better than separate estimate in curve fitting. However, the simulation shows the errors for curve fitting and joint estimation are very close at high SNRs. This is a little surprising since the joint approach takes advantage of more information and is expected to perform better. Again, the estimation error is around than 0.06 radians with an SNR of 25 dB for this approach.

3.3.3 Maximum Likelihood Estimation

The maximum likelihood estimation (MLE) of the parameters in frequency-modulated chirp signals has been studied in a number of papers [51–55]. The solution can be achieved by a simple generalization of MLE of the parameters of tones [51, 56] and results in estimators of similar format. Here we apply the MLE on the frequency and frequency rate to estimate the phase of the output signal from each channel. The derivation of the MLE for frequency rate and initial frequency of a complex chirp signal is given in [53]. To make use of the derived result to solve our problem, we first create the complex analytic signal with Equation (3.2). As stated in [53], the MLE of frequency rate a and initial frequency ω_0 is given by

$$\arg\max_{a,\,\omega_0} \left\{ \frac{1}{N} \left| \sum_{t=0}^{N-1} Z(t)\, e^{-j(\frac{1}{2}at^2+\omega_0 t)} \right|^2 \right\} . \tag{3.6}$$

It is also shown in [53] the peak of Equation (3.6) lies at or near the true values of a and ω_0, even at low SNR, which proves the robustness of the MLE solution.

Fast algorithms for searching the peaks has been discussed in [51, 55]. Since we have a rough idea of the theoretical values of initial frequency and frequency rate under our experiment, we are able to simplify the search by applying the exhaustive search for the two parameters in a predefined range.

We ran simulations to test the performance of the MLE approach for parametric estimation. The RMS values of estimation errors with MLE are provided in Table 3.2. Again, with an SNR of 25 dB, the estimation error with this approach is around than 0.06 radians.

Also note that even with an SNR below 15 dB, the RMS error of the MLE approach is less than 0.5 radians, which demonstrates the robustness of the MLE solution in comparison with curve fitting and joint estimation.

3.4 Phase Calibration Results

3.4.1 Estimated Phase Ripple

During the calibration experiment described in Section 3.2, we collected over 10,000 chirp records (pulses) from both receiver channels of the system. For each data record, we applied different estimation schemes discussed in Section 3.3 to estimate the phase and compute the phase ripple. Finally, we obtain the phase ripple for each channel by averaging the results from all the records in order to minimize the statistics of the solution.

The phase ripples of both channels calculated with different schemes are shown in Figure 3.5. From the derived results it's easy to tell that all three estimation approaches are consistent and yield very close results over most of the range. Note that at the near range region at about 1 km, the MLE result shows an abrupt phase jump which looks like the discontinuity in the filter phase response, or overshoot due to Gibbs phenomenon caused by the discontinuity at the ends of the digital output signal in Equation (3.1) and the finite-length Hilbert transform. In fact, since the signal to noise ratio (SNR) is very low at that near range part, we do not try to characterize the phase ripple of that region. We are more interested in the phase ripple at slant ranges greater than 1.5 km. Therefore, we discard data samples from the beginning and the end of the output signal during the curve fitting and joint phase estimation approaches. The results of all three approaches look identical for channel 0 estimation but deviate a little bit for channel 1. That the results look similar is not surprising since for large, complete data sets, both the least squares estimate method and the MLE methods should provide consistent results.

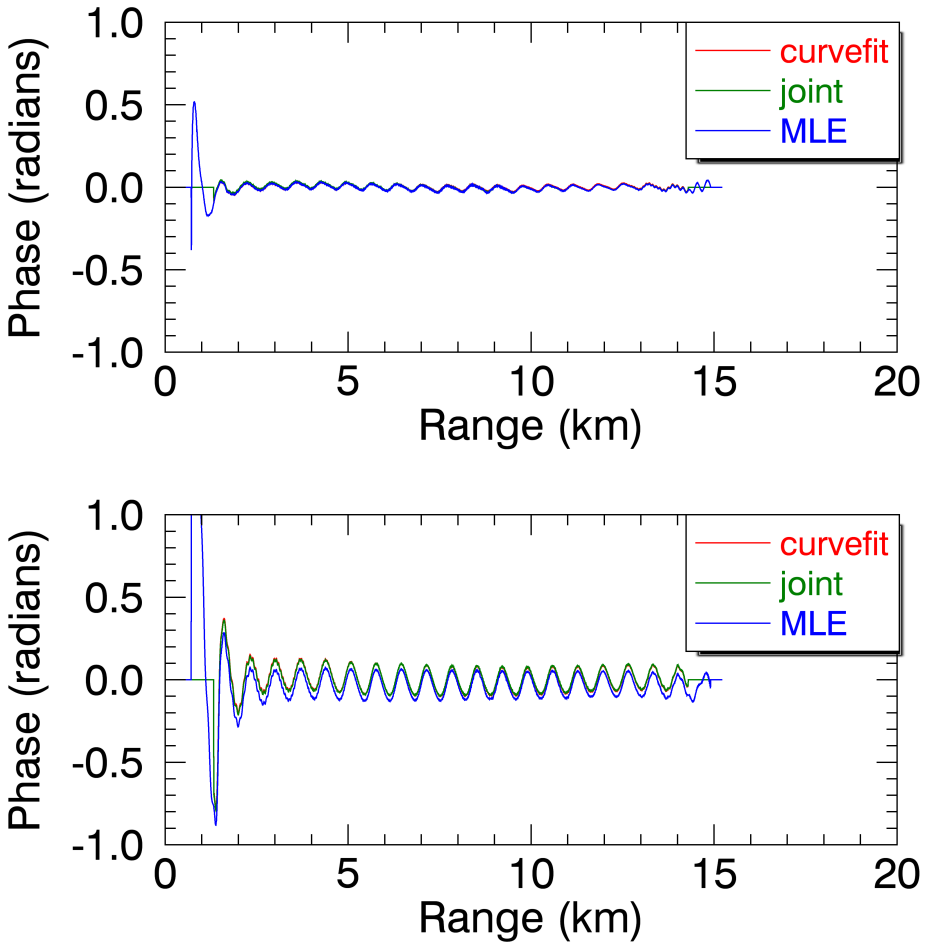

Figure 3.5: Estimated phase ripple from calibration setup. The top figure shows the phase ripple from channel 0 and the bottom one shows the phase ripple from channel 1. The plots with different colors correspond to different phase estimation approaches. Range values are computed by scaling the beat frequency by the chirp rate used to collect the farmland SAR data.

3.4.2 Calibrated Interferograms

After we computed the phase ripple of each receiver channel, we applied the results to the range compressed data of each channel in the SAR processor to compensate for the phase offsets observed in the uncalibrated interferograms. The calibrated interferograms with different calibration schemes along with the uncalibrated one, are shown in Figure 3.6. After comparing with the uncalibrated interferogram in Figure 3.6a, we observe that the phase ripple shown in the uncalibrated interferogram has been greatly attenuated and visually disappeared in most of the area. Moreover, the calibrated interferograms showed that these different approaches seemed to perform similarly in reducing the ripple level, although, one can still observe slight phase variations in range direction. However, all the proposed approaches have reduced the range-dependent phase ripple.

Note that these results confirm the the hypothesis presented in Section 3.2 that mismatches in the phase response of the SAW filters accounts for the majority of phase ripple between the receivers. Since the phase ripple in the interferogram can be greatly reduced by the calibration measurements which were done in the laboratory where multipath effects are not present, we can conclude that the phase ripple seen in the interfergram is mainly due to the phase response of the radar electronics at the FMCW beat-frequency stage instead of the multipath effect.

3.4.3 Quantification of Improvement

To quantify the reduction of the phase ripple in the interferograms after calibration, we performed a spectral analysis of the interferogram. Direct spectral estimates [57] with a Hanning taper of the phase series from a column in the uncalibrated interferogram and the calibrated ones are shown in Figure 3.7. The analysis of the interferometric phase series we chose from the column of the uncalibrated interferogram shows a period of around $0.18\,\mathrm{km\,cycle^{-1}}$, which would correspond to a peak at about $5.5\,\mathrm{cycles\,km^{-1}}$ in the spectral estimate. We observe a strong peak in the spectral estimate at about $5.5\,\mathrm{cycles\,km^{-1}}$ in

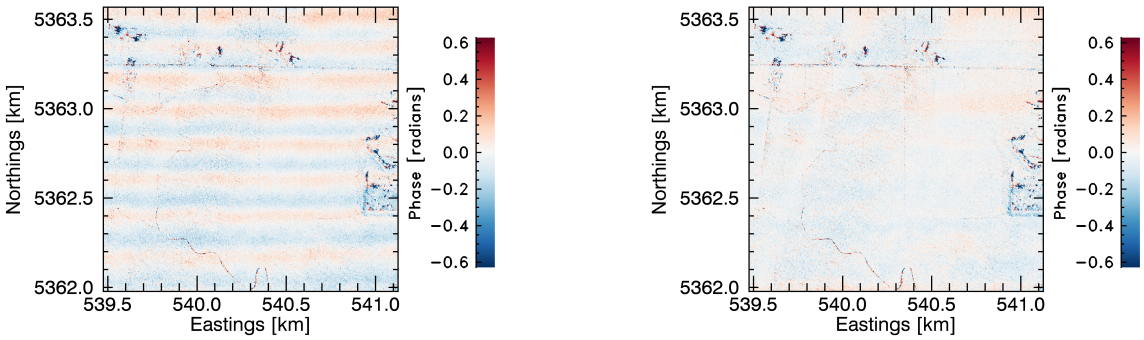

(a) Uncalibrated

(b) Curve fitting

(c) Joint estimate

(d) MLE

Figure 3.6: Interferograms before and after phase calibration with different approaches.

the four images in Figure 3.7. The magnitude of that peak for the uncalibrated is about −27 dB. All three estimation approaches reduced the magnitude of that peak by around 14 dB (Table 3.3). Note that in Table 3.3), we set the peak value for the uncalibrated spectrum to 0 dB and other values in the table are relative to the reference.

With a high-quality laboratory synthesizer used to generate the calibration signal, all three approaches reduced the magnitude of that peak by around 14 dB. Table 3.3 also shows the reduction of phase ripple when we use a crystal oscillator and phase-locked loop in place of signal generator. The approaches using the oscillator reduced the peak in the spectrum by

about 12 dB, which is slightly worse than results of using signal generator. This is reasonable since the precision of the output signal generated from the PLL-based synthesizer will not be as good as the high-precision signal generator.

Table 3.3: Summary of magnitude of the peak in the spectrum before and after phase calibration.

	Signal Generator	Oscillator
Uncalibrated	0 dB	0 dB
Curve Fitting	−14.18 dB	−11.94 dB
Joint Estimate	−14.19 dB	−11.95 dB
MLE	−14.30 dB	−12.07 dB

3.4.4 Estimation with Phase Model 2

The previous parametric estimation schemes performed in this paper exploit Phase Model 1 for estimation. However, the second phase model presented in Section 3.3 is a better description of the phase of the signal. After we calculated the phase ripple with approaches above, we have a rough idea what the phase ripple looks like, so we can create an analytic representation of the phase ripple using a Fourier series. The phase ripple calculated with Phase Model 1 can be represented by Fourier series with the dominant Fourier coefficients,

as is shown below.

$$\begin{aligned}\Phi_r(t) = \frac{a_0}{N} &+ \frac{2a_1}{N}\cos\left(\frac{2\pi}{N}t\right) + \frac{2b_1}{N}\sin\left(\frac{2\pi}{N}t\right) \\ &+ \frac{2a_2}{N}\cos\left(\frac{4\pi}{N}t\right) + \frac{2b_2}{N}\sin\left(\frac{4\pi}{N}t\right) \\ &+ \frac{2a_3}{N}\cos\left(\frac{6\pi}{N}t\right) + \frac{2b_3}{N}\sin\left(\frac{6\pi}{N}t\right) \\ &+ \frac{2a_4}{N}\cos\left(\frac{8\pi}{N}t\right) + \frac{2b_4}{N}\sin\left(\frac{8\pi}{N}t\right) \\ &+ \frac{2a_5}{N}\cos\left(\frac{32\pi}{N}t\right) + \frac{2b_5}{N}\sin\left(\frac{32\pi}{N}t\right) \end{aligned} \tag{3.7}$$

where N is the length of this time series. Then we applied the joint estimation approach described in 3.3 to estimate unknown parameters in Phase Model 2, i.e., a, ω_0, ϕ_0 and ϕ_1 and all the Fourier coefficients in (3.7). With the estimation results, we are able to compute the phase ripple for each channel using (3.7).

The estimated phase ripple with Phase Model 2 are shown in Figure 3.8. As we can observed from Figure 3.8, the ripple estimated with Phase Model 2 shows a low frequency variation behind the fast oscillating phase ripple, which doesn't exist in the ripple estimated with Phase Model 1 in Figure 3.5. The cause for this low frequency variation is likely due to this approach being an ill-conditioned problem. The condition number of the predictor matrix in this case spans 18 orders of magnitude, indicating that the parameter estimates with regression can change significantly in response to small changes in the measured data. Despite this, we find that with joint estimation and Phase Model 2, the phase ripple is reduced by 13 dB.

3.5 Summary

This chapter presents the technique for implementing a calibration scheme for FMCW interferometric SAR. The scheme estimates phase deviations introduced by the radar electronics. The calibration scheme effectively reduces the range-dependent phase ripple observed in the interferograms, and also probably improves the SAR image quality by accounting for a range-dependent phase change. By comparing the results with different estimation schemes, we

find that the estimated phase ripple reproduced by all three approaches are consistent and can reduce the phase ripple by around 14 dB. The performance of calibration with oscillator and PLL to generate the input signal is slightly worse than using the more accurate signal generator but still does an acceptable job. However, we can still observe phase deviations in certain areas of the calibrated interferograms, meaning the calibration for the range-dependent ripple is not perfect or there exist other sources that cause phase errors. These remaining issues need to be addressed in future studies.

We conclude by noting that although the phase calibration scheme presented in this chapter is derived from the dual-channel FMCW radar to reduce the range-dependent phase ripple observed in the interferogram, the proposed approach tried to estimate the phase ripple for each channel. Therefore, it can be adapted to any multi-channel interferometric FMCW radar systems to compensate for the phase nonlinearity in each channel and calibrate the phase for each SAR image. The applications of this approach in interferometric FMCW systems can be promising. Meanwhile, we note that most SAR systems used for geophysical measurements will have a built-in calibration circuit that can most likely generate a single-frequency calibration signal, so the approach taken in this work would be applicable to such systems.

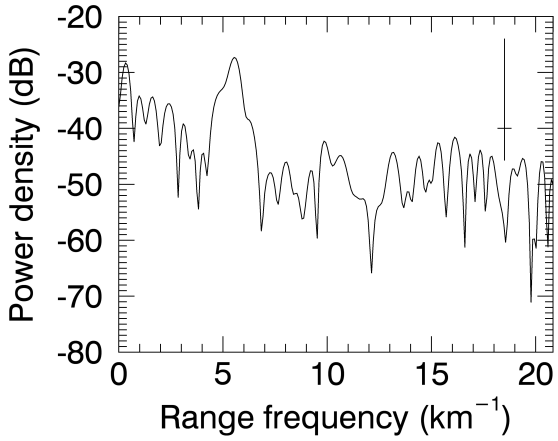

(a) Uncalibrated

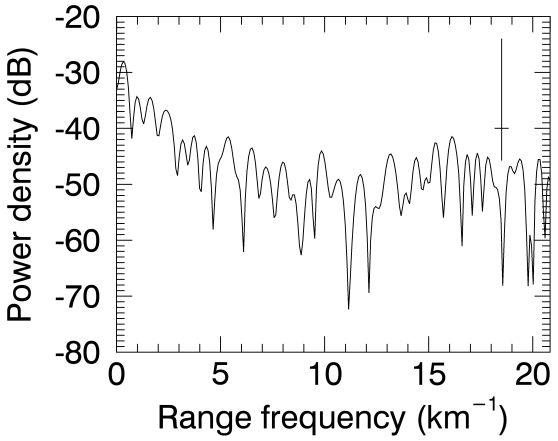

(b) Curve fitting

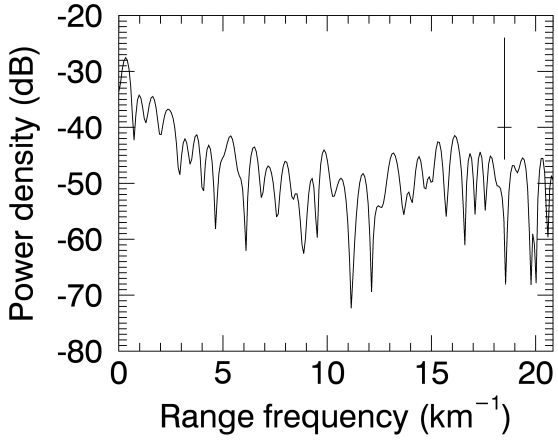

(c) Joint estimate

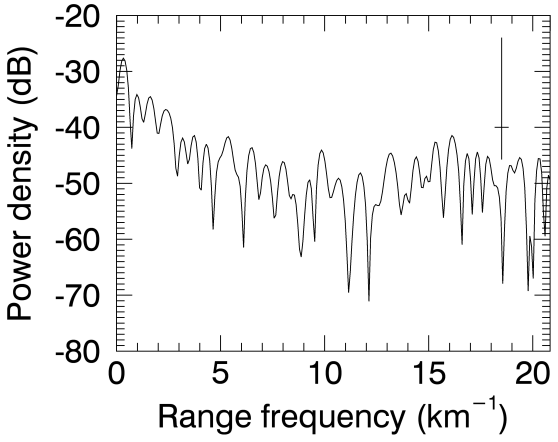

(d) MLE

Figure 3.7: Spectrum of one specific column of interferometric phase. The confidence interval for amplitude and frequency is marked with the horizontal and vertical lines respectively.

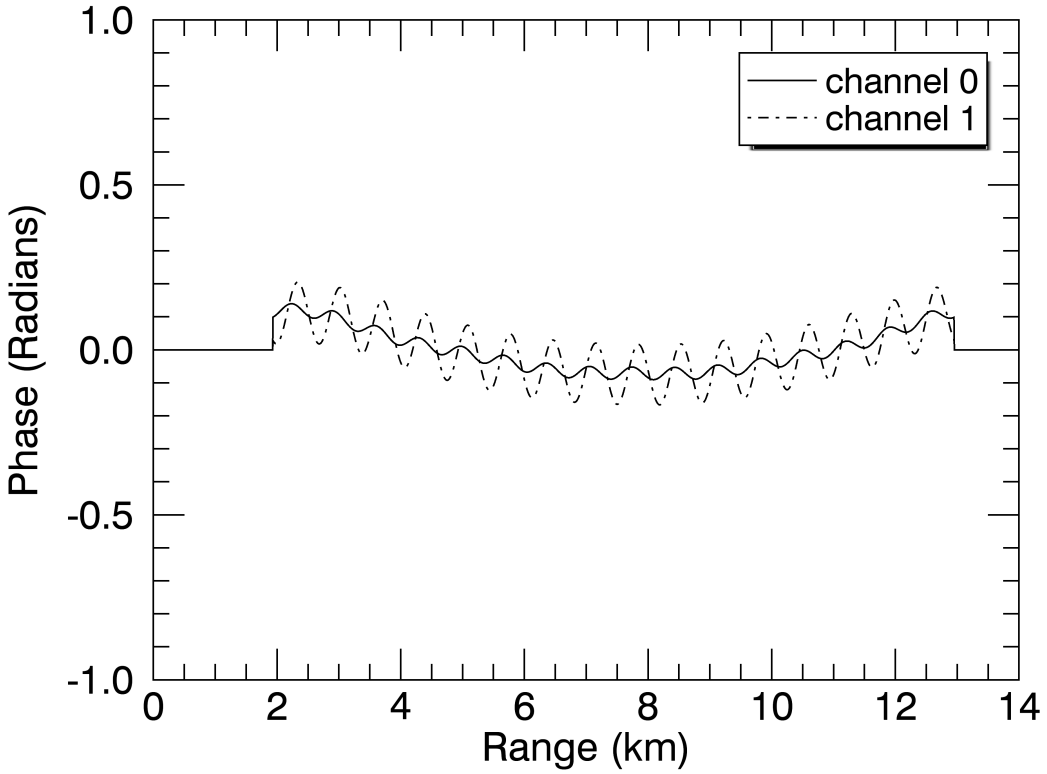

Figure 3.8: Estimated phase ripple for both channels with phase model 2.

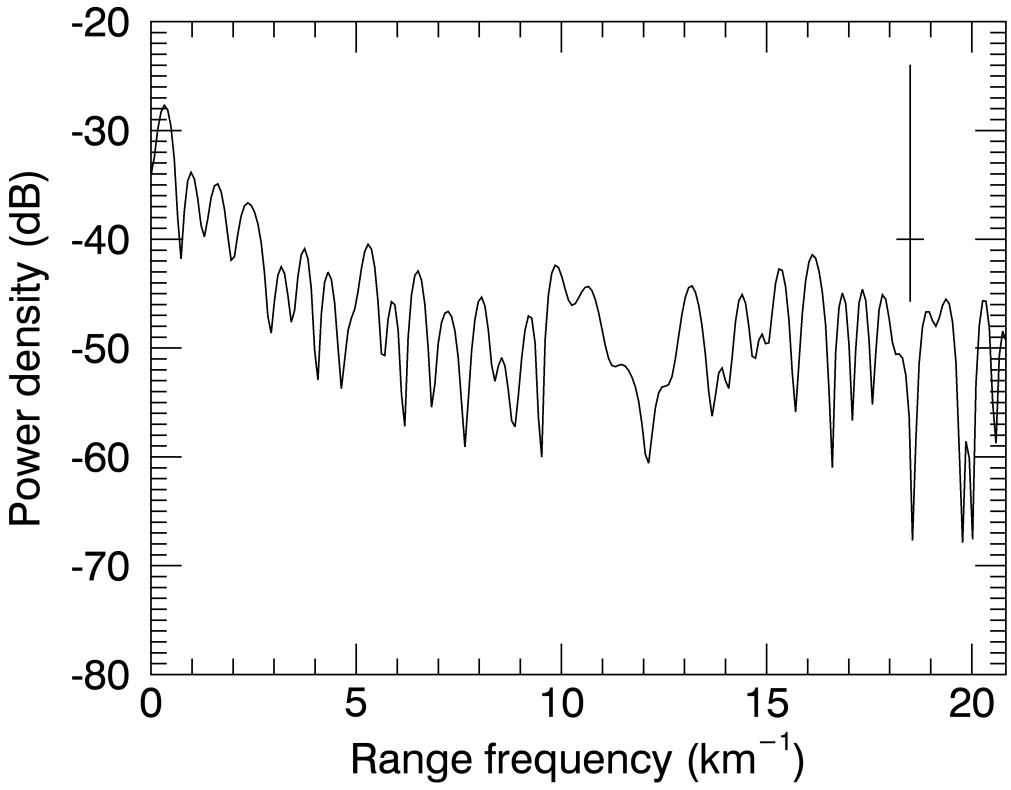

Figure 3.9: Spectrum of one column of interferometric phase with Phase Model 2.

Chapter 4

CALIBRATION OF THE PHASE MISMATCH BETWEEN RECEIVE ANTENNAS

4.1 Observations and Analysis

Chapter 3 introduces the calibration of the phase mismatch between the two receive channels of the FMCW radar. Recall that after the range-dependent phase fluctuations are removed with the proposed approaches, we can still observe some phase variations in the range direction. The slow range-dependent phase variations are illustrated in Figure 4.1, which is the interferogram after the phase ripple calibration using the join estimation approach presented in 3.3.2. Note that during the experiment, the aircraft was flying from the southwest to the northeast and the two squinted SARs are looking at the starboard (right) side of the platform.

It is obvious to see in Figure 4.1 that even after the phase fluctuation calibration, there still exits certain phase offsets (red colored) which may vary slowly in the range direction of the scene. The goal of this chapter is to study what error sources can account for this slowly varying phase offset in range. Since we've already characterized and removed the phase fluctuations due to the imbalance between the radar receive channels, we now consider some other error sources. Note that the system uses C-band patch array antenna as its receive antenna, which consists of a total of 16×4 patches in the antenna plane. Figure 4.2 shows the picture taken for the antennas mounted on the belly of the aircraft. Figure 4.3 shows the structure of the plate antenna. There are 16 patches in the horizontal direction and 4 patches in the vertical direction. These 4 patches in the vertical direction will have their phases constructively or destructively added and cause interference in the elevation plane of the antenna pattern. Therefore, the antenna phase pattern for each receive antenna may be

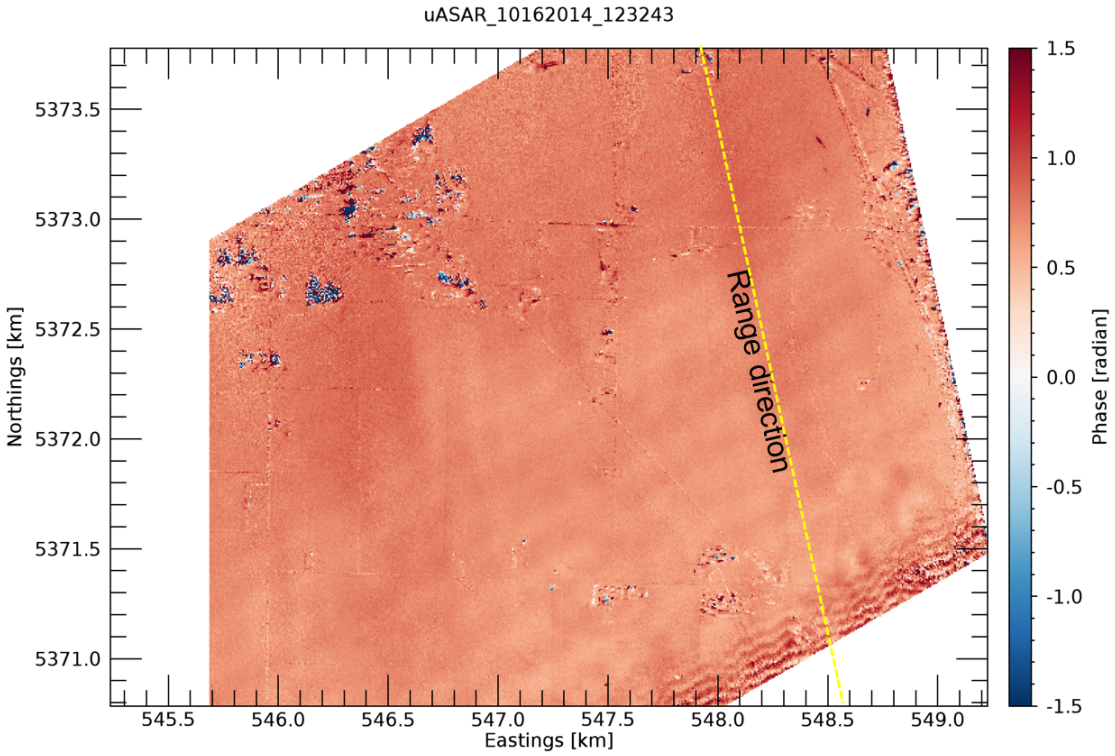

Figure 4.1: Range ripple calibrated (joint estimate) inteferogram for the stationary farmland area in WA, USA

a function of elevation angle in the antenna elevation plane. Also, note that due to the manufacture imperfection, the power for each patch element and spacing between the elements for the two receive antennas can be a bit different. The two receive antennas may have different phase pattern in the elevation plane. The mismatch between the antenna's phase pattern in the elevation plane will result in range-dependent phase offset in the interferometric phase. Note that in the azimuth direction, each pixel is the average of contributions from thousands of pulses. Hence, the phase pattern variations for each pixel in azimuth is cancelled out during averaging and should not be distinct.

Figure 4.2: Picture of C-band patch array antenna mounted on the belly of the aircraft.

4.2 Approaches

Estimating the phase of antenna pattern has become a comparably new topic in interferometric SAR mission. [31] demonstrates for the first time the importance of characterizing the difference between antenna phase patterns in an operational InSAR mission. It also presented a mathematical model for deriving the antenna phase pattern, which can be used for calibration to minimize the residual phase errors between antennas. However, the mathematical derivation has proved to be very complicated and impractical to be implemented for our simation.

To facilitate our approach for the estimation, we defined the antenna offset angle for each pixel located in the antenna beam for the study, which is shown in Figure 4.4. The pixel $\vec{P}$ is first projected onto the $\hat{e}O\hat{k}$ plane and $\vec{P}'$ is the projection point for $\vec{P}$, where $\hat{e}$ is unit vector for E-plane and $\hat{h}$ is the unit vector for H-plane. $\hat{k}$ is in the antenna boresight direction. The angle θ_e between the antenna boresight and the projection of the pixel is what we defined as

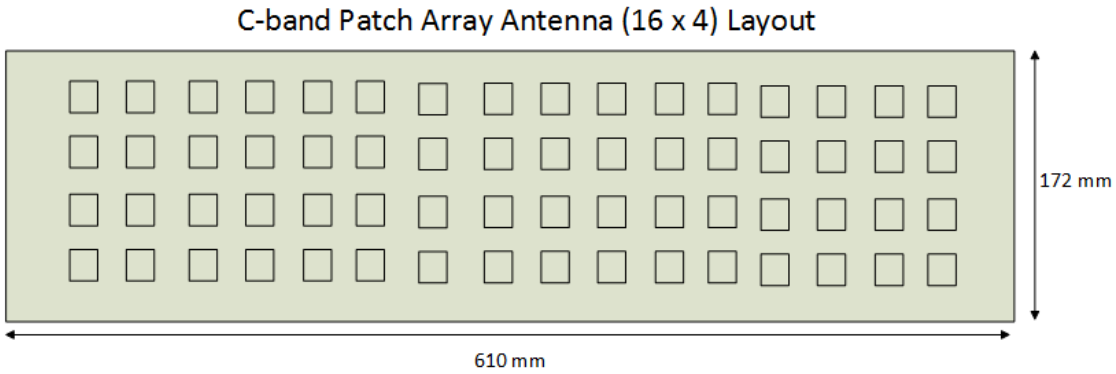

Figure 4.3: Layout of C-band patch array antenna.

the elevation offset angle for the pixel illuminated by the antenna beam.

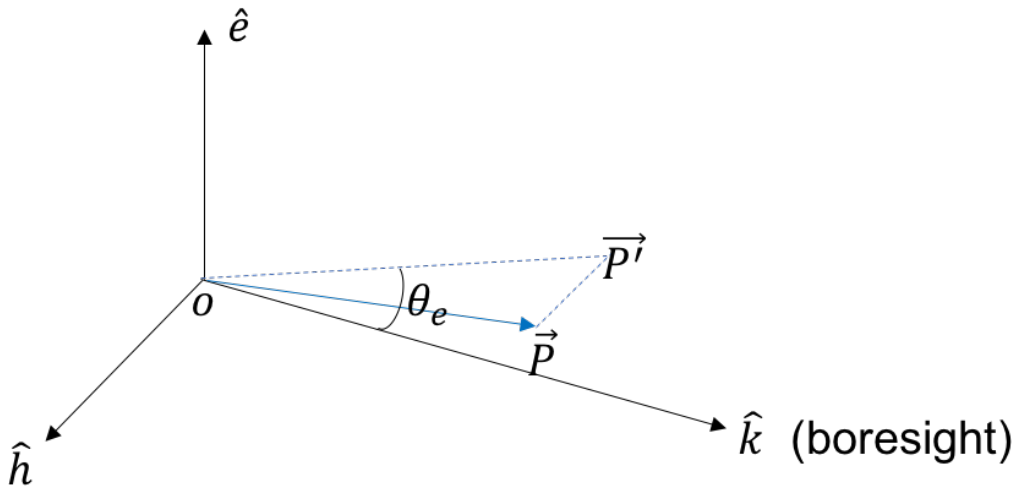

Figure 4.4: Antenna offset angle θ_e for a pixel $\vec{P}$ in the antenna beam defined.

The SAR processor is able to calculate the elevation offset angle for each pixel in the imaged scene based on the measurement of the antenna's position and attitude extracted from the raw data. The values of the elevation offset angle for each pixel in the farmland scene are calculated in the SAR processor The value of the elevation offset angle ranges from

about -46 to 20 degrees for the imaged scene. To estimate the imbalance between the antenna phase pattern, we made use of the measured interferometric phase in Figure 4.1 rather than calculate the antenna phase pattern for each antenna. The estimation approach is fast and efficient. First, we divided the range of elevation offset angles into 184 bins, with the bin size of 0.2 degrees. Then we plot a histogram of the elevation offset angles with 184 bins. For those angles that fall in each bin, we first find out the coordinates for the angles (pixels). Then we go back to the phase plot in Figure 4.1 to find the corresponding phase values at those coordinates. These phase values correspond to the angles that fall into that particular angle bin. We then compute the median of these phase values and use it to represent the phase imbalance between antennas for that particular elevation offset angle (the center value of the bin). In this way, we estimated the phase imbalance for every elevation offset angle in the imaged scene. The histogram of the elevation offset angle is plot in Figure 4.5 and the estimated antenna phase imbalance is shown in Figure 4.6 and Figure 4.7. Note that the 3 dB beamwidth of the antenna is about 30 degrees and we are interested only in elevation offset angles which range from -20 to 15 degrees. The standard deviation of the phases that fall into angle bins in this range is close to 0.1 radians, which is denoted with the red error bar in Figure 4.6. Since the estimated phase imbalance is literally the sample mean of phase values that fall in a particular bin, we are more interested in the standard deviation of the sample mean of the estimated phase imbalance. The error bar in Figure 4.7 indicates the standard deviation of the sample mean. Note for better visualization purpose, here we plot the error bar equal to 10 times big as the standard deviation of the sample mean. The actual standard deviation of sample mean is much smaller and it's not easy to plot it here with good visualization.

We also estimated the antenna phase imbalance from data sets collected at different times to study the consistency of the estimated results. These estimated results are shown in Figure 4.8. Each color plot in this figure represents the estimated antenna phase imbalance from a specific dataset. We can see while the trend of phase pattern stays roughly the same, the mean phase offset of each plot can vary as much as 0.2 radians. To better understand

this, we also need to study what caused the variations in the estimated mean phase offset. A study on the temperature dependence of the mean phase offset is presented in Appendix C

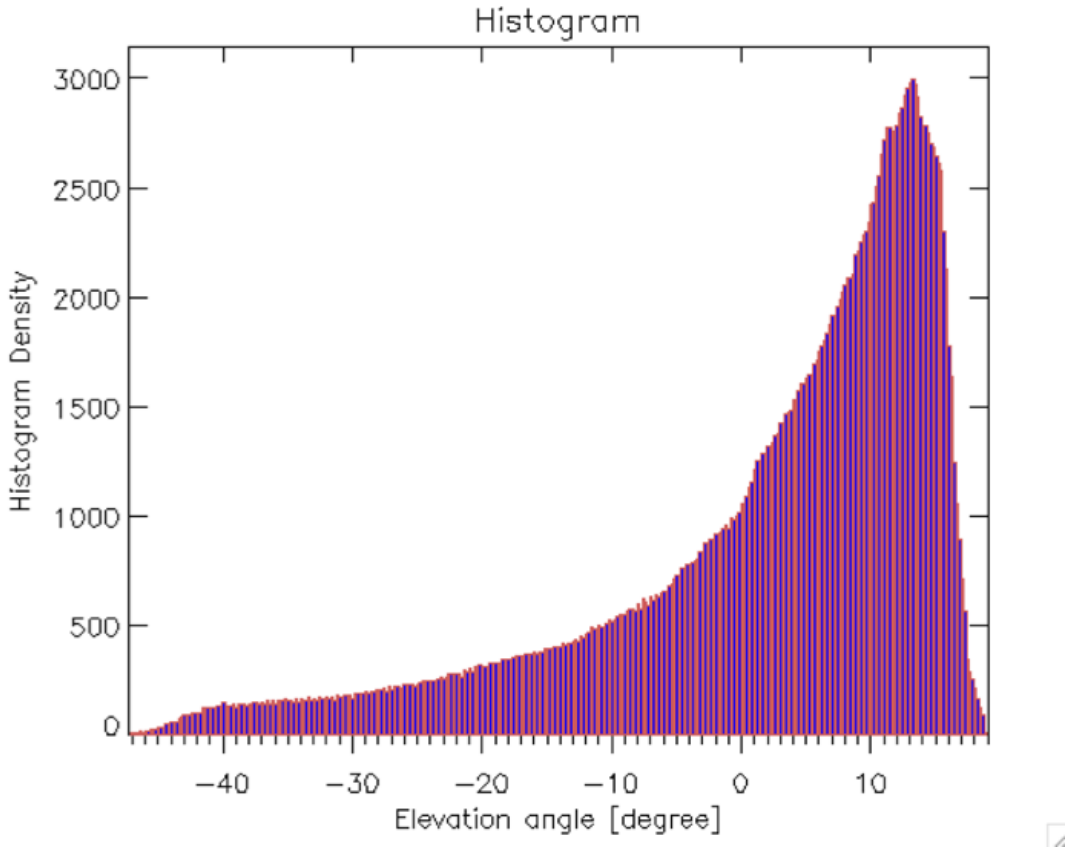

Figure 4.5: Histogram of the antenna phase imbalances vs elevation offset angle.

4.3 Calibrated Results

After we derived the estimated phase imbalances between two receive antennas, we applied it to the post processing of the interferogram. After phase imbalance calibration, the resulting interferogram is shown in Figure 4.9. Compared with the interferogram in Figure 4.1 before calibration, the calibrated interferogram in Figure 4.9 shows a significant reduction of the

phase offset (about 0.6 radians). The phase values are almost zeros for the farmland area after the antenna phase calibration.

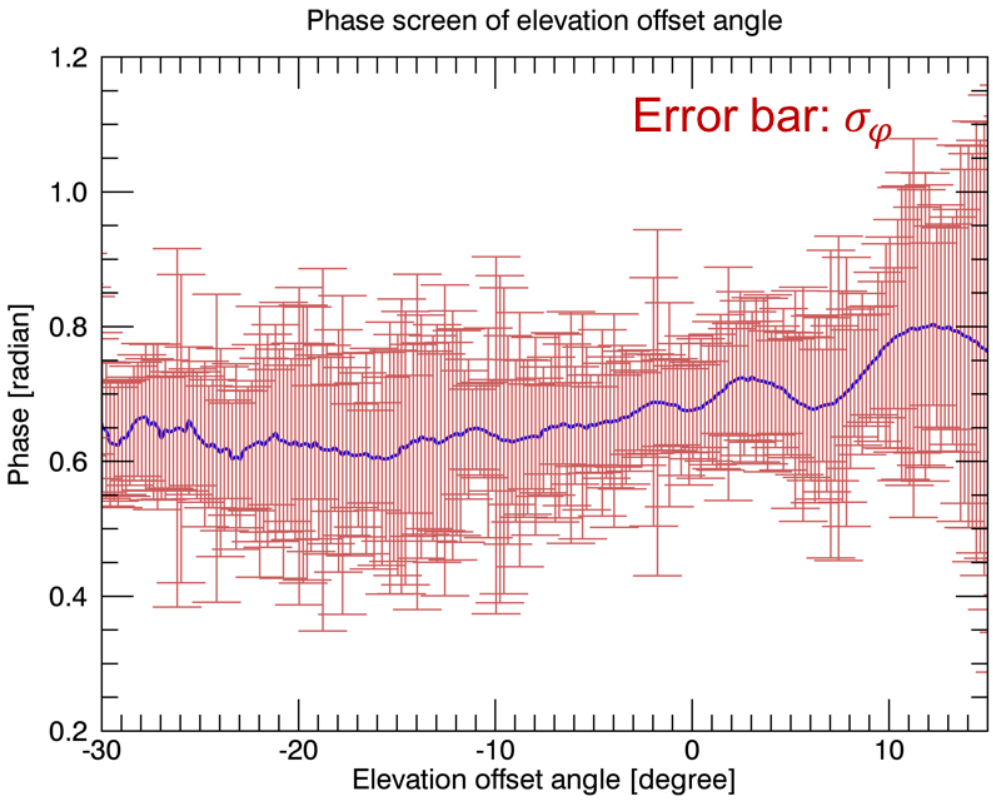

Figure 4.6: Estimated antenna phase imbalance from calibrated interferogram for farmland area in WA, USA . Error bar corresponds to the standard deviation of the phase values in each bin.

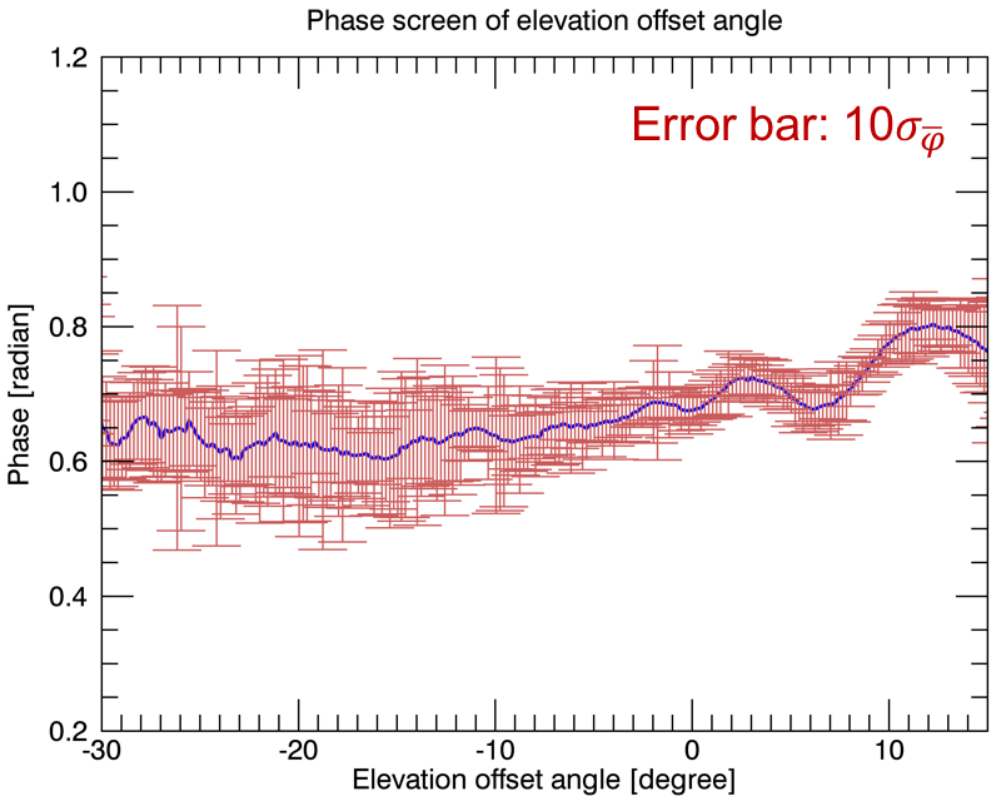

Figure 4.7: Estimated antenna phase imbalance from calibrated interferogram for farmland area in WA, USA . Error bar corresponds to the standard deviation of the sample mean of phase values in each bin.

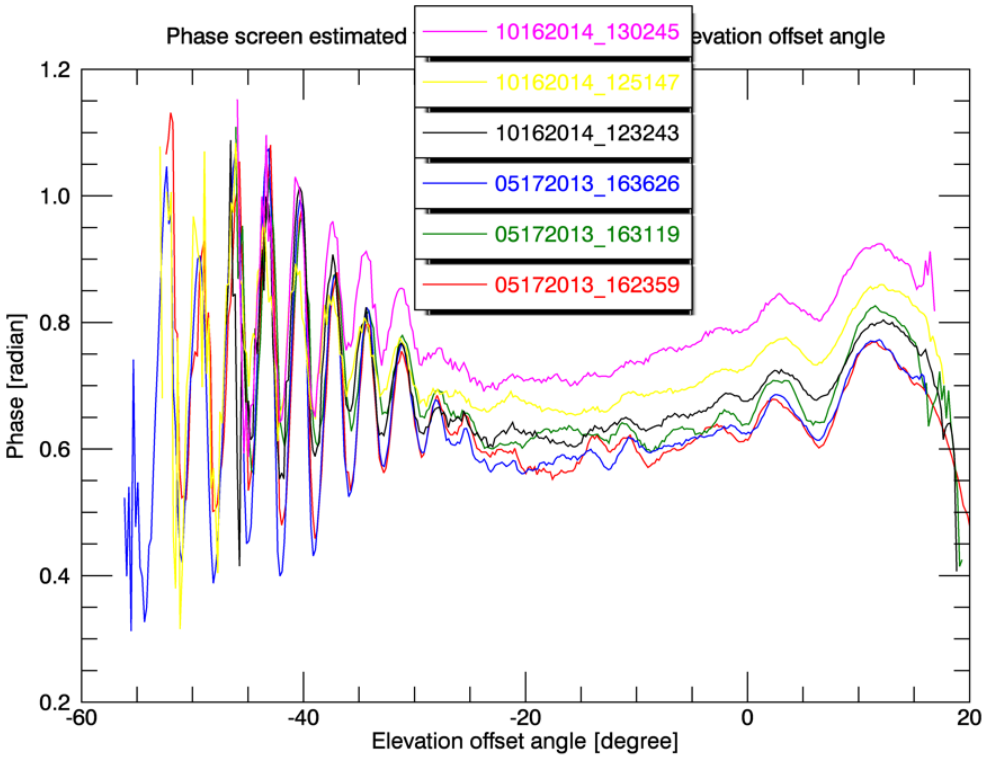

Figure 4.8: Estimated antenna phase imbalance from different data sets to study the consistency of the estimated results.

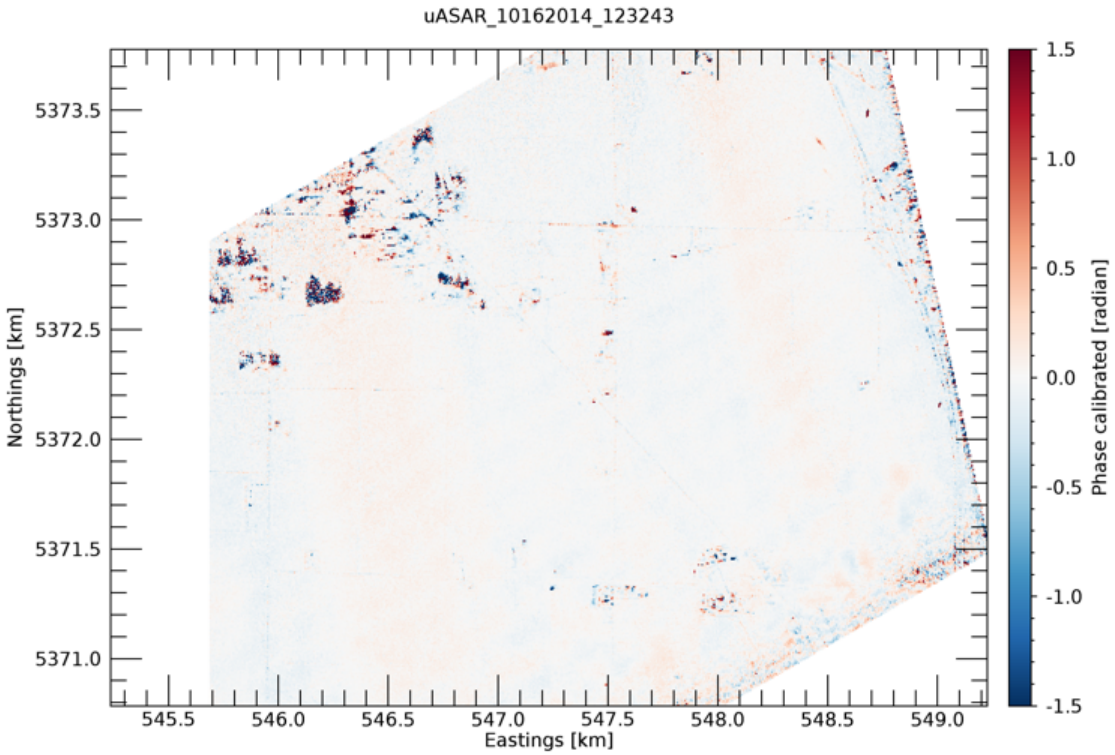

Figure 4.9: Antenna phase imbalance calibrated interferogram for a farmland area in WA, USA .

Chapter 5

ANALYSIS OF EFFECTS OF THE UNCOMPENSATED MOTION ERROR ON ATI PHASE

5.1 Observations and Problem Statement

The systematic phase errors, i.e., phase offsets in ATI phase can be introduced by different sources. Chapter 3 studied the range dependent phase fluctuations due to the phase mismatch between receiver channels. In Chapter 4, we further estimated the phase offsets caused by the mismatch between receive antenna's phase pattern. After we applied the estimated phase ripple and antenna's phase offsets to the ATI processing, we obtained the calibrated interferogram shown in Figure 4.9 of the previous chapter. The phase offsets shown in the figure are pretty close to zeros. However, if we zoom in the image by setting the range of the color bar to be smaller, we are able to observe subtle phase variations in the along-track (cross-range) direction, which is shown in Figure 5.1 as the alternating red and blue regions. Note that Figure 5.1 is the same plot of ATI phase as Figure 4.9 except that the color scales are different. During the experiment, the aircraft was flying from the southwest to the northeast and the two squinted SARs are looking at the starboard (right) side of the platform. These varying phase offset seem to agree well with the significant changes in the mean SAR azimuth pointing angle, which are mainly due to the abrupt changes in the aircraft attitude.

The hypothesis for the cause of these observed azimuthal phase undulations is the uncompensated motion error due to the insufficient INS accuracy. The attitude of the platform during the flight can change due to the air disturbance, and the change of platform attitude or antenna pointing angles might be not perfectly measured by the inertial measurement unit (IMU) and global navigation satellite system (GNSS) installed on the platform. The uncertainty of the antenna attitude or platform velocity will translate into errors in the

ATI phase measurement after the motion compensation in the time-domain backprojection imaging algorithm [58, 59]. These navigation errors are frequently encountered in ATI-SAR systems [14, 16], especially in airborne systems since the abrupt changes in aircraft attitude and speed are more inevitable. Figure 5.2 illustrates the three dimensions in which the attitude of an aircraft changes during a flight: yaw, nose left or right about an axis running up and down; pitch, nose up or down about an axis running from wing to wing; and roll, rotation about an axis running from nose to tail.

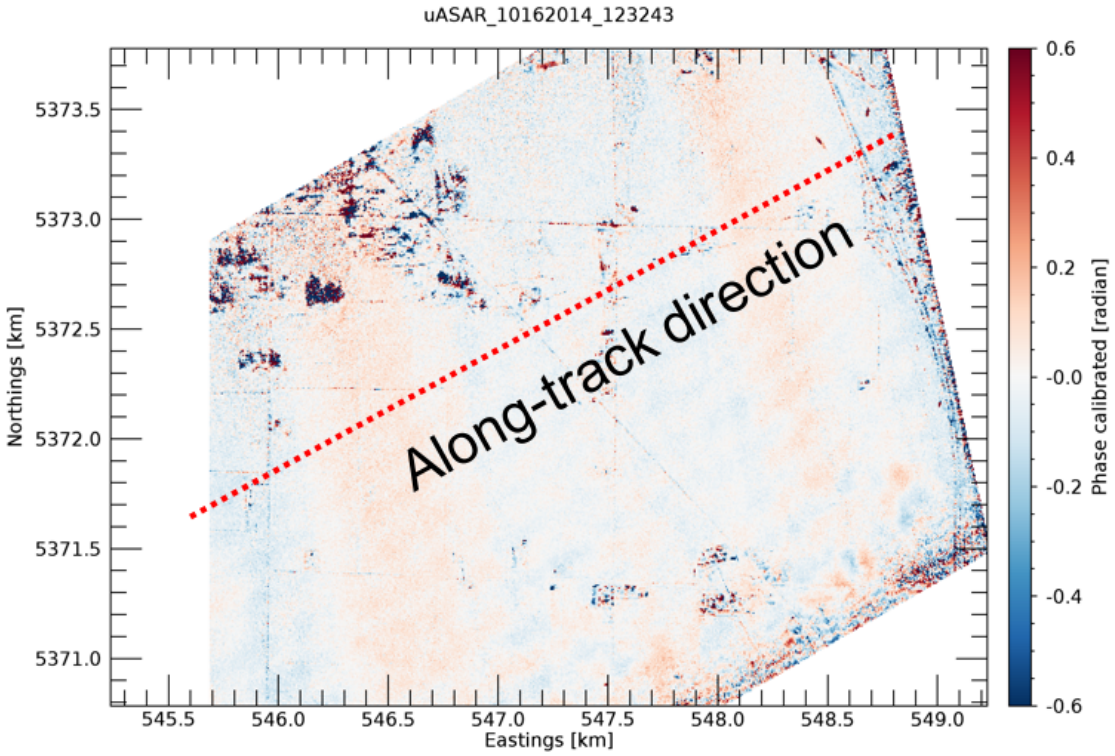

Figure 5.1: Antenna phase imbalance calibrated interferogram for a farmland area in WA, USA .

In this chapter, we investigate the effect of measurement error in platform velocity and attitude on the ATI phase measurement through theoretical analysis and numerical simula-

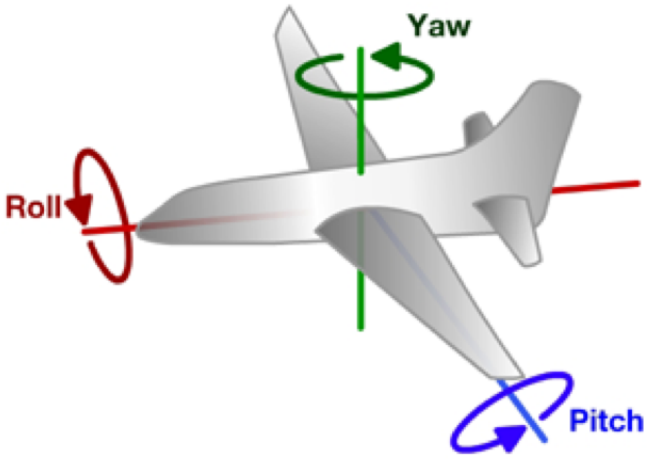

Figure 5.2: Directions of roll, pitch and yaw in an aircraft. Reprinted from [8].

tions. The goal is to verify the observed phase undulations is caused by the uncompensated motion errors by reproducing the observed phase errors with simulations and ultimately, to determine the maximum motion and attitude measurement error that can be tolerated for airborne ATI SAR measurements.

5.2 Theoretical Analysis of Attitude and Velocity Error

Based on previous discussion, the goal of this study is to first find out the effects of the uncompensated attitude and velocity error on the ATI phase since the uncertainties in the aircraft attitude and velocity measurements may introduce phase errors during the motion compensation of the time-domain ATI processing. We start the study with an theoretical derivation of the ATI phase error in terms of platform attitude and velocity errors by using the mathematical approach taken by Frasier and Camps [16]. We first study the sensitivity of the radial velocity measurement to platform velocity and attitude error and then use Equation (2.1) to convert the result to the sensitivity of the ATI phase measurement to velocity and attitude error. The baseline vector in terms of aircraft attitude based on the

measurement geometry shown in Figure 5.3 is

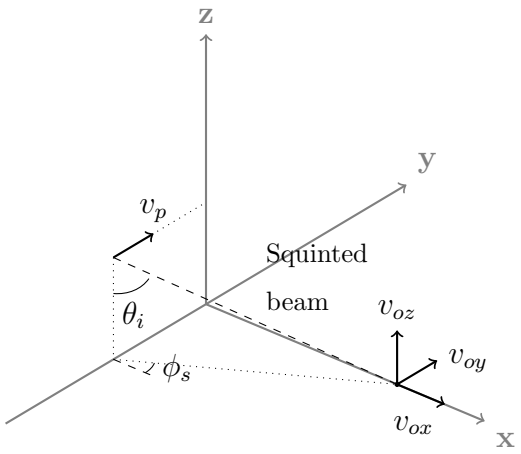

Figure 5.3: Squinted ATI-SAR measurement geometry.

$$\vec{B} = \langle -B\cos\theta\sin\psi, B\cos\theta\cos\psi, B\sin\theta\rangle \tag{5.1}$$

where θ and ψ denote the respective pitch and yaw angles (defined by the NovAtel IMU system) of the baseline. The corresponding unit baseline vector is

$$\hat{B} = \langle -\cos\theta\sin\psi, \cos\theta\cos\psi, \sin\theta\rangle \tag{5.2}$$

The range vector from the end of the along-track baseline to the surface and unit range vector are given by

$$\vec{R} = \langle -R\sin\theta_i\sin\varphi_s, -R\sin\theta_i\cos\varphi_s, R\cos\theta_i\rangle \tag{5.3}$$

$$\hat{R} = \langle -\sin\theta_i\sin\varphi_s, -\sin\theta_i\cos\varphi_s, \cos\theta_i\rangle \tag{5.4}$$

where θ_i is the SAR incidence angle and φ_s is the antenna azimuth angle measured clockwise from north in the compass coordinate system. Therefore, the antenna squint angle ϕ_s in Figure 5.3 will be $90^\circ - \varphi_s$. The platform velocity vector is given by

$$\overrightarrow{v_p} = \langle 0, v_y + \Delta v_y, \Delta v_z\rangle \tag{5.5}$$

where Δv_y and Δv_z are the velocity errors in y and z directions, respectively. The surface point velocity vector is given by

$$\overrightarrow{v_0} = \langle v_{ox}, v_{oy}, v_{oz} \rangle \tag{5.6}$$

The relative vector velocity of the surface point, with respect to the platform velocity is

$$\vec{v} = \overrightarrow{v_p} - \overrightarrow{v_0} \tag{5.7}$$

The interferometric phase of the surface point is given by [16]

$$\Phi = -\frac{2kB}{R}\left(\frac{\vec{R}\cdot\vec{v}}{v_p} - \frac{\vec{R}\cdot\vec{B}}{B}\right) \tag{5.8}$$

Combining (2.1) and (5.7), and replacing the true platform velocity v_p with v_y, we obtain the radial velocity estimate as

$$\begin{aligned} u_r &= -\frac{v_y}{2kB}\frac{2kB}{R}\left(\frac{\vec{R}\cdot\vec{v}}{v_y} - \frac{\vec{R}\cdot\vec{B}}{B}\right) \\ &= -\hat{R}\cdot\vec{v} + (\hat{R}\cdot\hat{B})v_y \end{aligned} \tag{5.9}$$

Substituting (5.2), (5.4) and (5.7) into(5.9), we obtain

$$\begin{aligned} u_r =& (v_y\cos\theta\sin\psi - v_{ox})\sin\theta_i\sin\varphi_s \\ &+ [v_y(1-\cos\theta\cos\psi) + \Delta v_y - v_{oy}]\sin\theta_i\cos\varphi_s \\ &+ (v_y\sin\theta - \Delta v_z + v_{oz})\cos\theta_i \end{aligned} \tag{5.10}$$

Assuming the mean values of θ and ψ are zero, and assuming velocity and attitude errors are independent, the variance of the radial velocity estimate is

$$\begin{aligned} \sigma_{u_r}^2 =& v_y^2\sigma_\psi^2\sin^2\theta_i\sin^2\varphi_s + \sigma_{v_y}^2\sin^2\theta_i\cos^2\varphi_s \\ &+ (v_y^2\sigma_\theta^2 + \sigma_{v_z}^2)\cos^2\theta_i \end{aligned} \tag{5.11}$$

Based on (2.1), the uncertainty of interferometric phase estimate is

$$\begin{aligned} \sigma_\Phi^2 =& \frac{4k^2B^2}{v_y^2}(v_y^2\sigma_\psi^2\sin^2\theta_i\sin^2\varphi_s + \sigma_{v_y}^2\sin^2\theta_i\cos^2\varphi_s \\ &+ (v_y^2\sigma_\theta^2 + \sigma_{v_z}^2)\cos^2\theta_i) \end{aligned} \tag{5.12}$$

Based on the derived relationship between the ATI phase error and the uncertainties in the INS measurements in Equation (5.12), we performed a numerical study of the sensitivity of interferometric phase estimate to the random errors in platform velocity (σ_{v_y}, σ_{v_z}) and attitude (σ_θ, σ_ψ). During the study, one error source is set to be nonzero while the other three error sources are set to be zero. Table 5.1 shows the values of the velocity and attitude errors which correspond to one tenth radians of error in ATI phase estimate. Table 5.2 shows the measurement accuracy for the inertial navigation system (INS). By comparing the data from the two tables, we find that the INS measurement uncertainty (error) for pitch angle (0.014 deg.) or velocities (0.01 m/s) are about 10 times smaller than the corresponding pitch error (0.13 deg.) or velocity error (0.1 m/s) needed to produce 0.1 radian of phase error. While the yaw angle uncertainty (0.026 deg.) of the INS is only 3 times smaller than the yaw error (0.09 radian) needed to produce 0.1 radian phase error in Table 5.1. Therefore, the ATI phase error seems to be most sensitive to the uncertainty in the yaw measurement. We will demonstrate this finding with SAR simulations in the next section.

Table 5.1: Uncertainties in velocity and attitude which corresponds to one tenth radians of error in ATI phase estimate.

σ_Φ	σ_{v_y}	σ_{v_z}	σ_θ	σ_ψ
0.1 radian	0.12 m/s	0.10 m/s	0.13 degree	0.09 degree

Table 5.2: Inertial navigation system (INS) measurement accuracy (RMS).

Roll	Pitch (θ)	Yaw (ψ)	v_y	v_z
0.010 degree	0.014 degree	0.026 degree	0.02 m/s	0.01 m/s

5.3 ATI Simulation

A simulator was developed to simulate ATI-SAR data in the format produced by the radar [60], so that the simulated data could be processed by the same processor that is used for the data collected by the radar. The simulator is a time-domain code that models antenna pattern, pulse shape, and also velocity and attitude changes of the platform on which the radar is mounted.

We used the simulator to reproduce the measurement scenario shown in Figure 5.1 by feeding the simulator with the attitude measurements from the real data. The SAR simulator takes the radar parameters, target parameters and aircraft track information measured by INS as the input. The output, which is the simulated data, is then processed by the SAR processor. The SAR processor used the INS measured attitude and velocity for motion compensation.

To start with, our collaborator Balaban [60] ran the simulator with the attitude and velocity data originally measured by the INS. Note this INS data is considered to be the ground truth in the experiment. We first simulated 11 stationary targets with the true INS data measured during the farmland experiment flight described in Figure 5.1. The output of the simulator is the simulated SAR data with true attitude and velocity data recorded. The baseline experiment here is to process the simulated data with the true INS data, which is shown by the flowchart in Figure 5.4. As we know, the ATI phase for stationary under the such configuration should be zero since we apply time-domain backprojection for imaging and know the exact positions of the antennas and targets.

Then we generated Gaussian errors for pitch, roll and azimuth angles, respectively and the velocities in the INS data and added these errors to the original INS measurement (ground truth). We use these error disturbed INS data to represent the measured attitude and velocity data by the INS with limited instrument accuracy (Level of uncertainty here is:). Note here the Gaussian noise (error) we generated is not white noise due to the fact that during a certain time period, e.g., one second, the aircraft attitude and velocity should

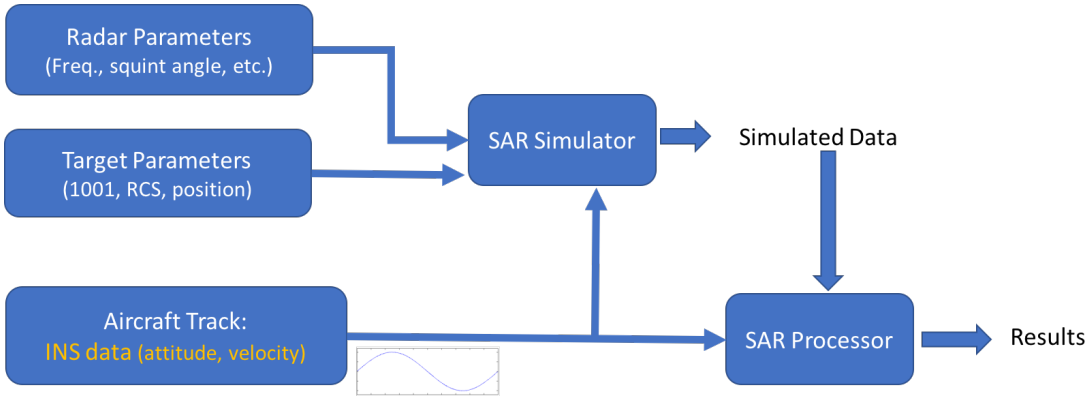

Figure 5.4: Flowchart for simulation experiment. Baseline case.

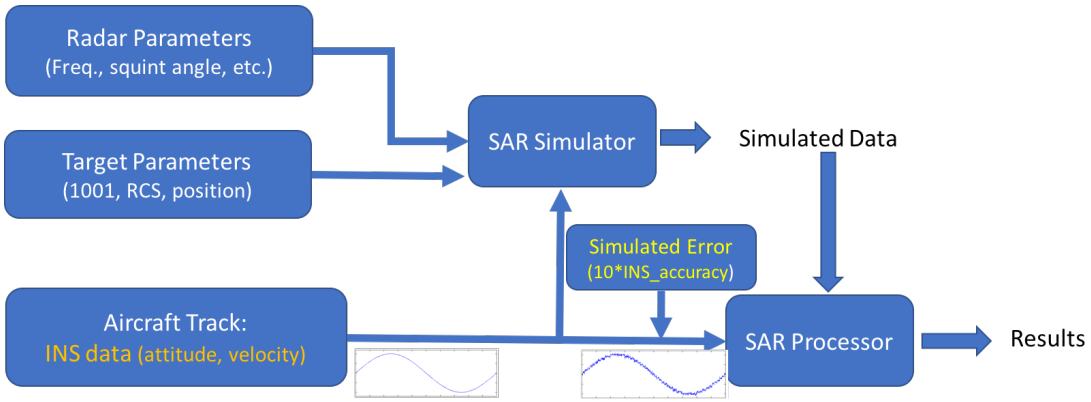

Figure 5.5: Flowchart for simulation experiment. Error disturbed case.

not change abruptly and hence, the Gaussian error remains highly correlated. However, the correlation between each sample error point decreases as time goes by since abrupt attitude changes might occur due to random air disturbance. The generation process for the correlated Gaussian errors is described in Appendix B. Then we processed the simulated data using the error disturbed INS data to study the effects of the attitude and velocity errors separately on the ATI phase, which is shown by the flowchart in Figure 5.5.

The procedure to study the effect of velocity errors on ATI phase is very similar. We first added correlated Gaussian noises to the INS velocity measurement.Then we repeated

the procedure to create simulated SAR data and processed them in the SAR processor with the error disturbed INS measurements.

5.4 Results and Discussion

Based on the simulation configuration specified in previous section, we simulated the SAR data and then processed the simulated data in the SAR processor. To begin with, we simulated 11 stationary point targets to study the effects of attitude and velocity errors on ATI phase by comparing the error disturbed cases to the baseline experiment. Figure 5.6 shows the interferogram generated for the baseline experiment where we simulated the SAR data with original INS measurement and processed it with the same INS data. Note that during the simulation, we set the DEM of the targets to be zero to eliminate the effects of the DEM uncertainty, which will be studied in Chapter 6. We can clearly see the targets feature as bright white dots denoting zero phases. Next, we generated the interferograms by processing the simulated data with attitude error and velocity error adding to original INS data.

We plot the phase values for the 11 targets for error disturbed cases as well as the reference case in Figure 5.7. The black line denotes the phase values for the reference case where the data is processed with the original INS data. The RMS values of the phases for the 11 targets is close to zero (0.028 radian). After attitude errors are added to the original INS data, the phases (red color with RMS value of 0.047 radian) vary quite a bit from the original ones. We are more interested in which attitude (roll, pitch or yaw) uncertainty contributes most to the phase change. The RMS value of phases for the INS data with velocity errors (in blue) is close to the RMS value of the original phases, which indicates that the velocity error probably do not contribute as much as the attitude error does to the interferometric phase.

We further studied which attitude error has the most significant impact on the ATI phase by adding the roll error, pitch error, and azimuth (equivalent to change of yaw) error to the INS attitude data respectively and used the disturbed INS data to process the simulated data. To get more accurate phase statistics, this time we simulated 1001 stationary targets

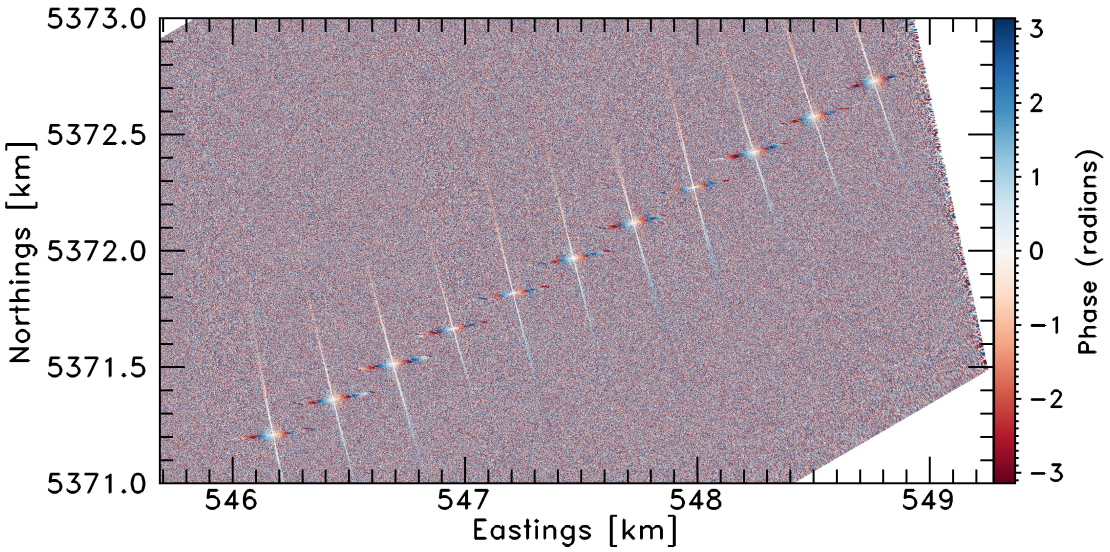

Figure 5.6: Interferogram for simulated 11 stationary point targets spread in the along-track direction.

along the flight direction with the assistance of our collaborate Balaban [60]. Figure 5.8 shows the interferogram of the 1001 simulated targets for the reference case. The targets' phases within the red dashed tile are very close to zero (white color). Note here we used the same geographic information for simulations as the described farmland experiment except that the DEM height for all the targets are set to zero.

Then we plot the phases for the targets for each individual simulated case. The roll error, pitch error and azimuth error cases, together with the reference case are plotted in Figure 5.9. Subfigure 5.9a corresponds to the reference case where no error was added to the INS data for processing, and the RMS value of the target phase for this case is 0.037 radian, which is very close to zero. This nonzero phase is caused by the finite SNR (0 dB) during the simulation. The remaining 3 subfigures correspond to the cases where only the roll/pitch/yaw error was added to INS data for the processing. By comparing the 3 error disturbed cases, we find that the roll error has minor effect on the ATI phase error and the pitch error has a little

impact on the ATI phase error but not significant. The RMS phase for the case where yaw error was added is 0.21 radian, which further verifies our theoretical analysis that the ATI phase error is very sensitive to the uncertainty in the yaw angle measurement.

After comparing the RMS phase error for each individual error disturbed case with the reference case, we then combined attitude errors and added roll, pitch and yaw errors together into the INS data and repeat the simulation. Meanwhile, we added velocity errors in horizontal direction (east and north) and vertical direction (up) together to the INS data to repeat simulation. The phase plots for the combined attitude error and combined velocity error cases are shown in Figure 5.10. Subfigure 5.10a shows the RMS value for the case with combined attitude errors is 0.25 radian, which is much higher than the RMS phase error (0.038 radian) for case with combined velocity errors. This agrees with the conclusion of the theoretical analysis and the results from simulations for 11 targets in Figure 5.7.

Finally, we added both the combined attitude and velocity errors into the INS data for the SAR processor and plot the phase for the 1001 targets and the phase from the actual farmland interferogram in Figure 5.11. We compared the phase statistics of the simulated targets' phases in Figure 5.10 with the actual phase values in the actual farmland interferogram in Figure 5.1. The RMS phase values for the simulated targets with both attitude and velocity errors adding to INS is about 0.25 radian, while the RMS phase value for the corresponding pixels from the actual farmland interferogram is 0.27 radian. Therefore, the simulated phase with attitude and velocity error added to INS data does capture most of the azimuthal phase variation in the farmland interferogram. This further demonstrates our hypothesis that the uncertainty in the INS measurement account for most of the phase undulations observed in the along-track direction.

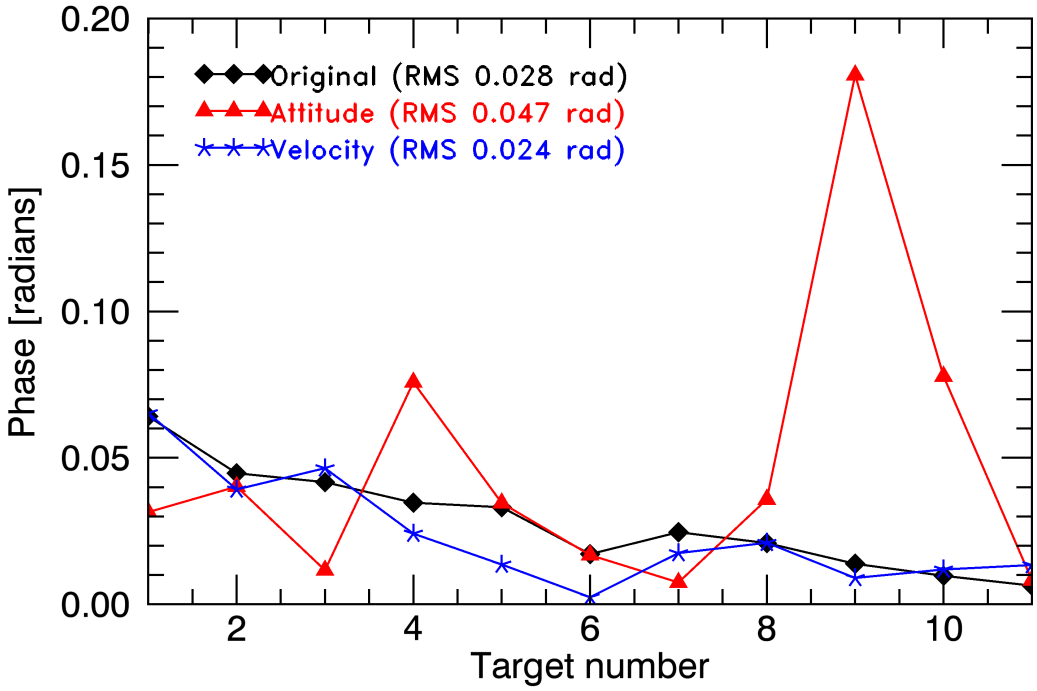

Figure 5.7: Phase plot for the 11 simulated stationary targets. Black color denotes the phase for the baseline case where original INS data was used to process the simulated data. Red color represents the case where attitude (roll, pitch, azimuth) errors were added to the original INS data for SAR processor. Blue color represents the case where velocity (horizontal and vertical) errors were added to the original INS data.

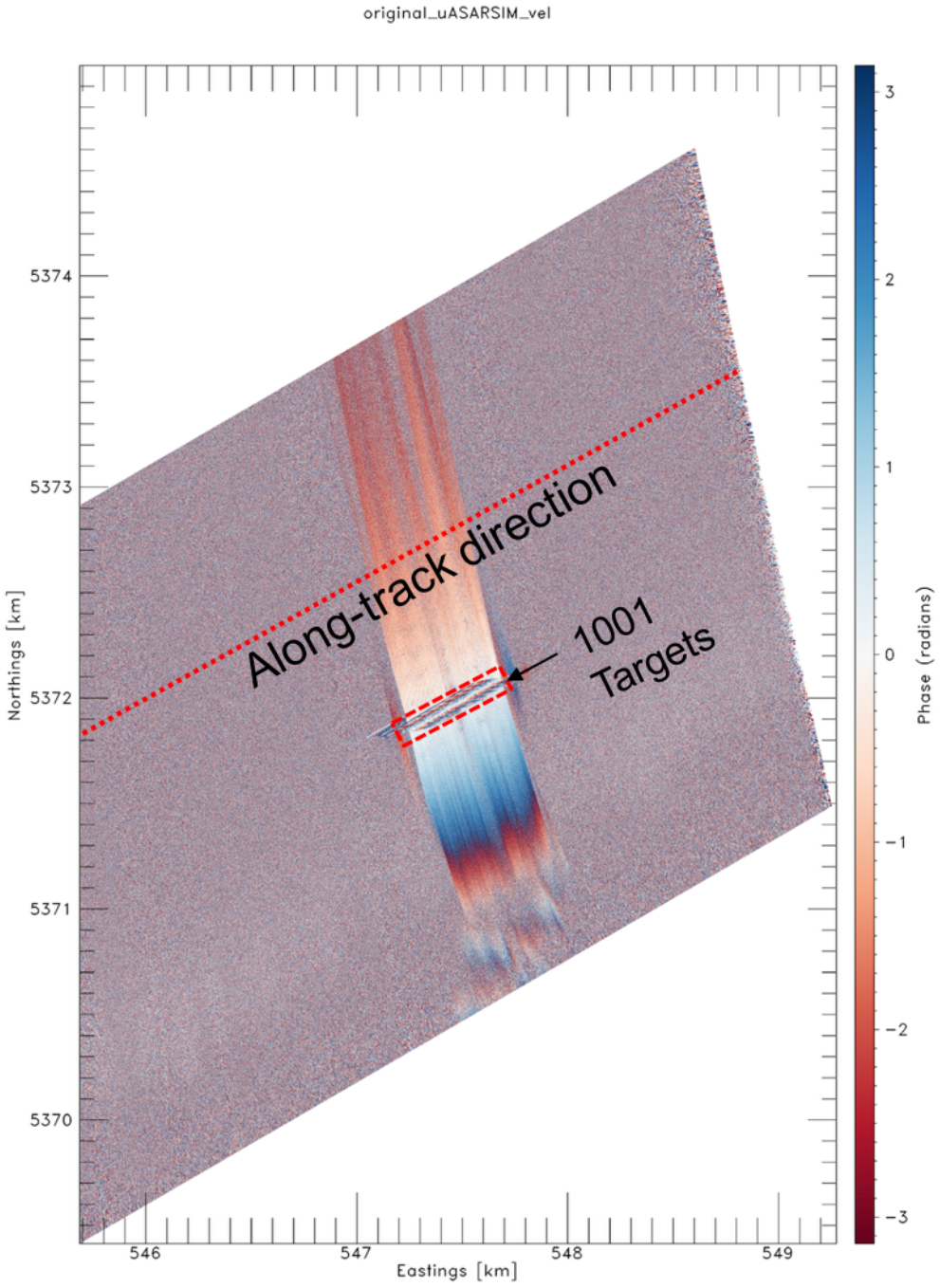

Figure 5.8: Interferogram for simulated 1001 stationary point targets spread in the along-track direction.

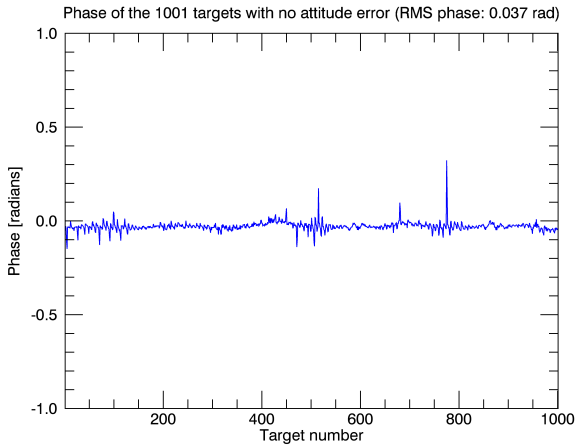

(a) No error

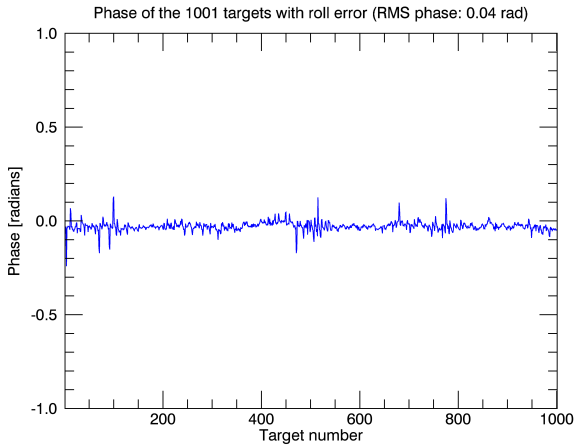

(b) Roll error

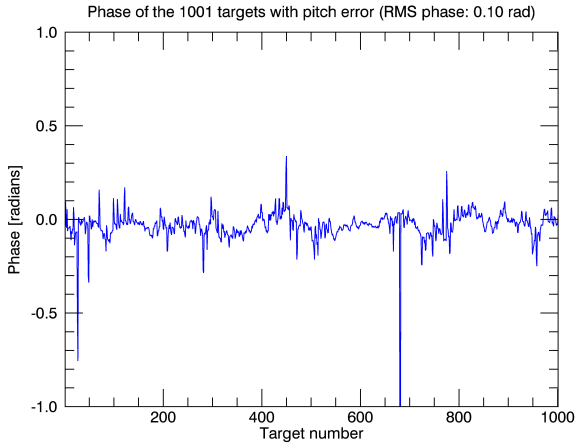

(c) Pitch error

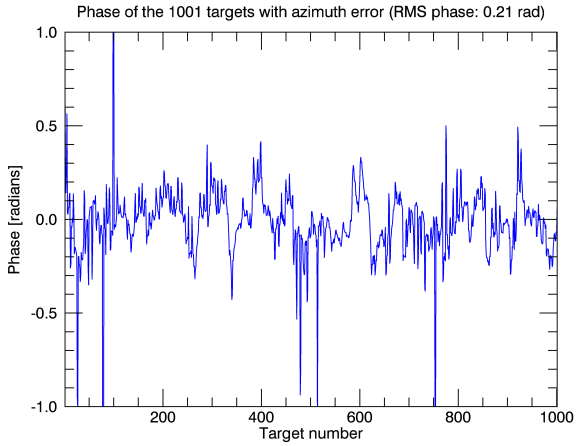

(d) Yaw error

Figure 5.9: Phase plots for the 1001 stationary targets under with different simulated cases.

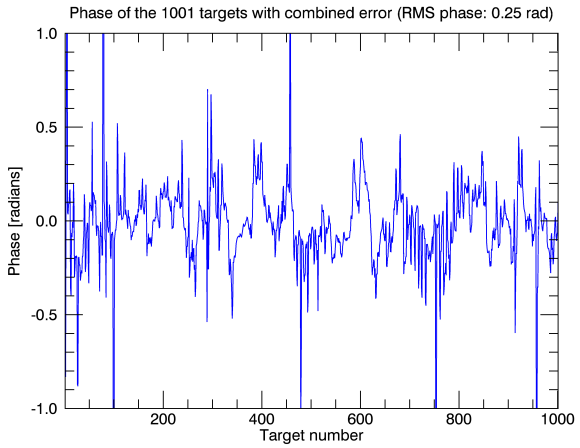

(a) Combined attitude error

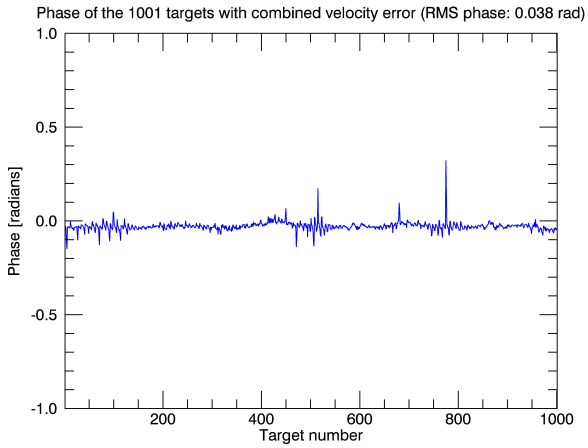

(b) Combined velocity error

Figure 5.10: Phase plots for the 1001 stationary simulated targets with combined attitude and velocity errors added.

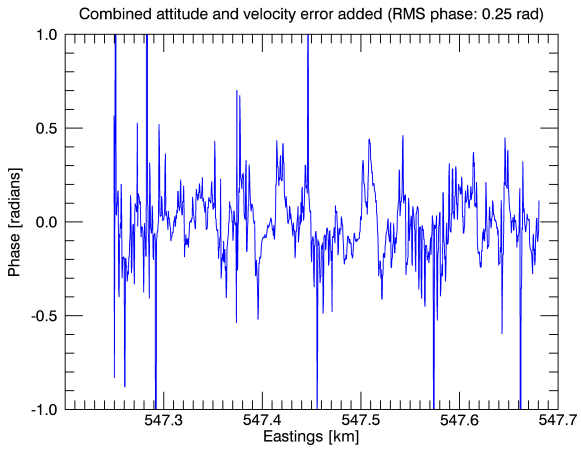

(a) Combined attitude and velocity error

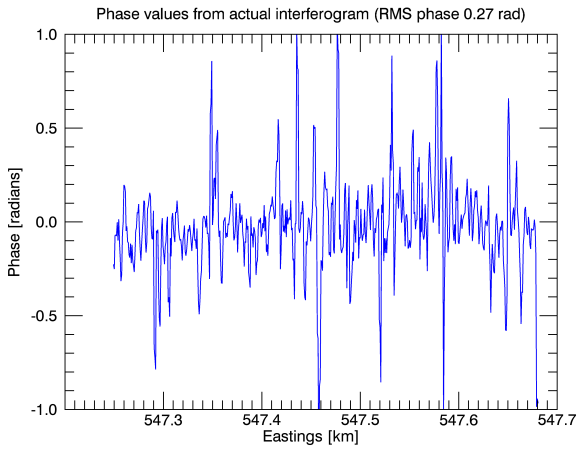

(b) Actual interferogram

Figure 5.11: Phase plots for simulated targets with INS error and actual farmland interferogram.

Chapter 6

ANALYSIS OF EFFECTS OF THE DEM ERROR ON ATI PHASE

6.1 Problem Statement

During the time-domain backprojection image formation in the SAR processing, we need accurate information on both the antenna's position and scatter's height. The antenna's position is calculated from the INS measurement on aircraft attitude and velocity. The target's height is provided by a reference digital elevation model (DEM). The Digital Elevation Model (DEM) used by the SAR processor was obtained from the Shuttle Radar Topography Mission (SRTM). The DEM map product produced by SRTM has a spatial resolution of one arc-second, or about 30 meters. The vertical height accuracy of the DEM is about 12 meters and the horizontal circular accuracy is less than 20 meters, which might introduce the ATI phase error during the SAR processing. In this chapter, we performed a numerical analysis to study the effect of the DEM vertical uncertainty on the ATI phase measurement and demonstrated that this amount of uncertainty in DEM would not have a significant impact on the ATI phase measurement.

6.2 Mathematical Analysis

As is illustrated in Figure 6.1, in the 3-dimensional standard Cartesian coordinate system, the radar antenna is at position $\vec{A} = (0, 0, H)$, where H denotes the antenna altitude.

The scatterer's true position is at $\vec{P} = (x, y, 0)$. Due to the limited accuracy of the DEM, the processor will think the scatterer at position $\vec{D} = (x, y, h)$, indicating that the target altitude is h. Recall that the expression of the interferometric phase of the surface point in Equation (5.8) is related to $\vec{R}$, which is the range vector between the antenna and the surface

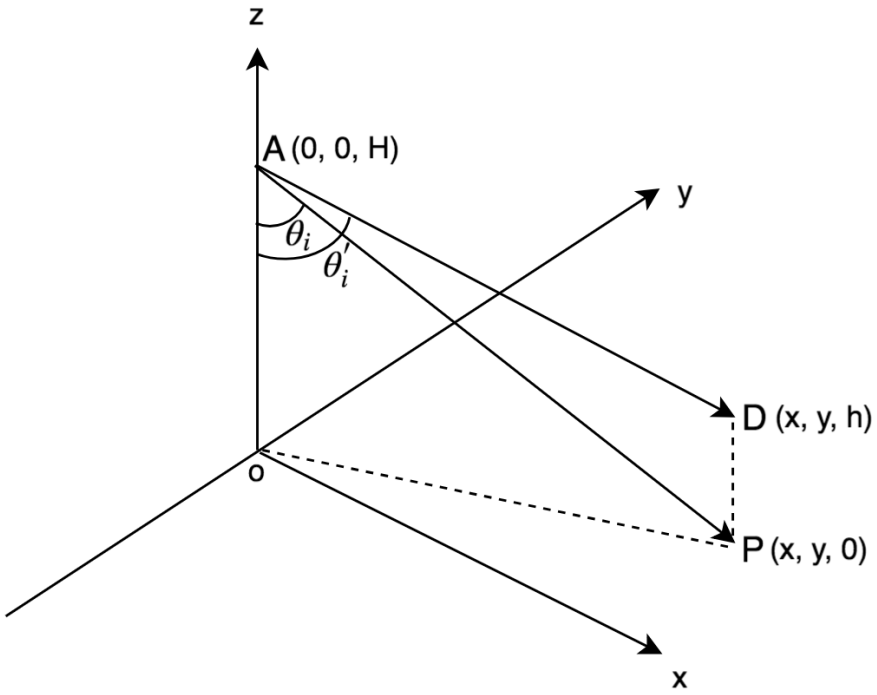

Figure 6.1: Illustration of the imaging geometry for inaccurate DEM.

point. Therefore, the ATI phase error introduced by the DEM error is the interferometric phase difference between the range path $\overrightarrow{R_{AD}}$ and $\overrightarrow{R_{AP}}$. Note that our derivation assumes that the aircraft is flying in the y direction, which is the UTM North and x axis is pointing to UTM East. Let $\vec{R} = \overrightarrow{R_{AP}}$, $\vec{R}' = \overrightarrow{R_{AD}}$, and replace the true platform velocity v_p with v_y y, we calculate the ATI phase error

$$\begin{aligned}\Delta\Phi &= \Phi_{AD} - \Phi_{AP} \\ &= -\frac{2kB}{R'}\left(\frac{\vec{R}' \cdot \vec{v}}{v_y} - \frac{\vec{R}' \cdot \vec{B}}{B}\right) + \frac{2kB}{R}\left(\frac{\vec{R} \cdot \vec{v}}{v_y} - \frac{\vec{R} \cdot \vec{B}}{B}\right) \\ &= 2kB\left[\frac{(\hat{R} - \hat{R}') \cdot \vec{v}}{v_y} - (\hat{R} - \hat{R}') \cdot \hat{B}\right] \end{aligned} \tag{6.1}$$

where $\hat{B}$ is the unit baseline vector in Euqation (5.2) given by and B is the length of the

baseline. $\hat{R}$ is the unit range vector for $\vec{R}$,

$$\hat{R} = \langle -\sin\theta_i \cos\phi_s,\ -\sin\theta_i \cos\phi_s,\ \cos\theta_i \rangle \tag{6.2}$$

where θ_i is the antenna incidence angle and ϕ_s is the antenna squint angle. $\hat{R}'$ is the corresponding unit range vector for $\vec{R}'$ with a different incidence angle θ_i. $\vec{v}$ is the relative vector velocity of the surface point, with respect to the platform velocity given by Equation (5.5) (5.6), (5.7).

The difference between the two unit range vectors is

$$\hat{R} - \hat{R}' = \langle -(\sin\theta_i - \sin\theta_i')\cos\phi_s,\ -(\sin\theta_i - \sin\theta_i')\cos\phi_s,\ \cos\theta_i \rangle \tag{6.3}$$

where θ is the incidence angle. Based on the geometry shown in Figure 6.1, we have the following relationship

$$\sin\theta_i - \sin\theta_i' = \sin\theta_i - \frac{H\tan\theta_i}{\sqrt{(H\tan\theta_i)^2 + (H-h)^2}} \tag{6.4}$$

$$\cos\theta_i - \cos\theta_i' = \cos\theta_i - \frac{H-h}{\sqrt{(H\tan\theta_i)^2 + (H-h)^2}} \tag{6.5}$$

Substituting Equation (6.3) (6.4) (6.5) into Equation (6.1), we can express the ATI phase error in terms of θ_i, H and h

$$\begin{aligned}\Delta\Phi = 2kB\Bigg[&\left(\frac{v_{ox}}{v_y} - \cos\theta\sin\psi\right)\cos\phi_s \left(\sin\theta_i - \frac{H\tan\theta_i}{\sqrt{(H\tan\theta_i)^2 + (H-h)^2}}\right) \\ &+ \left(\cos\theta\cos\psi - 1 - \frac{\Delta v_y}{v_y} + \frac{v_{oy}}{v_y}\right)\sin\phi_s \left(\sin\theta_i - \frac{H\tan\theta_i}{\sqrt{(H\tan\theta_i)^2 + (H-h)^2}}\right) \\ &+ \left(\frac{\Delta v_z}{v_y} - \frac{v_{oz}}{v_y} - \sin\theta\right)\left(\cos\theta_i - \frac{H-h}{\sqrt{(H\tan\theta_i)^2 + (H-h)^2}}\right)\Bigg]\end{aligned} \tag{6.6}$$

where θ and ψ denote the respective pitch and yaw angles of the baseline, θ_i is the SAR incidence angle, ϕ_s is the antenna squint angle shown in Figure 5.3. Δv_y and Δv_z are the

INS velocity errors in y and z directions, respectively. v_{ox}, v_{oy}, v_{oz} are the scatterer's velocity components in x, y, z directions, respectively.

Note that Equation (6.6) is the exact format of the derived ATI phase error in terms of the DEM uncertainty h. Here we can further simply this equation to obtain a better understanding of the effect of the ratio of DEM height error h to the aircraft altitude H. For the term in Equation (6.6) which contains h, we performed Taylor expansion at zero and used the first two terms from the expansion for approximation

$$\begin{aligned}
\frac{H\tan\theta_i}{\sqrt{(H\tan\theta_i)^2+(H-h)^2}} &= \frac{\tan\theta_i}{\sqrt{\tan^2\theta_i+(1-\frac{h}{H})^2}} \\
&\approx \frac{\tan\theta_i}{\sqrt{\tan^2\theta_i+(1-\frac{2h}{H})}} \\
&= \frac{\tan\theta_i}{\sqrt{\sec^2\theta_i-\frac{2h}{H}}} \\
&= \frac{\sin\theta_i}{\sqrt{1-\frac{2h}{H}\cos^2\theta_i}} \\
&\approx \sin\theta_i(1+\frac{h}{H}\cos^2\theta_i) \qquad (6.7)
\end{aligned}$$

where we ignored the 2nd order terms $(\frac{h}{H})^2$ during the 1st approximation and performed the Taylor expansion at zero for $\frac{1}{\sqrt{1-\frac{2h}{H}\cos^2\theta_i}}$ by ignoring the higher order terms during the 2nd approximation. Note that this is reasonable since h is on the order of 10 m while H is on the order of 1000 m, the ratio $\frac{h}{H}$ is close to zero. Similarly, we have

$$\begin{aligned}
\frac{H-h}{\sqrt{(H\tan\theta_i)^2+(H-h)^2}} &= \frac{1}{\sqrt{(\frac{H\tan\theta_i}{H-h})^2+1}} \\
&= \frac{1}{\sqrt{(1+\frac{h}{H-h})^2\tan^2\theta_i+1}} \\
&\approx \frac{1}{\sqrt{(1+\frac{2h}{H-h})\tan^2\theta_i+1}} \\
&= \frac{1}{\sqrt{(\sec^2\theta_i+\frac{2h\tan^2\theta_i}{H-h})}} \\
&= \frac{\cos\theta_i}{\sqrt{(1+\frac{2h\sin^2\theta_i}{H-h})}} \\
&\approx \cos\theta_i(1-\frac{h\sin^2\theta_i}{H-h}) \qquad (6.8)
\end{aligned}$$

Note that during the second approximation above we performed the Taylor expansion at zero for $\frac{1}{\sqrt{(1+\frac{2h\sin^2\theta_i}{H-h})}}$ and ignored the high order terms. We also noticed that with Taylor expansion, the term $\frac{h}{H-h}$ after the second approximation can be further approximated by

$$\begin{aligned}
\frac{h}{H-h} &= \frac{\frac{h}{H}}{1-\frac{h}{H}} \\
&\approx \frac{h}{H}(1+\frac{h}{H}) \\
&\approx \frac{h}{H} \qquad (6.9)
\end{aligned}$$

where we performed Taylor expansion for $\frac{1}{1-\frac{h}{H}}$ at zero and ignored the high order terms during the first approximation and ignored the $(\frac{h}{H})^2$ term during the second approximation. Finally, we substitute all the above approximations into Equation (6.6) and express the ATI

phase error in terms of the DEM error to altitude ratio with

$$\begin{aligned}\Delta\Phi = 2kB\frac{h}{H}\Bigg[&- \left(\frac{v_{ox}}{v_y} - \cos\theta\sin\psi\right)\cos\phi_s\sin\theta_i\cos^2\theta_i \\ &- \left(\cos\theta\cos\psi - 1 - \frac{\Delta v_y}{v_y} + \frac{v_{oy}}{v_y}\right)\sin\phi_s\sin\theta_i\cos^2\theta_i \\ &+ \left(\frac{\Delta v_z}{v_y} - \frac{v_{oz}}{v_y} - \sin\theta\right)\sin^2\theta_i\cos\theta_i\Bigg] \end{aligned} \tag{6.10}$$

With the Equation (6.10), it's easy to tell that the ATI phase error is approximately linearly proportional to the DEM error to altitude ratio assuming that no attitude error exits. Assuming the mean values of $h, \theta, \psi, \Delta v_y$ and Δv_z are zero, and assuming velocity, attitude and DEM errors are independent, the variance of the ATI phase in terms of the DEM uncertainty can be derived and given by

$$\begin{aligned}\sigma^2_{\Delta\Phi} = \frac{4k^2B^2}{H^2}\sigma_h^2\Bigg[&\cos^2\phi_s\sin^2\theta_i\cos^4\theta_i\frac{v_{ox}^2}{v_y^2} \\ &+ \sin^2\phi_s\sin^2\theta_i\cos^4\theta_i\left(2 + \frac{v_{oy}^2}{v_y^2}\right) \\ &+ \sin^4\theta_i\cos^2\theta_i\frac{v_{oz}^2}{v_y^2}\Bigg] \end{aligned} \tag{6.11}$$

Note that the variance of the ATI phase derived here is a function of only the DEM uncertainty by assuming that the INS can make perfect measurements and setting the uncertainties in aircraft attitudes and velocities $(\sigma_\theta, \sigma_\psi, \sigma_{v_y}, \sigma_{v_z})$ to zeros. Equation (6.11) indicates that the ATI phase error introduced by the DEM uncertainty is related to the imaging geometry, i.e., the incidence and squint angles.

6.3 Results and Summary

Based on the derivation of Equation 6.11, we performed the numerical analysis of the ATI phase in terms of the imaging geometry and DEM uncertainty. To be consistent with the previous study, we still focus on the case where the scatterers are stationary, i.e. $v_{ox} = v_{oy} = v_{oz} = 0$. Since the antenna has a beamwidth of 30° in the elevation plane, the

incidence angle of the system will vary from 45° to 75°. We computed the ATI phase error for different incidence angles over different levels of DEM uncertainties using the same imaging configuration from the real farmland experiment shown in Table 6.1. The results are plotted in Figure 6.2.

Table 6.1: List of parameters for computing the ATI phase error due to DEM uncertainty.

Parameter	Description	Value	Unit
k	Wavenumber	113.8	rad/m
B	Antenna baseline	0.4	m
θ_i	Incidence angle	60	degree
ϕ_s	Squint angle	30	degree
H	Platform height	800	m
σ_h	DEM uncertainty	12	m

From Figure 6.2 one can see that the ATI phase error increases approximately linearly as the incidence angle decreases, which makes sense since greater incidence angles correspond to longer distances, and the longer the distance, the less sensitive the path length difference becomes for a fixed height error, and thus, a smaller phase error. Note that the DEM we used in the SAR processing was obtained from the spaceborne SRTM, with a height accuracy of about 12 m. From the plots, we also find that the phase error introduced by the 12 m DEM uncertainty is about 0.21 radians for a 60° incidence angle, which corresponds to the boresight of the antenna. Therefore, the DEM error does introduce certain amount of phase error which ranges from 0.1 to 0.3 radians, which translates to about 5 cm/s to 15 cm/s of radial velocity error. This DEM introduced error accounts for a great portion of the phase offset we observed in the real farmland interferogram and should be taken care of in the

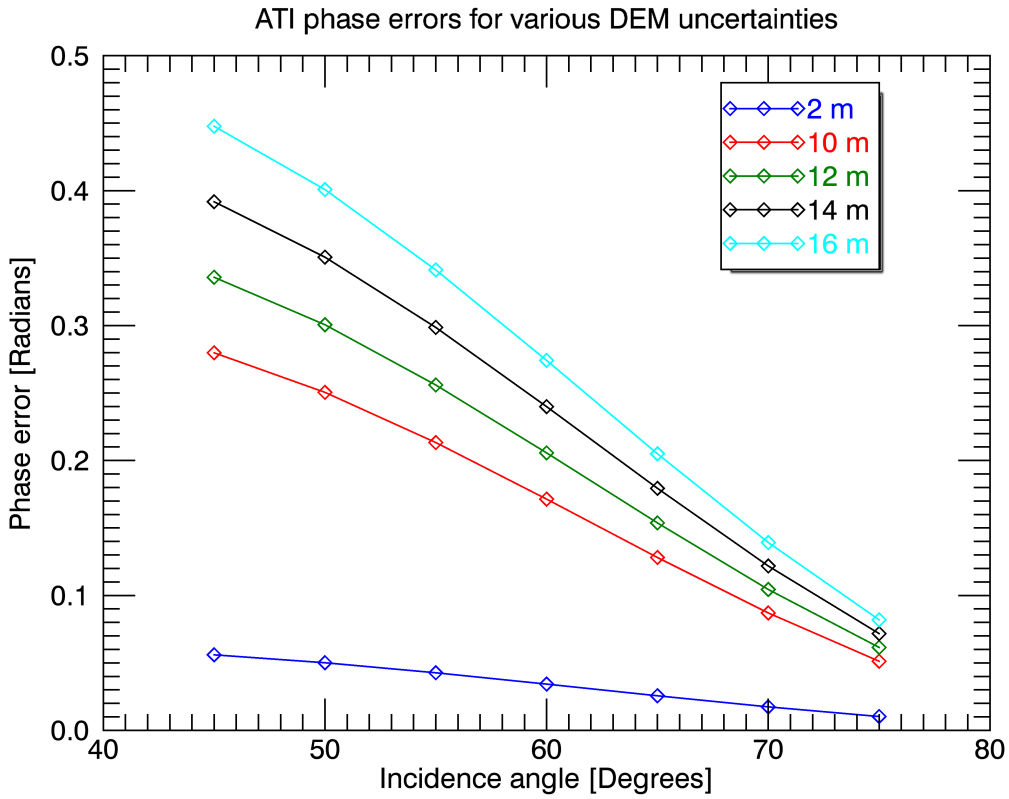

Figure 6.2: ATI phase errors over different incidence angles due to inaccurate DEM.

future data processing. One approach to reduce the effect of the DEM error on the ATI phase error is to utilize some commercial DEMs with better accuracy, although they are not free and cost more. For example, the WorldDEM provided by the more recent spaceborne mission TanDEM-X has a height accuracy better than 2 m, which will only introduce about 0.03 radians of phase error if we refer to the plot in Figure 6.2.

Chapter 7

ANALYSIS OF GEOPHYSICAL RETRIEVAL ERRORS OF OCEAN SURFACE CURRENTS BY ATI-SAR

7.1 Overview of Geophysical Retrieval Errors

As mentioned earlier in Chapter 2, the radial velocity estimated by ATI-SAR is the combined contributions of surface currents, long gravity waves and Bragg-waves. Previous chapters present approaches to minimize the errors on the ATI phases (or radial velocity u_r) estimated by the radar system. To obtain accurate surface currents velocity estimates, one also needs to remove the contributions from the orbital velocities of the long gravity waves and the net Bragg-wave phase velocity. The Bragg-wave's contribution can be estimated using the model proposed in [26, 61] and local wind measurements. However, the estimation of the contribution of long gravity waves has been a challenging task and a few different studies have reported the observations of the significant impacts of long ocean waves on surface currents retrieval [14, 19, 62, 63]. Aslebash from the microwave remote sensing lab at UW-APL is working on modeling the effect of long ocean waves during her Ph.D. [64]. This chapter provides our observations of ocean wave effects on ATI-SAR surface currents retrieval and the test of the M4S model [65] for the estimation of effects of orbital ocean waves. Moreover, the well-known azimuthal displacement of moving surface scatterers in SAR imaging might also introduce certain amount of distortions on the imaged velocity fields. Therefore, these geophysical retrieval error sources must be considered and mitigated during the ATI-SAR processing in order to retrieve accurate surface currents velocity. Note that most of the contents in this chapter are cited from the author's paper in 2016 [66].

7.2 Experiments and Observations

A number of field experiments have been conducted at the New River Inlet (NRI), NC, USA with UW-APL dual-beam ATI-SAR. The radar imaged area is shown in Figure 7.1. NRI is a tidally driven inlet: during the flood period, the seawater is flowing from the Atlantic Ocean into the inlet while during the ebb period, the seawater is flowing from the inlet into the ocean. During the experiment, surface drifters were also deployed into the ocean to provide the in situ measurement of ocean surface currents with very high accuracy ($<$ 0.15 cm/s). It shows that the surface current velocity estimated by SAR differs from the in situ measurement made by surface drifters in both magnitude and direction. Table 7.1 and Table 7.2 provides a summary of the root mean squared (RMS) errors in both magnitude and direction for data collected during the NRI campaign on different flight paths on different days. Figure 7.2 shows radar and drifter measurements of the current at a tidally-driven inlet during a period of maximum ebb flow. The calculated RMS error between them is 43 cm/s in magnitude and 35 degree in direction (in mathematical coordinates). While some velocity vectors agree well, we see that most of the radar measurements are biased slightly towards the east. Clearly, these distortions are significant compared with the typical mean value of the current measurement (70 cm/s) at the NRI. The errors in current velocity estimates can be due to various sources, which will be discussed in this chapter.

As is shown in Figure 7.2, errors between SAR measurements and surface drifter measurements of surface currents velocity fields have been observed and the velocity bias exists in both magnitude and direction. More specifically, we saw eastward velocity bias in the SAR measurements with respect to the drifter measurements for NRI at specific environment condition and radar imaging geometry. In this chapter, we will focus on the possible geophysical retrieval errors in converting the ATI-SAR velocity to surface current velocity estimates.

Table 7.1: Summary of error between SAR and surface drifter measurements when the radar is looking alongshore at NRI, NC, USA in May 2012.

	SW→NE, looking offshore		NE→SW, looking onshore	
Date	Magnitude [m/s]	Angle [degree]	Magnitude [m/s]	Angle [degree]
May 02	0.41	69.37	0.32	48.64
May 07	0.29	64.43	0.37	59.90
May 10	0.34	49.80	0.38	38.12
May 13	0.17	24.08	0.27	26.99
May 18	0.39	40.30	0.62	34.55

7.3 Gradient-induced Distortion

It is well-known that SAR imaging mechanism for moving targets that have a radial velocity component relative to the SAR flight direction will introduce an azimuthal displacement from their true positions [67]. This effect also applies to the imaging of a moving ocean surface. Since the amount of displacement is relative to the value of radial velocity measurement, the value of the displacement will vary with a spatially varying current profile and can cause distortion on measured velocity fields. For a dual-beam ATI SAR system, this kind of distortion may become even more complicated because the distortions for the two beams will be different for most of the scene that the radar is looking at [68]. Here we studied on the effect of this gradient-induced distortion and simulated this effect based on a simulated surface current field at NRI.

Starting with the imaging geometry described in Figure 5.3, SAR imaging mechanism shifts the moving scatterers azimuthally and the horizontal shift unit vector perpendicular

Table 7.2: Summary of error between SAR and surface drifter measurements when the radar is looking crossshore at NRI, NC, USA in May 2012.

	SW→NE, looking offshore		NE→SW, looking onshore	
Date	Magnitude [m/s]	Angle [degree]	Magnitude [m/s]	Angle [degree]
May 02	0.36	44.64	0.31	48.89
May 07	0.25	54.45	0.25	46.14
May 10	0.43	62.07	0.37	57.50
May 13	0.43	54.53	0.28	21.34
May 18	N/A	N/A	0.59	51.88

to the line of sight is

$$\hat{d} = \langle -\sin\phi_s, \cos\phi_s \rangle. \tag{7.1}$$

where ϕ_s denotes the squint angle of the radar beam. The amount of displacement is proportional to the radial velocity of the scatterers and the displacement vector from the true scatterer position to the shifted scatterer position is

$$\hat{d}(\hat{p}) = -\frac{R}{v_p} u_r(\hat{p})\hat{d} \tag{7.2}$$

where $\hat{p}$ is the position vector of the scatterer on the surface, $\hat{d}$ is the unit displacement vector. R is the distance between the radar and the scatterer, v_p is the speed of the aircraft and u_r is the radial component of the surface velocity. The radial component of the velocity field is mapped to the radar image space with the transformation

$$u_{ri}(\hat{p} + \hat{d}(\hat{p})) = u_r(\hat{p}). \tag{7.3}$$

This mapping distorts the true velocity field spatially. Note that the mapping is only valid

Figure 7.1: The google earth image of New River Inlet, NC, USA. The area imaged by the radar during the campaign is in the yellow tile with the dimension of about 2 km by 2 km.

when the gradient of the radial component of the velocity field is less than a critical value [68], i.e.,

$$\frac{\partial u_r}{\partial \hat{d}} < \frac{v_p}{R} \tag{7.4}$$

where $\frac{\partial}{\partial \hat{d}}$ is the directional derivative in the $\hat{d}$ direction. When the gradient of the radial velocity field equals this critical value, the mapping from true position to radar image space becomes a many to one mapping. In this case, the velocity measured by SAR should not be used, or considered to introduce a large error. Finally, assuming the contribution from the vertical velocity component is small, we can estimate the x and y components of the shifted velocity fields using (2.8) by replacing u_r^+ with u_r^- with u_{ri}^+ and u_{ri}^-.

A simulated velocity field for the NRI is generated from a hydrodynamic model using the

regional ocean modeling system (ROMS). Then we apply the above distortion mechanism to shift the simulated surface currents field (considered to be the true currents field). By comparing the shifted velocity vector field with the true velocity field, we can tell how much error is introduced by the gradient-induced distortion.

We plotted the distorted current field and the simulated current field (considered as the ground truth) in Figure 7.3. We find that the distorted current field (green) aligns with the simulated field (blue) well in direction for most of the area. The calculation shows that the RMS difference between the simulated and distorted field is 19 cm/s in magnitude and about 1 degree in direction, indicating that the gradient-induced distortion contributes to some errors in magnitude but cannot explain the eastward bias seem in the ATI-SAR estimated velocity field.

7.4 Wave-dependent Velocity Bias

The radial velocity measured by ATI-SAR is an estimate of the mean Doppler shift induced by the surface motion on the incident electromagnetic wave. This mean Doppler shift includes contributions from surface current, the phase velocity of Bragg-resonant wave and the orbital motion of long gravity waves. To retrieve the surface current, one needs to remove the contributions of the Bragg waves and the long gravity waves from the radar measurement. The Bragg wave contribution (u_r^B in Equation (2.6)) to the Doppler shift can be estimated using a model proposed in [61] and local wind measurements. (1) (2) (3) in [26] details the estimation approach for Bragg-resonant wave contribution used in our study.

The contributions of the orbital velocities of the long gravity waves introduces an additional velocity term in the Doppler measurement, i.e., u_r^m in Equation (2.6). As long waves propagate through the short wave field, two adjustments to the short waves are made that directly change the intensity and thus imaging of radar returns. Figure 7.4 [9] illustrates these two types of modulations. The first, tilt modulation, is when the varying slope of the long wave changes the local orientation or tilt of the short waves. These tilting waves act as reflecting mirrors or facets to the incoming electromagnetic waves, so that the return will

vary as the facets change tilt along the longer propagating wave. The second adjustment, hydrodynamic modulation, takes place when the amplitudes of the short wave field are non-uniformly altered by the long wave in the following ways: the long wave orbital velocities shown in Figure 7.5 have different directions along the wave, which tends to pile up short waves in the convergence zones (crest) and spread them out in the divergence zones (trough); and the airflow over the long waves is distorted, thereby preferentially forming short waves at the crest as compared to the trough. Both tilt and hydrodynamic modulations have the strongest effects on the radar returns when the long waves are propagating perpendicular to the platform direction. Thus, the backscattered signal has different intensity at different locations along the long ocean waves, resulting in a nonzero velocity component even after averaging the measurements over large areas. However, this term hasn't been removed from the ATI-SAR measured radial velocity so far. To compute the contributions of the orbital motions of long gravity waves, we first need an estimate of the ocean wave spectra. A nonlinear integral transform relating ocean wave spectra to the ATI-SAR phase image spectra was derived by Bao et al. [69]. They replaced the full nonlinear mapping relation by the linear approximation for the special case in which the nonlinearity parameter is small. Therefore, the linear transform can be used to invert ATI-SAR phase image spectra into ocean wave spectra. However, the transform also requires the knowledge of ocean wave such as the wavenumber and the azimuthal angle of the dominant ocean wave.

To study the effect of the orbital motions of long gravity waves, we used the M4S model developed by Romeiser and Thompson [65], which computes mean Doppler estimates and ATI-SAR radial velocities from input current and wind fields. We first used the ROMS simulated surface current field and wind field as input to the model. Figure 7.6 shows the plots of the simulated surface current field, the ATI-SAR measurement and the output of the M4S simulation for NRI. Note that the Bragg wave phase velocity was estimated [26] and subtracted from the SAR measurement and the output of the M4S simulation in Figure 7.6. We find that the ATI-SAR measurement agrees with M4S model output over most of the area, indicating that the model reproduces the ATI-SAR measurement quite well. Also,

the M4S model output captures some of the eastward velocity bias observed in the SAR measurement.

As gradient-induced distortion cannot explain the observed eastward bias, we hypothesize that the eastward velocity bias results from the orbital motion of ocean gravity waves. Again, the M4S model was applied to compute the radial velocity, but with zero current field and the modeled wind field as input. The corresponding output is the mean Doppler due to the waves and Bragg scatterers. Then we subtract an estimate of the Bragg wave contribution from the M4S-computed radial velocities to get an estimate of the contribution of the gravity waves to the ATI radial velocity estimates. The resulting long gravity wave velocity is 22 cm/s and 15 degree counterclockwise from east and is shown in Figure 7.7. We plot the vector summation of the true current and the gravity wave velocity component together with the true current field and the ATI-SAR measurement in Figure 7.8, and find that the wave-biased current field captures some of the eastward bias seen in the SAR measurement. Hence, much of the ATI SAR measurement bias can be explained by the gravity wave-induced bias on the Doppler shift. Note that the wave-biased current will not perfectly match with the SAR measurement since the wave spectrum computed by the M4S model will probably not match with the true wave spectrum for the inlet due to the lack of precise environment conditions and the breaking waves present in the inlet is also not accounted for by the model.

7.5 Summary

Significant measurement errors were observed in both magnitude and direction between SAR and surface drifters at the a tidally-driven inlet (NRI) site. We analyzed possible geophysical retrieval errors of ATI-SAR for estimating ocean surface currents. The gradient-induced distortion is found not significant for the directional bias observed at the NRI site. The error has proved to be more related to the wave-dependent bias through simulations with a hydrodynamic model (ROMS) and the M4S model which is used to simulate the Doppler measurements by the ATI-SAR.

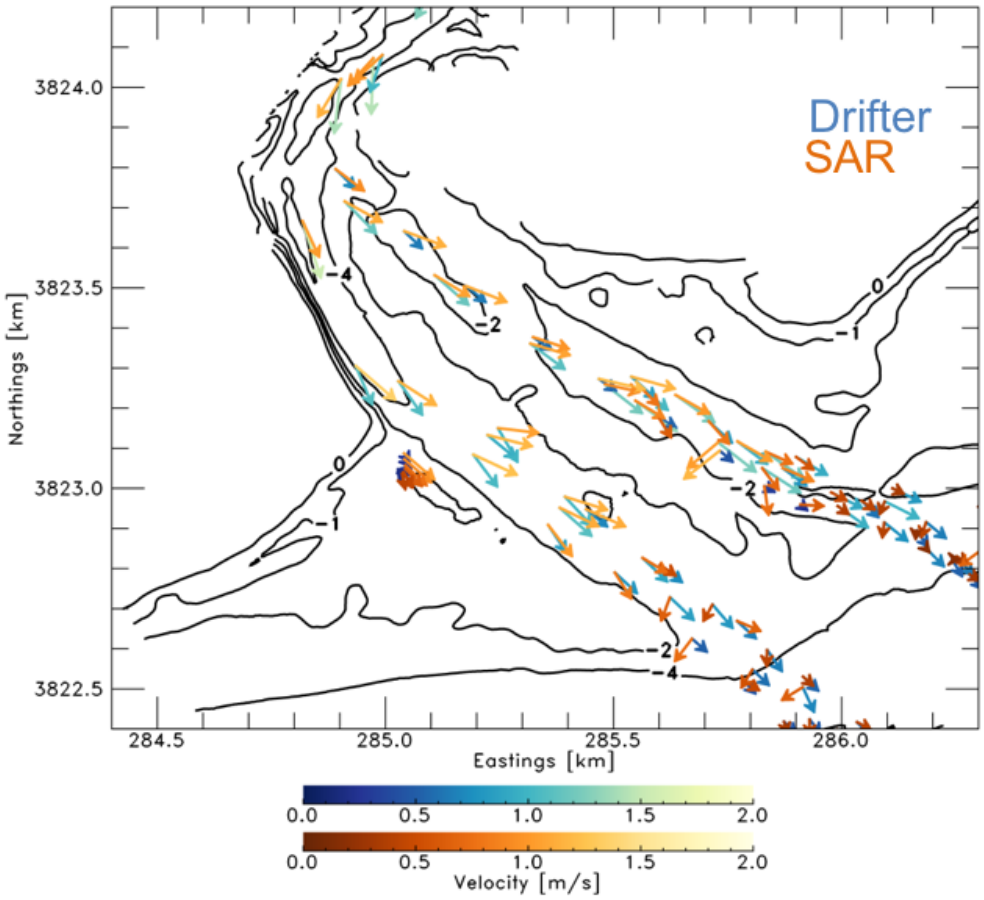

Figure 7.2: SAR (brown) and surface drifter (blue) measurements for surface current field at NRI, NC, USA during an ebb period when the water is flowing from the inlet into the ocean. Note that the phase offset from the radar channel and antenna as well as the the Bragg wave contribution has been removed from the SAR measurement.

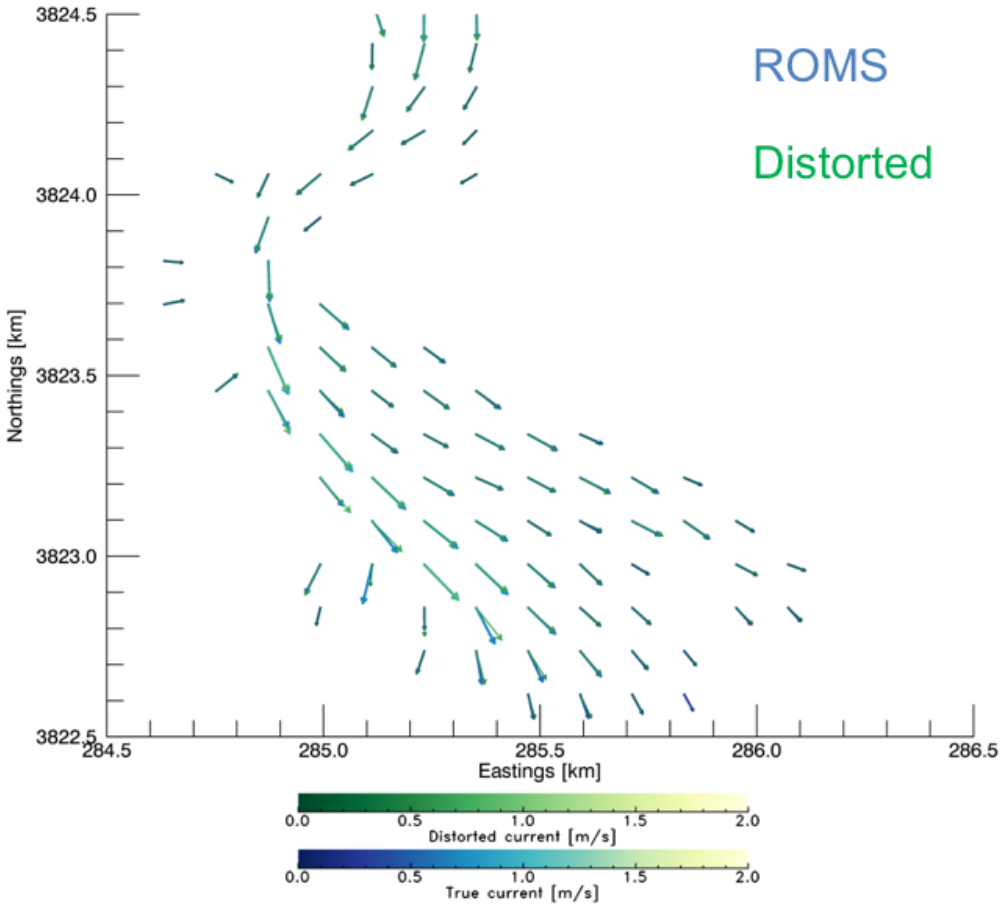

Figure 7.3: The simulated surface currents vectors with ROMS model (blue) and distorted current vectors (green) for New River Inlet, NC, USA. The simulated currents fields are used as the ground truth to compare with the distorted currents fields.

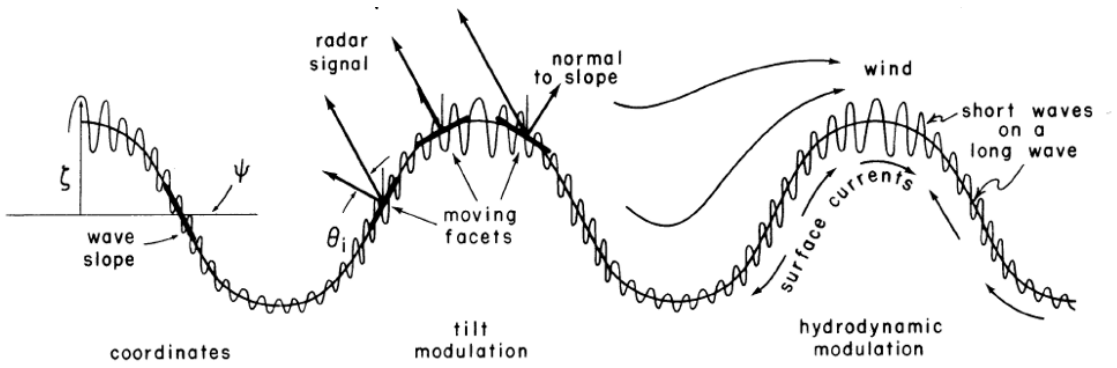

Figure 7.4: Illustration of tilt and hydrodynamic modulation. The longer waves change the local orientation or slope (tilt modulation) and distribution (hydrodynamic modulation) of the shorter wave fields. Reprinted from [9].

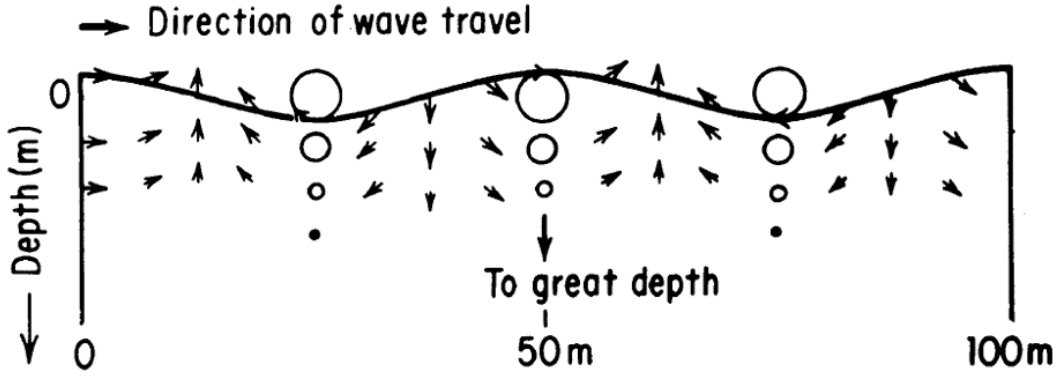

Figure 7.5: Instantaneous velocity vectors and orbital paths of fluid particles in a long wave in deepwater. Reprinted from [9].

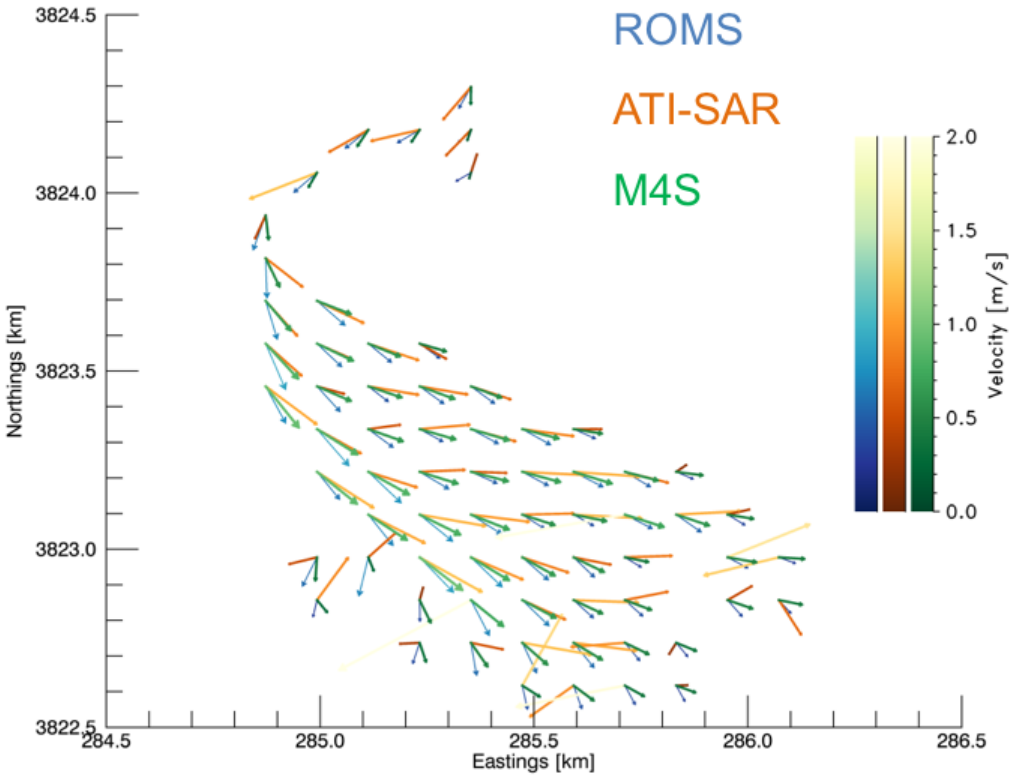

Figure 7.6: The simulated current field with ROMS model (blue) as the ground truth, ATI-SAR measurement (brown) and output of M4S model (green) at NRI, NC, USA. Note that the phase offset from the radar channel and antenna as well as the the Bragg wave contribution has been removed from the SAR measurement and the output of the M4S simulation.

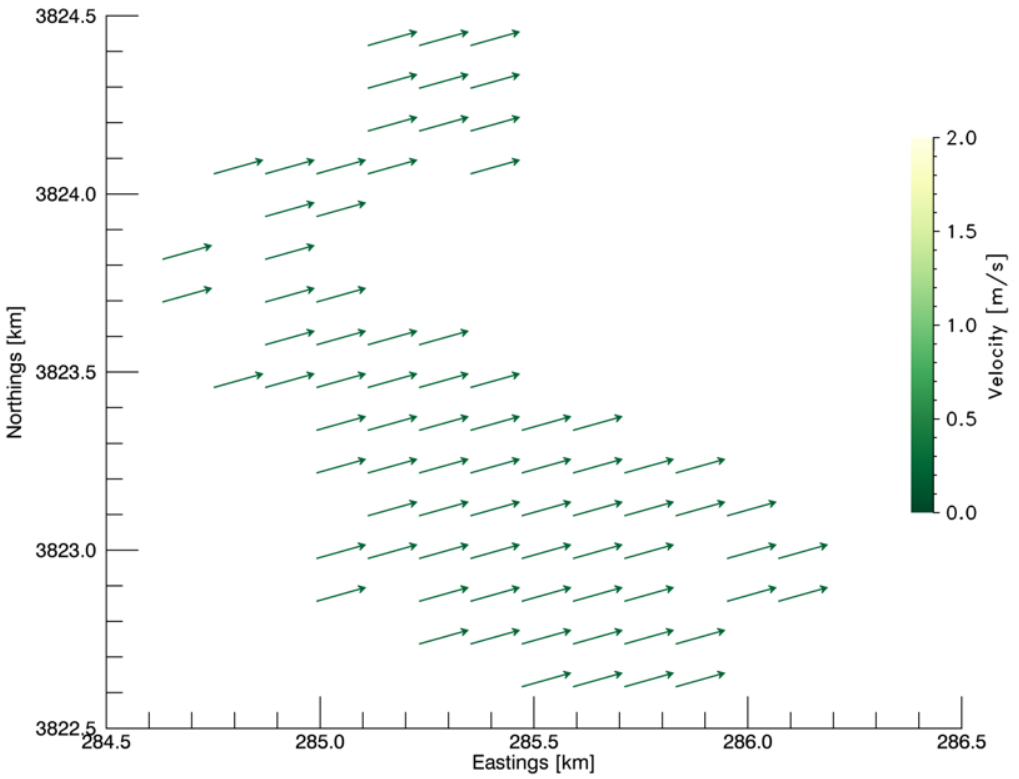

Figure 7.7: Estimated velocity contributions from the orbital motion of long gravity waves with the M4S model.

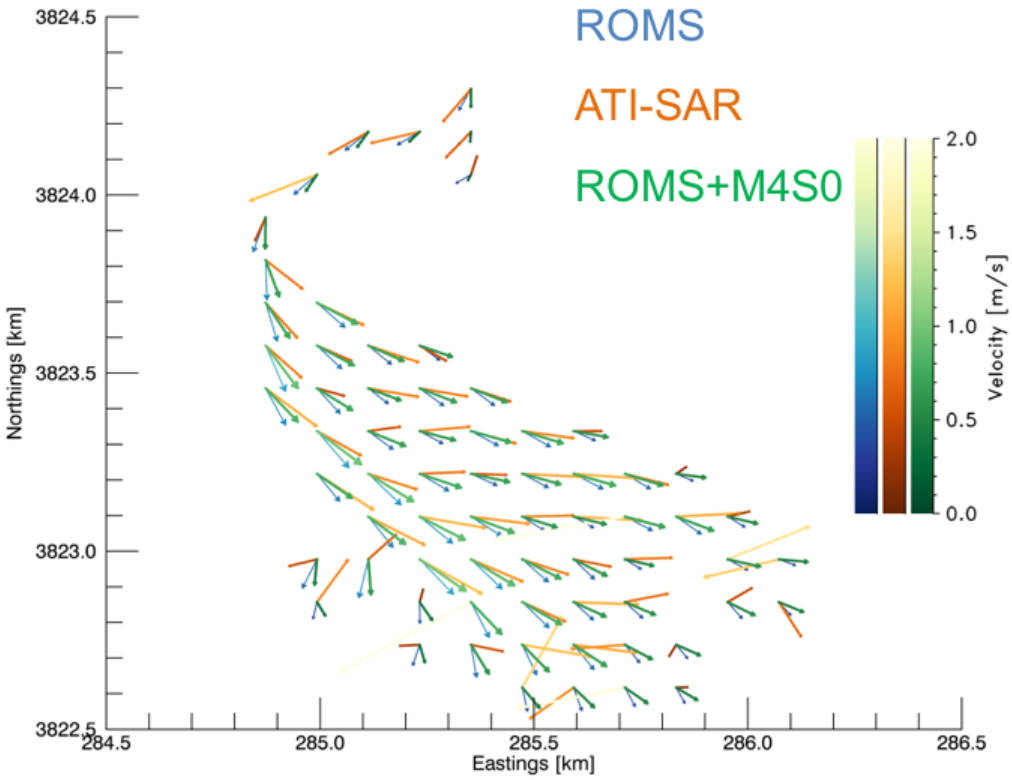

Figure 7.8: Simulated currents field with ROMS model (blue) as the ground truth, currents field from ATI-SAR measurement (brown) and wave biased currents field (green) with M4S model with zero currents at the input at NRI, NC, USA. Note that the phase offset from the radar channel and antenna as well as the the Bragg wave contribution has been removed from the SAR measurement and the output of the M4S simulation.

Chapter 8

CONCLUSIONS

Knowledge of ocean currents is important for understanding ocean circulation, ship navigation as well as coastal engineering. Ocean currents have been monitored with in-situ point sensors for a long period before airborne/spaceborne SAR interferometry was employed to cover a vast area of the ocean surface. The long synthetic aperture of the radar mounted on a moving platform makes the formation of high-resolution ocean surface currents maps possible. The repeat pass SAR interferometry, which contains only one radar with two receivers separated by a small baseline distance, can only measure the velocity between the radar and surface scatterer in the line of sight direction. To retrieve the 2-D surface currents map, at least two flights of measurements, ideally perpendicular to each other and with little temporal difference, are required. The dual-beam ATI SAR overcomes these limitations by employing two squinted ATI-SARs with each squinted beam measuring one radial velocity from a specific direction. Therefore, it can generate the 2-D surface currents map within a single flight. Field experiments have shown that the ATI-SAR measurements of surface currents can roughly agree with the in-situ currents measurement in directions. However, the deviations of SAR measurements from in-situ measurements of currents velocities have been observed during most of the field experiments. The measurement errors can result from two major category of error sources. The first category comes from the system itself, which contains errors from radars, antennas and the GPS/IMU. The second category of error sources is due to geophysical retrieval errors. As described in Chapter 1 and Chapter 7, the motion measured by InSAR has mixed contributions from surface currents and waves. The waves contribution to Doppler measurements by the radar can be significant and must be removed to retrieve the correct surface currents velocities. In Chapter 7, an initial study on

the wave's effect on ATI-SAR currents retrieval was introduced. However, this area of study will include sophisticated ocean scattering models and different hydrodynamic models and is not within the scope of our study. Our study mainly focused on studying the first category of error sources, i.e, the systematic errors from the instruments, and possible calibration approaches to mitigate the systematic errors.

Starting with the observed interferometric phase error over the stationary land areas during field experiments, we hypothesized all possible system error sources and performed the comprehensive error analysis to verify the hypothesis and identify the contribution of each potential error source to the total observed ATI phase error. In Chapter 3, we studied the cause of range-dependent phase ripple and demonstrated that it is mainly due to the phase mismatch between the two receiver channels of the radar. We designed a lab-controlled experiment to characterize the phase response of each receiver channel and estimated the phase ripple for each channel. The calculated standard deviation of the phase ripple can be as high as 0.2 radians. After applying the estimated phase ripple in the SAR processing, the observed range-dependent phase ripple has been greatly attenuated and almost visually gone. The direct spectral estimate of the ATI phase in range direction has shown a reduction of 14 dB after calibration. The calibration schemes derived for the dual-channel FMCW transceiver can be adapted to calibrate the phase mismatches for any multi-channel FMCW system, which is important for performing radar interferometry.

After the range-dependent phase fluctuations were removed from the interferogram after phase ripple calibration, one can still observe non-zero phase offset which varies slowly in range. Since the calibration experiment was conducted in the lab and the antennas were taken off during the experiment, we hypothesized that the remaining phase offset were mainly caused by the mismatch between the receive antennas' phase pattern. An approach to directly estimate the mismatch between receive antenna phase pattern was derived in Chapter 4 and applied to the interferogram to further calibrate the residual phase offset in range. After calibration, the remaining phase offset was greatly reduced and became much closer to zero, which further verified our hypothesis. However, the estimated phase mismatches from

different dataset shows certain level of variations in the mean phase offset. Future study will try to understand the cause for the variations.

Since the time-domain backprojection algorithms in the SAR processing requires accurate knowledge of both antenna positions and scatterer's height, the uncertainties in the aircraft attitude and velocity measurements made by the GNSS/INS and the uncertainty in the DEM used during the processing may result in path length error between the antenna and the scatterer. The path length error will result in error in the ATI phase during the azimuth compression of SAR image formation. Chapter 5 and 6 studies the effect of the INS uncertainties in aircraft attitude and velocity measurements and the effect of the DEM uncertainty, respectively, on the ATI phase error by mathematical derivation and simulations. It has been demonstrated that the INS uncertainty in attitude measurement does account for most of the phase undulations observed in the along-track direction of the interferogram. The DEM uncertainty greater than 10 m will introduce an ATI phase error greater than 0.2 radians, which can not be neglected for accurate ocean surface velocity retrieval and needs to be taken care of. Although this may be true for land scatterers, the DEM uncertainty will be less of an issue for ocean surface remote sensing because the ocean surface elevation in coastal region is usually surveyed well through tide measurements, with an accuracy of usually less than one meter.

To summarize, a comprehensive systematic error source analysis was conducted to improve the accuracy of the ATI-SAR measurement of ocean surface currents. We studied the effect of the phase mismatch between the receive channels, phase imbalance between receive antennas, INS measurement uncertainty and DEM errors, respectively, on the interferometric phase after SAR processing. Calibration approaches for the first two error sources were presented to mitigate the observed phase error. With the stationary farmland data whose phase should be zero as the test dataset, the initial ATI phase error before calibration can be as high as 1.2 radians. After phase calibration, the RMS phase error can be reduced by almost 1 radian. The DEM error analysis shows that with a more accurate DEM better than 3 m uncertainty, one can further reduce the phase error by 0.2 radians. In conclusion,

after applying all the calibration schemes derived in this study, the system phase error can be reduced by as much as 1 radians, which corresponds to about 58 cm/s error in surface velocity estimate based on the default system imaging configuration. The typical value of the near-shore ocean surface currents can vary from a few tens of cm/s to 1 m/s for a tidally-driven inlet, which means the proposed system error calibration schemes will have significant impacts on improving the accuracy on ocean surface currents retrieval by long-track SAR interferometry. Also recall that the long ocean waves will also introduce significant errors to the Doppler velocity estimated by SAR. The study on characterizing the contributions of ocean waves to the ATI-SAR measurement will be an inevitable step to mitigate the geophysical retrieval error and improve the ocean surface currents estimation accuracy, together with the system error calibration schemes.

Table 8.1 shows the comparison between the ATI-SAR measurements and the conventional in-situ measurements of ocean currents. The acoustic doppler current profiler (ADCP) has an accuracy of a few cm/s for currents measurement. The surface drifters (SWIFT) employed by the UW-APL engineers can achieve an accuracy of less than 5 cm/s. Note that although these in-situ measurements have slightly better accuracy than what the ATI-SAR can achieve, they are the time-averaged measurements over a period of a few minutes or more. Meanwhile, they are point sensors and can only cover a very limited area of the ocean surface. In comparison, the ATI-SAR measurements can take current measurements within less than 30 seconds and can provide a high resolution surface currents map with wide coverage of the ocean surface. The ocean currents maps used by the oceanographers nowadays have very coarse resolution which can be as high as a few kilometers, with a few tens of cm/s error in velocity. Therefore, the high resolution currents map on the order of meters is of great importance to validate and improve the ocean models.

Table 8.1: Comparison between the ATI-SAR and conventional in-situ measurements for ocean currents.

Instrument	**Accuracy**	**Coverage**	**Temporal Resolution**
ADCP	A few cm/s (with averaging)	Limited	A few minutes
Surface Drifters (SWIFT)	< 5 cm/s (with averaging)	Limited	A few minutes
ATI-SAR	14 cm/s	Wide	30 seconds

BIBLIOGRAPHY

[1] C. Foley, "Nearshore buoys deployed off waukegan and winthrop harbor," http://www.iiseagrant.org/newsroom/lake-michigan-gains-two-new-buoys/, Jul. 2018, accessed: 2018-12-05.

[2] Q. E. Solutions, "Hf radar," https://www.phenixa.radeel.qualitasenv.com/index.php/produits/par-application#radarhf, accessed: 2018-12-05.

[3] R. K. Green, "Scaled synthetic aperture radar system development," Master's thesis, California Polytechnic State University, San Luis Obispo, CA, Dec. 2015.

[4] D. Kim, W. Moon, D. Moller, and D. Imel, "Measurements of ocean surface waves and currents using L- and C-band along-track interferometric SAR," *IEEE Trans. Geosci. Remote Sens.*, vol. 41, no. 12, pp. 2821–2832, Dec. 2003.

[5] H. Deng, Y. Goncharenko, and G. Farquharson, "Phase calibration of an along-track interferometric FMCW SAR," in *IEEE Int. Geosci. Remote Sens. Symp.*, Jul. 2013.

[6] M. Edwards, D. Madsen, C. Stringham, A. Margulis, B. Wicks, and D. Long, "microASAR: A small, robust LFM-CW SAR for operation on UAVs and small aircraft," in *IEEE Int. Geosci. Remote Sens. Symp.*, vol. 5, July 2008, pp. V–514–V–517.

[7] H. Deng and G. Farquharson, "A robust phase calibration algorithm for a dual-channel along-track interferometric FMCW SAR," in *IEEE Int. Geosci. Remote Sens. Symp.*, Jul. 2014.

[8] T. M. Company, "Pitch, roll, and yaw," https://www.touringmachine.com/Articles/aircraft/6/, accessed: 2018-12-05.

[9] *Synthetic Aperture Radar Marine User's Manual*, National Oceanic and Atmospheric Administration, Sep. 2004, technical Manual.

[10] G. Franceschetti and G. Schirinzi, "A sar processor based on two-dimensional fft codes," *IEEE Trans. Aerosp. Electron. Syst.*, vol. 26, pp. 356–366, March 1990.

[11] R. M. Goldstein and H. A. Zebker, "Interferometric radar measurement of ocean surface currents," *Nature*, vol. 328, no. 6132, pp. 707–709, 1987.

[12] R. M. Goldstein, T. P. Barnett, and H. A. Zebker, "Remote sensing of ocean currents," *Science*, vol. 246, no. 4935, pp. 1282–1285, 1989.

[13] L. Shemer, M. Marom, and D. Markman, "Estimates of currents in the nearshore ocean region using interferometric synthetic aperture radar," *J. Geophys. Res.*, vol. 98, no. C4, pp. 7001–7010, 1993.

[14] H. C. Graber, D. R. Thompson, and R. E. Carande, "Ocean surface features and currents measured with synthetic aperture radar interferometry and HF radar," *J. Geophys. Res.*, vol. 101, no. C11, pp. 25 813–25 832, Nov. 1996.

[15] E. Rodriguez, D. Imel, and B. Houshmand, "Two-dimensional surface currents using vector along-track interferometry," in *Proc. PIERS'95*, Seattle, WA, 1995, p. 763.

[16] S. Frasier and A. Camps, "Dual-beam interferometry for ocean surface current vector mapping," *IEEE Trans. Geosci. Remote Sens.*, vol. 39, no. 2, pp. 401–414, Feb. 2001.

[17] G. Farquharson, W. N. Junek, A. Ramanathan, S. J. Frasier, R. J. Tessier, D. J. McLaughlin, M. A. Sletten, and J. V. Toporkov, "A pod-based dual-beam SAR," *IEEE Geosci. Remote Sens. Lett.*, vol. 1, no. 2, pp. 62–65, Apr. 2004.

[18] J. Toporkov, D. Perkovic, G. Farquharson, M. Sletten, and S. Frasier, "Sea surface velocity vector retrieval using dual-beam interferometry: first demonstration," *IEEE Trans. Geosci. Remote Sens.*, vol. 43, no. 11, pp. 2494–2502, Nov. 2005.

[19] A. Martin, C. Gommenginger, B. Chapron, J. Marquez, S. Doody, D. Cotton, and C. Buck, "Dual beam along-track interferometic sar to map total ocean surface current vectors with the airborne wavemill proof-of-concept instrument: Impact of wind-waves," in *Geoscience and Remote Sensing Symposium (IGARSS), 2015 IEEE International*. IEEE, 2015, pp. 4069–4072.

[20] G. Farquharson, S. Aslebagh, and J. Mower, "Calibration of a miniaturized fmcw ati-sar for normalized radar cross section measurement," in *2015 IEEE Int. Geosci. Remote Sens. Symp.*, 2015.

[21] G. Farquharson and J. Thomson, "Airborne microwave radar measurements of surface velocity in a tidally-driven inlet," Dec. 2012, AGU Fall Meeting.

[22] G. Farquharson, H. Deng, Y. Goncharenko, and J. Mower, "Measurements of the nearshore ocean with FMCW ATI SAR," in *10th European Conference on Synthetic Aperture Radar*, 2014.

[23] S. Aslebagh and G. Farquharson, "Wave period and direction estimation in shallow water using airborne along-track interferometric synthetic aperture radar," in *IEEE Int. Geosci. Remote Sens. Symp.*, Jul. 2015.

[24] G. Farquharson, S. Aslebagh, and R. Romeiser, "Estimating nearshore ocean currents from airborne ati-sar," in *11th European Conference on Synthetic Aperture Radar*, 2016.

[25] S. Aslebagh, G. Farquharson, E. Rodriguez, and D. Perkovic-Martin, "Nearshore ocean surface current estimation comparison in c-band and ka-band," in *IEEE Int. Geosci. Remote Sens. Symp.*, Jul. 2017.

[26] G. Farquharson, H. Deng, Y. Goncharenko, and J. Mower, "Dual-beam ATI SAR measurements of surface currents in the nearshore ocean," in *2014 IEEE Int. Geosci. Remote Sens. Symp.*, 2014.

[27] A. Recchiao, A. Monti Guarnieri, A. Broquetas, and R.-R. J., "Assesment of atmospheric phase screen impact on geosynchronous SAR," in *Proc. IEEE Geosci. Remote Sens. Symp.*, Jul. 2014, pp. 2253 – 2256.

[28] X. Ding, Z. Li, and J. Zhu, "Atmospheric effects on insar measurements and their mitigation," *Sensors*, vol. 8, no. 9, pp. 5426–5448, 2008.

[29] M. Pinheiro, P. Prats, S. R., and F. J., "Multi-path correction model for multi-channel airborne SAR," in *Proc. IEEE Geosci. Remote Sens. Symp.*, vol. 3, Jul. 2009, pp. 729 – 732.

[30] Y. Mao, M. Xiang, L. Wei, and S. Han, "The mathematic model of multipath error in airborne interferometric SAR system," in *Proc. IEEE Geosci. Remote Sens. Symp.*, vol. 2, Jul. 2010, pp. 2904 – 2907.

[31] M. Bachmann, M. Schwerdt, G. Castellanos Alfonzo, and D. Schrank, "Phase pattern calibration for interferometric applications in spaceborne sar systems," *International Journal of Antennas and Propagation*, vol. 2013, 2013.

[32] H. Zhang, J. Hong, X. Qiu, J. Li, F. Li, and F. Ming, "Effects of residual motion compensation errors on the performance of airborne along-track interferometric sar," *Frontiers of Information Technology & Electronic Engineering*, vol. 17, no. 10, pp. 1095–1106, 2016.

[33] D. R. Thompson and J. R. Jensen, "Synthetic-aperture radar interferometry applied to ship-generated internal waves in the 1989 Loch-Linnhe experiment," *J. Geophys. Res.*, vol. 96, no. C6, pp. 10 259–10 269, Jun. 1993.

[34] J. Thompson, "Wave breaking dissipation observed with swift drifters," *J. Atmos. and Oceanic Technol.*, vol. 29, no. 12, pp. 1866–1882, Dec. 2012.

[35] H. Deng, G. Farquharson, J. Sahr, Y. Goncharenko, and J. Mower, "Phase caliration of an along-track interferometric fmcw sar," *IEEE Trans. Geosci. Remote Sens.*, vol. 56, no. 8, pp. 4876–4886, 2018.

[36] G. O. Marmorino, D. R. Thompson, H. C. Graber, and C. L. Trump, "Correlation of oceanographic signatures appearing in synthetic aperture radar and interferometric synthetic aperture radar imagery with in situ measurements," *J. Geophys. Res.*, vol. 102, no. C8, pp. 18 723–18 736, Aug. 1997.

[37] M. Marom, L. Shemer, and E. B. Thornton, "Energy density directional spectra of a nearshore wave field measured by interferometric synthetic aperture radar," *J. Geophys. Res.*, vol. 96, no. C12, pp. 22 125–22 134, Dec. 1991.

[38] A. Meta, J. J. M. De Wit, and P. Hoogeboom, "Development of a high resolution airborne millimeter wave FM-CW SAR," in *First European Radar Conference (EURAD)*, 2004, pp. 209–212.

[39] M. Edrich, "Ultra-lightweight synthetic aperture radar based on a 35 GHz FMCW sensor concept and online raw data transmission," *IEE Proc. Radar Sonar Navig.*, vol. 153, no. 2, pp. 129–134, 2006.

[40] D. L. Bickel and W. H. Hensley, "Interferometric sar phase difference calibration: methods and results," in *Proc. 1994 IEEE Int. Geosci. Remote Sens. Symp.*, vol. 4, 1994, pp. 2259–2262.

[41] O. Hirsch, "Calibration of an airborne along-track interferometric sar system for accurate measurement of velocities," in *Proc. 2001 IEEE Int. Geosci. Remote Sens. Symp.*, vol. 1, 2001, pp. 558–560.

[42] J. L. Chau, D. L. Hysell, K. M. Kuyeng, and F. R. Galindo, "Phase calibration approaches for radar interferometry and imaging configurations: equatorial spread f results," *Ann. Geophys.*, vol. 26, Jan. 2008.

[43] N. Draper and H. Simith, *Applied Regression Analysis*, 3rd ed. John Wiley & Sons, Inc., 1998.

[44] C. Daniel and F. Wood, *Fitting Equations to Data: Computer Analysis of Miltifactor Data*, 2nd ed. John Wiley & Sons, Inc., 1999.

[45] K. Levenberg, "A method for the solution of centain non-linear problems in least squares," *Quart. Appl. Math.*, vol. 2, pp. 164–168, 1944.

[46] B. Boashash, "Estimating and interpreting the instantaneous frequency of a signal. II. algorithms and applications," in *Proc. 1992 IEEE*, vol. 80, Apr. 1992, pp. 540–568.

[47] S. Tretter, "Estimating the frequency of a noisy sinusoid by linear regression (Corresp.)," *IEEE Trans. Inf. Theory*, vol. 31, no. 6, pp. 832–835, Nov. 1985.

[48] S. L. J. Marple, "Computing the discrete-time analytic signal via FFT," *IEEE Trans. Signal Process.*, vol. 47, no. 9, pp. 2600–2603, Sep. 1999.

[49] S. L. Hahn, *Hilbert Transforms in Signal Processing*. Artech House, Inc., 1996.

[50] S. Weisberg, *Applied Linear Regression*, 3rd ed. Hoboken, NJ: Wiley, 2005.

[51] T. Abotzoglou, "Fast maximum likelihood joint estimation of frequency and frequency rate," *IEEE Trans. Acoust., Speech, Signal Process.*, vol. 11, pp. 1409–1412, 1986.

[52] P. O'Shea, "Fast parameter estimation algorithms for linear FM signals," in *1994 IEEE Int. Conf. Acoust., Speech, and Signal Process*, 1994, pp. 17–20.

[53] J. Hansen, "Selected approaches to estimation of signal phase," University of Rhode Island, Tech. Rep., 2003.

[54] P. O'Shea, "A new technique for instantaneous frequency rate estimation," *IEEE Signal Process. Lett.*, vol. 9, no. 8, pp. 251–252, 2002.

[55] ——, "A fast algorithm for estimating the parameters of a quadratic FM signal," *IEEE Trans. Signal Process.*, vol. 52, no. 2, pp. 385–393, 2004.

[56] D. C. Rife and R. R. Boorstyn, "Single tone parameter estimation from discrete-time observations," *IEEE Trans. Inf. Theory*, vol. 20, no. 5, pp. 591–598, 1974.

[57] D. B. Percival and A. T. Walden, *Spectral Analysis for Physical Applications: Multitaper and Conventional Univariate Techniques*. Cambridge University Press, 1993.

[58] H. Deng, G. Farquharson, M. Nalaban, A. Korovotniy, and Y. Goncharenko, "Analysis of velocity and attitude error in along-track interferometric SAR," in *IEEE Int. Geosci. Remote Sens. Symp.*, Jul. 2017.

[59] M. I. Duersch, "Backprojection for synthetic aperture radar," Ph.D. dissertation, Brigham Young University, Provo, Jun. 2013.

[60] A. Kovorotniy, M. Balaban, V. Gorobets, F. Kivva, Y. Goncharenko, G. Farquharson, and A. Jessup, "ATI SAR simulation shows signatures of complex objects," in *Proc. Int. Symp. Physics and Engineering of Microwaves, MM, and Sub-MM Waves*, 2016.

[61] D. Moller, S. J. Frasier, D. L. Porter, and R. E. McIntosh, "Radar-derived interferometric surface currents and their relationship to subsurface current structure," *J. Geophys. Res.*, vol. 103, no. C6, pp. 12 839–12 852, Jun. 1998.

[62] A. C. H. Martin, C. Gommenginger, J. Marquez, S. Doody, V. Navarro, and C. Buck, "Wind-wave-induced velocity in ati sar ocean surface currents: First experimental evidence from an airborne campaign," *Journal of Geophysical Research: Oceans*, vol. 121, no. 3, pp. 1640–1653, Mar. 2016.

[63] S. Aslebagh, G. Farquharson, J. Sahr, and R. Romeiser, "Wave-dependent directional biases in airborne ocean surface current estimation," in *IEEE Int. Geosci. Remote Sens. Symp.*, Jul. 2018.

[64] S. Aslebagh, "Improvement of geophysical model functions for Radar-based ocean surface currents measurements," Ph.D. dissertation, University of Washington, Dec. 2018.

[65] R. Romeiser and D. R. Thompson, "Numerical study on the along-track interferometric radar imaging mechanism of oceanic surface currents," *IEEE Trans. Geosci. Remote Sens.*, vol. 38, no. 1, pp. 446–458, 2000.

[66] H. Deng, G. Farquharson, J. Thomson, S. Moghimi, and T. Ozkan-Haller, "An analysis of error in surface current mapping by an along-track interferometric FMCW SAR," in *IEEE Int. Geosci. Remote Sens. Symp.*, Jul. 2016.

[67] R. K. Raney, "Synthetic aperture imaging radar and moving targets," *IEEE Trans. Aerosp. Electron. Syst.*, vol. AES-7, no. 3, pp. 499–505, 1971.

[68] M. A. Sletten, "An analysis of gradient-induced distortion in ATI-SAR imagery of surface currents," *IEEE Trans. Geosci. Remote Sens.*, vol. 44, no. 7, pp. 1995–2002, 2006.

[69] M. Bao, W. Alpers, and C. Bruning, "A new nonlinear integral transform relating ocean wave spectra to phase image spectra of an along-track interferometric synthetic aperture radar," *IEEE Trans. Geosci. Remote Sens.*, vol. 37, no. 3, pp. 461–466, Jan. 1999.

Appendix A

ANALYSIS OF THE EFFECT OF FRONT-END COMPONENT PHASE NONLINEARITY

In Chapter 3, we hypothesized that the frequency-dependent phase ripple in the front-end components results in a phase that is roughly independent of the beat frequency. In this appendix, we show that this is true. Note that the contents of this appendix are cited from the author's paper [35].

To study the effect of non-linearity in the phase response of front-end components in FMCW receivers, we derive an analytical expression for the frequency-domain response of a beat frequency signal with a nonlinear phase front-end. We use this expression to show that the effect is beat frequency (and therefore, range) independent.

Without loss of generality, we express the transmitted signal as a baseband signal:

$$s_T(t) = Ae^{i\left(\omega_0 t + \frac{1}{2}at^2\right)} \ , \ -\frac{T}{2} < t < \frac{T}{2} \tag{A.1}$$

where a denotes the chirp rate, ω_0 denotes the initial frequency and is zero for baseband signal. The frequency response of $s_T(t)$ is obtained by taking the Fourier transform

$$\begin{aligned} S_T(\omega) &= \int_{-\infty}^{+\infty} Ae^{i\left(\omega_0 t + \frac{1}{2}at^2\right)} e^{-i\omega t} dt \\ &= \int_{-T/2}^{+T/2} Ae^{i\left((\omega_0 - \omega)t + \frac{1}{2}at^2\right)} dt \\ &= \int_{-T/2}^{+T/2} Ae^{ih(t)} dt \ , \end{aligned} \tag{A.2}$$

where $h(t) = (\omega_0 - \omega)t + \frac{1}{2}at^2$. To obtain an approximate expression for $S_T(\omega)$, we applied the method of stationary phase, which is often used to find an approximation of the integral with the following format:

$$f(\lambda) = \int_a^b g(t)e^{i\lambda h(t)} dt \ , \tag{A.3}$$

where $\lambda \to \infty$, and $t, g(t), h(t)$ are real. Note that if the phase term $\lambda h(t)$ varies rapidly, contributions to the integral cancels and the integral tends to be zero.

The Taylor series of $h(t)$ at $t = t_0$ is

$$h(t) = h(t_0) + h^{'}(t_0)(t - t_0) + \frac{1}{2}h^{''}(t_0)(t - t_0)^2 + \cdots$$

If the following conditions are satisfied:

$$h^{'}(t_0) = 0, \quad h^{''}(t_0) > 0, \quad a < t_0 < b \, ,$$

then t_0 is the point of stationary phase, near which the phase term $\lambda h(t)$ varies slowly and the contributions to the integral do not cancel. Then we have

$$h(t) = h(t_0) + O\Big((t - t_0)^2\Big) \, . \tag{A.4}$$

Substituting (A.4) into (A.3), we obtain the approximation of $f(\lambda)$ as

$$\begin{aligned} f(\lambda) &\approx \int_{t_0-\varepsilon}^{t_0+\varepsilon} g(t_0) e^{i\lambda\Big(h(t_0)+\frac{1}{2}h^{''}(t_0)(t-t_0)^2\Big)} dt \\ &\approx g(t_0) e^{i\lambda h(t_0)} \int_{-\infty}^{+\infty} e^{i\Big(\frac{1}{2}\lambda h^{''}(t_0)t^2\Big)} dt \\ &= g(t_0)\sqrt{\frac{2\pi}{\lambda h^{''}(t_0)}} e^{i\Big(\lambda h(t_0)+\frac{\pi}{4}\Big)} \, . \end{aligned} \tag{A.5}$$

Note in the last step we use the result of the integral

$$\int_{-\infty}^{+\infty} e^{i\lambda t^2} dt = \sqrt{\frac{\pi}{\lambda}} e^{i\frac{\pi}{4}} \, , \quad \lambda > 0$$

Now we approximate $S_T(w)$ in (A.2) using stationary phase method described in (A.5):

$$\begin{aligned} S_T(\omega) &\approx A\sqrt{\frac{2\pi}{h^{''}(t_0)}} e^{i\Big(h(t_0)+\frac{\pi}{4}\Big)} \\ &= A\sqrt{\frac{2\pi}{a}} e^{i\Big(-\frac{w^2}{2a}+\frac{\pi}{4}\Big)} \, , \end{aligned} \tag{A.6}$$

where t_0 is the solution to $h^{'}(t) = 0$.

The received signal in the radar receiver is a delayed version of the transmitted chirp:

$$s_d(t) = s_T(t - \tau) \, . \tag{A.7}$$

We compute the corresponding frequency response by taking the Fourier transform and then using the stationary phase approximation:

$$\begin{aligned} S_d(\omega) &= \int_{-\infty}^{+\infty} s_T(t-\tau)e^{-i\omega t}dt \\ &= A\int_{\tau-T/2}^{\tau+T/2} e^{i\left(\omega_0(t-\tau)+\frac{1}{2}a(t-\tau)^2\right)}e^{-i\omega t}dt \\ &= A\int_{\tau-T/2}^{\tau+T/2} e^{i\left(\frac{1}{2}at^2-(w+a\tau)t+\frac{a}{2}\tau^2\right)}dt \\ &\approx A\sqrt{\frac{2\pi}{a}}e^{i(-\frac{\omega^2}{2a}-\tau\omega+\frac{\pi}{4})} \ . \end{aligned} \tag{A.8}$$

We model the phase response of the front-end electronics with a frequency-dependent phase $\Phi_{fr}(\omega)$. The signal at the output of the front-end components is denoted by $s_f(t)$, and can be written as

$$\begin{aligned} S_f(\omega) &= S_d(\omega)e^{-i\Phi_{fr}(w)} \\ &= A\int_{\tau-T/2}^{\tau+T/2} e^{i\left(\frac{1}{2}at^2-(w+a\tau)t+\frac{a}{2}\tau^2-\Phi_{fr}(w)\right)}dt \\ &\approx A\sqrt{\frac{2\pi}{a}}e^{i(-\frac{\omega^2}{2a}-\tau\omega+\frac{\pi}{4}-\Phi_{fr}(w))} \ , \end{aligned} \tag{A.9}$$

The signal after the mixing operation is the beat frequency signal, or dechirped signal, which is mathematically equivalent to multiplying (A.1) by the complex conjugate of $s_f(t)$:

$$s_b(t) = s_T(t)s_f^*(t) \ . \tag{A.10}$$

The frequency response of the beat frequency signal can be obtained as the convolution of $S_T(\omega)$ and $S_f^*(-\omega)$:

$$\begin{aligned} S_b(\omega) &= \int_{-\infty}^{+\infty} S_T(\Omega)S_f^*(\Omega-\omega)d\Omega \\ &\approx A^2\frac{2\pi}{a}e^{i(\frac{\omega^2}{2a}-\tau\omega)}\int_{-\infty}^{+\infty} e^{i\left(-\frac{\omega}{a}\Omega+\tau\Omega+\Phi_{fr}(\Omega-\omega)\right)}d\Omega \\ &= A^2\frac{2\pi}{a}e^{i(-\frac{\omega^2}{2a})}\int_{-\infty}^{+\infty} e^{i\left(\Phi_{fr}(\Omega-\omega)\right)}d\Omega \ , \end{aligned} \tag{A.11}$$

where $\Delta\Omega$ is the bandwidth of the transmitted chirp signal. Note here the argument in $S_b(\omega)$ is the beat frequency, which satisfies the condition $\omega = a\tau$. Thus, the $\frac{w}{a} - \tau$ term in the

integral becomes zero, making the function in the integral independent of ω. However, one must be careful about the integration interval in (A.11) since the arguments in $S_T(\Omega)$ and $S_f(\Omega-\omega)$ should satisfy

$$\begin{matrix} -\frac{\Delta\Omega}{2} < \Omega < \frac{\Delta\Omega}{2} \\ -\frac{\Delta\Omega}{2} < \Omega-\omega < \frac{\Delta\Omega}{2} \end{matrix} . \tag{A.12}$$

Therefore, (A.11) becomes

$$S_b(\omega) = \begin{cases} A^2\frac{2\pi}{a}e^{i(-\frac{\omega^2}{2a})} & \\ \times \int_{-\frac{\Delta\Omega}{2}}^{\omega+\frac{\Delta\Omega}{2}} e^{i\left(\Phi_{fr}(\Omega-\omega)\right)}d\Omega\,, & -\frac{\Delta\Omega}{2} < \omega < 0 \\ A^2\frac{2\pi}{a}e^{i(-\frac{\omega^2}{2a})} & \\ \times \int_{\omega-\frac{\Delta\Omega}{2}}^{\frac{\Delta\Omega}{2}} e^{i\left(\Phi_{fr}(\Omega-\omega)\right)}d\Omega\,, & 0 < \omega < \frac{\Delta\Omega}{2} \\ 0\,, & \text{otherwise} \end{cases} \tag{A.13}$$

The phase response in terms of the beat frequency ω is obtained by taking the phase of (A.13), which contains a quadratic phase term and the phase of the integral. The quadratic phase term is the residual video phase term present in FMCW radar, and does not result in the range-dependent phase ripple we observed in the phase calibration experiment.

The dependence of the phase of the integral in (A.13) on the beat frequency, or time delay τ of the received signal for our system is evaluated numerically in Mathematica, and is shown in Fig. A.1. It turns out the phase of the integral is roughly independent of τ for our system with chirp length of 170 µs and bandwidth of 80 MHz. We also numerically studied this effect for systems with different bandwidths and chirp lengths and found that with chirp length greater than 120 µs, the phase of the integral in Equation A.13 is roughly independent of τ. However, the phase gradually decreases with τ for chirp length less than 120 µs. The cause for this observation is out of the scope of this study and can be another topic related to FMCW radars. Therefore, we have demonstrated our hypothesis that the frequency-dependent phase ripple $\Phi_{fr}(\omega)$ in the front-end components of the receivers is independent

of beat frequency for systems with comparably long chirp length greater than 120 µs, i.e., for such systems, the nonlinearities in the front-end electronics affect all returns roughly the same, and therefore does not introduce the range-dependent phase ripple observed in the phase calibration experiment.

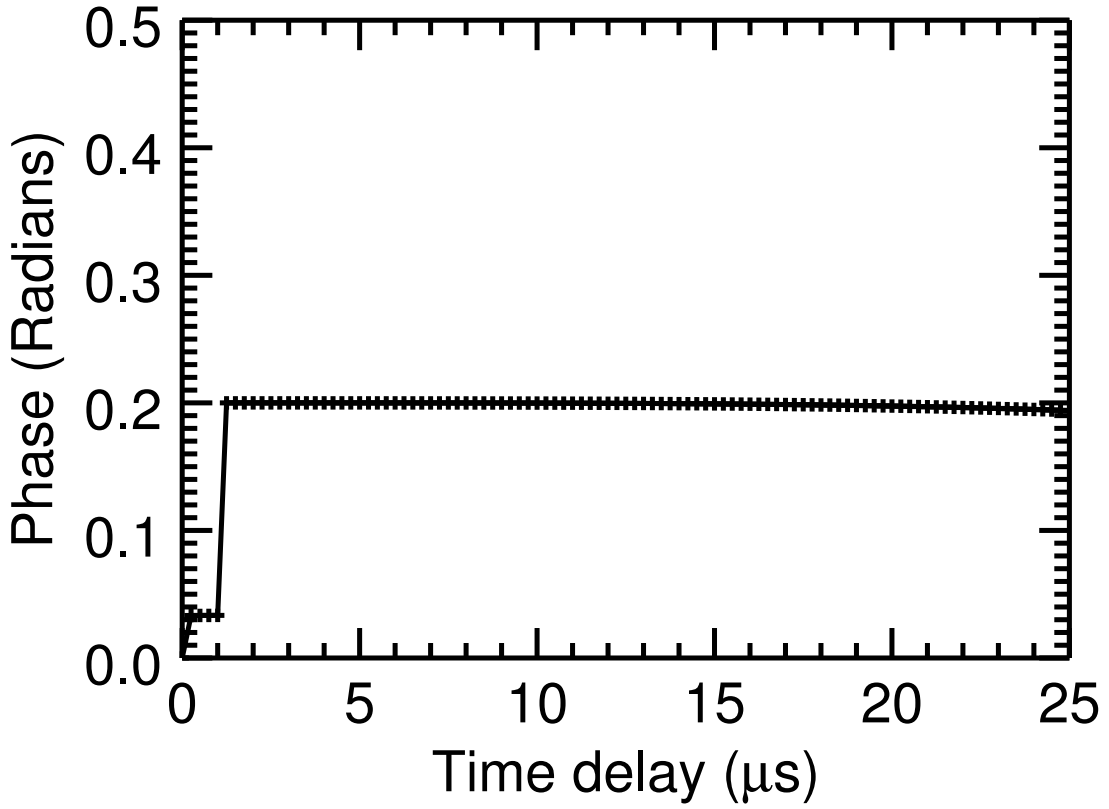

Figure A.1: Numerically-computed values of the argument (phase) of the integral in Equation A.13.

Appendix B

GENERATION OF CORRELATED GAUSSIAN ERROR

As mentioned in Chapter 5, we added error to the INS data and used the error disturbed INS data to represent the actual measurement made by INS with certain level of uncertainty. Note that the error we created here is not white Gaussian noise due to the fact that during a short time period of the flight, e.g., a few tenth second, the change of aircraft attitudes and velocities at each time instant might be highly correlated with each other because the air disturbance is not likely to change during this short period. Therefore, we simulated correlated Gaussian errors to add to the INS attitude and velocity measurements. In this appendix, we details our simulations on creating the correlated Gaussian noise.

The problem is to generate a multivariate normal (MN) random process $X = (X_1, \ldots, X_n)$ where $X \sim MN(0, \Sigma)$. Assume we have independent and identically distributed (IID) standard normal random variables $Z_i \sim N(0, 1)$ for $i = 1, \ldots, n$. Let C be a $(n \times m)$ matrix and let $Z = (Z_1, Z_2, \ldots, Z_n)^T$. Then

$$C^T Z \sim MN(0, C^T C). \tag{B.1}$$

Hence, the problem turns out to be finding C such that $C^T C = \Sigma$. Obtaining such a matrix C is equivalent to computing the Cholesky decomposition of covariance matrix Σ.

From linear algebra, any symmetric positive-definite matrix, M, can be decomposed by

$$M = U^T D U \tag{B.2}$$

where U is an upper triangular matrix and D is a diagonal matrix with positive diagonal

elements. Since the covariance matrix, Σ, is symmetric positive-definite, we can write

$$\begin{aligned}\Sigma &= U^T D U \\ &= \left(U^T\sqrt{D}\right)\left(\sqrt{D}U\right) \\ &= \left(\sqrt{D}U\right)^T\left(\sqrt{D}U\right)\end{aligned} \tag{B.3}$$

Therefore, the matrix C satisfies the relationship $C^T C = \Sigma$. This matrix is the well-known Cholesky Decomposition of Σ.

Now back to our problem, to obtain the desired correlated Gaussian error we need $X = C^T Z$ where Z is one realization from the standard normal random process $Z \sim N(0, I)$. Since the INS measurement used in our study for attitude/velocity is a time series with n (8679) samples, the desired Gaussian error X should have a dimension of $(n \times 1)$, indicating that the dimension for Z would be $(n \times 1)$ and the dimension for covariance matrix Σ in Equation (B.3) is $n \times n$. Hence, the first step is to create the covariance matrix Σ. Then we compute the Cholesky decomposition of Σ and finally multiply the decomposition with Z, which is one random realization from standard normal process to obtain one realization of the correlated Gaussian error. To create the covariance matrix Σ, we defined the value of element in the i_{th} row and the j_{th} column in the matrix with

$$v_{ij} = (10\sigma_{ins})^2 e^{-\frac{(i-j)^2}{2}} \tag{B.4}$$

Here is an example to obtain the correlated error for the pitch angle measurement. We set σ_{ins} in Equation (B.4) to be the INS pitch accuracy shown in Table 5.2. Note from the equation that the value for variance is actually 10 times the σ_{ins}, which is needed to reproduce the 0.1 radians phase error we observed in the along-track direction. Then we used Python numpy.inalg.cholesky() function to perform the Cholesky decomposition of Σ. Also, we generated one realization of 8679 data samples from the standard normal distribution in Python by using the numpy.random.randn() function. Finally, we multiply the Cholesky decomposition with generated errors from standard normal distribution to get the correlated Gaussian error for the pitch angle measurement. We followed the same procedure to generate

the correlated Gaussian errors for roll, yaw and velocities measurements, respectively. Note that for each simulation of the error, we need to pick a different random seed before calling numpy.random.randn(). This will guarantee that the generated roll, pitch and yaw errors are independent of each other, as assumed in the numerical analysis in Chapter 5.

Appendix C

TEMPERATURE DEPENDENCE ON THE PHASE OFFSET BETWEEN RECEIVE CHANNELS

In Chapter 4, we showed the estimated antenna phase imbalance from data sets collected at different times in Figure 4.8. It turns out that although the pattern of the estimated phase imbalance stays the same, one can observe the shift of the mean phase offset which can be as much as 0.2 radians. These observed mean phase offset can be introduced by different sources. For example, the change of the radar operating temperature introduces different level of thermal noise to the electronic components of the system, which varies the signal to noise ratio of the collected data and can cause the estimated phase to be inconsistent. Meanwhile, the difference between the electrical path length of each receiver channel might also be different, which can introduce different mean phase offset between receivers. In this appendix, we studied the temperature dependence of the phase offset between the radar receivers.

During the experiment, we placed the radar system without the antennas in an environmental chamber, which forms a lab-controlled environment for us to adjust the operating temperature. Then we let the radar running under the adjusted temperature for half an hour to warm up, and injected signals from the signal generator to both radar receivers and collected the raw data. Finally, we processed the raw data in the SAR processor and estimated the phase offset between radar receivers. The estimated phase offsets between receivers under different operating temperatures are summarized in Table C.1.

From the estimated results in Table C.1, we find that although the mean phase offset does vary with different environment temperatures, the maximum difference in the mean phase offset is only about 0.036 radians (corresponding to 1.8 cm/s in radial velocity error), which

Table C.1: Temperature dependence of mean phase offset between SAR receivers.

Temperature (°C)	Mean Phase Offset (Radians)
10	0.14347 ± 0.00002
19	0.12095 ± 0.00002
24	0.13408 ± 0.00002
30	0.15645 ± 0.00002

is not significant compared with the observed shift in the mean phase offset (0.2 radians). Therefore, it looks to us that the change of temperature does not account for most of the observed variations in the mean phase offset between receivers and the mean phase offset is roughly temperature independent.

VITA

Huazeng Deng received the B.S. degree from Beijing Jiaotong University, Beijing, China, in 2009 and M.S. degree in electrical and computer engineering from the University of Missouri, Columbia, USA, in 2012. He completed his PhD research at the department of electrical engineering at the University of Washington, Seattle, USA in 2018. His research interests include ocean surface currents estimation with along-track SAR interferometry, signal and image processing for the extraction of information from remote sensing data, and ground-based radar interferometry for surface deformation mapping.